AFRL-AFOSR-VA-TR-2021-0098

Electrically Detected Electron Nuclear Double Resonance in Solid State Electronics

Lenahan, Patrick
PENNSYLVANIA STATE UNIVERSITY
201 OLD MAIN
UNIVERSITY PARK, PA,
US

08/16/2021
Final Technical Report

DISTRIBUTION A: Distribution approved for public release.

Air Force Research Laboratory
Air Force Office of Scientific Research
Arlington, Virginia 22203
Air Force Materiel Command

REPORT DOCUMENTATION PAGE							*Form Approved* *OMB No. 0704-0188*

1. REPORT DATE *(DD-MM-YYYY)*	**2. REPORT TYPE**	**3. DATES COVERED** *(From - To)*
16-08-2021	Final	01 Jun 2017 - 31 May 2021

4. TITLE AND SUBTITLE
Electrically Detected Electron Nuclear Double Resonance in Solid State Electronics

5a. CONTRACT NUMBER

5b. GRANT NUMBER
FA9550-17-1-0242

5c. PROGRAM ELEMENT NUMBER
61102F

6. AUTHOR(S)
Patrick Lenahan

5d. PROJECT NUMBER

5e. TASK NUMBER

5f. WORK UNIT NUMBER

7. PERFORMING ORGANIZATION NAME(S) AND ADDRESS(ES)
PENNSYLVANIA STATE UNIVERSITY
201 OLD MAIN
UNIVERSITY PARK, PA
US

8. PERFORMING ORGANIZATION REPORT NUMBER

9. SPONSORING/MONITORING AGENCY NAME(S) AND ADDRESS(ES)
AF Office of Scientific Research
875 N. Randolph St. Room 3112
Arlington, VA 22203

10. SPONSOR/MONITOR'S ACRONYM(S)
AFRL/AFOSR RTA1

11. SPONSOR/MONITOR'S REPORT NUMBER(S)
AFRL-AFOSR-VA-TR-2021-0098

12. DISTRIBUTION/AVAILABILITY STATEMENT
A Distribution Unlimited: PB Public Release

13. SUPPLEMENTARY NOTES

14. ABSTRACT
During the past four years we have worked to develop electrically detected electron nuclear double resonance (EDENDOR). The conventional resonance technique known as electron nuclear double resonance (ENDOR) has been an exceptionally powerful tool in the study of the immediate surroundings of defects in semiconductors and insulators for quite some time. Unfortunately, conventional ENDOR has never been very useful in the study of semiconductor device problems because it has a sensitivity typically two to three orders of magnitude less than that of the sensitivity of the conventional electron paramagnetic resonance (EPR) technique upon which it is based. Since conventional EPR sensitivity is about 10^10 total electron spins within the sample under study, conventional ENDOR sensitivity is, at best, about 10^12 total defects. This number is far too large for studies of defects within meaningful micro or nano technology devices. The technique of electrically detected magnetic resonance (EDMR) offers a possible solution to the sensitivity limits of ENDOR. EDMR sensitivity is about seven orders of magnitude more sensitive than that of conventional EPR, around 10^3 total defects (with considerable effort). By combining the sensitivity of EDMR with ENDOR we hoped to develop a new technique with all of the analytical power of ENDOR and a sensitivity so greatly enhanced that it would allow meaningful measurements in micro and nanotechnology scale devices. In this effort we have been largely successful, demonstrating EDENDOR, for the first time, in a fully processed semiconductor device, a pn junction diode. We have also demonstrated EDENDOR in thin films of amorphous hydrogenated silicon and thin films
of amorphous boron. (It should be pointed out that our work does not constitute the first observation of electrically
detected ENDOR. Two other studies were published previously, neither involving a fully processed device and both
involved relatively weak ENDOR responses.)

15. SUBJECT TERMS

16. SECURITY CLASSIFICATION OF:			**17. LIMITATION OF ABSTRACT**	**18. NUMBER OF PAGES**	**19a. NAME OF RESPONSIBLE PERSON**
a. REPORT	**b. ABSTRACT**	**c. THIS PAGE**			KENNETH GORETTA
U	U	U	UU	52	**19b. TELEPHONE NUMBER** *(Include area code)* 426-7349

Standard Form 298 (Rev.8/98)
Prescribed by ANSI Std. Z39.18

Final Report for AFOSR Contract FA 9550-17-1-0242

Patrick M. Lenahan

Pennsylvania State University

University Park, PA 16802

During the past four years we have worked to develop electrically detected electron nuclear double resonance (EDENDOR). The conventional resonance technique known as electron nuclear double resonance (ENDOR) has been an exceptionally powerful tool in the study of the immediate surroundings of defects in semiconductors and insulators for quite some time.[1] Unfortunately, conventional ENDOR has never been very useful in the study of semiconductor device problems because it has a sensitivity typically two to three orders of magnitude less than that of the sensitivity of the conventional electron paramagnetic resonance (EPR) technique upon which it is based.[2] Since conventional EPR sensitivity is about 10^{10} total electron spins within the sample under study, conventional ENDOR sensitivity is, at best, about 10^{12} total defects. This number is far too large for studies of defects within meaningful micro or nano technology devices.

The technique of electrically detected magnetic resonance (EDMR) offers a possible solution to the sensitivity limits of ENDOR. EDMR sensitivity is about seven orders of magnitude more sensitive than that of conventional EPR, around 10^3 total defects (with considerable effort). [3,4] By combining the sensitivity of EDMR with ENDOR we hoped to develop a new technique with all of the analytical power of ENDOR and a sensitivity so greatly enhanced that it would allow meaningful measurements in micro and nanotechnology scale devices. In this effort we have been largely successful, demonstrating EDENDOR, for the first time, in a fully processed semiconductor device, a pn junction diode. We have also demonstrated EDENDOR in thin films of amorphous hydrogenated silicon and thin films of amorphous boron. (It should be pointed out that our work does not constitute the first observation of electrically detected ENDOR. Two other studies were published previously, neither involving a fully processed device and both involved relatively weak ENDOR responses. [5,6])

In the pn junction study we utilized EDMR detection through spin dependent recombination (SDR) EDMR. In the amorphous boron and amorphous silicon study we utilized spin dependent trap assisted tunneling (SDTAT) EDMR. In the SiC pn junction we observed matrix EDENDOR, an ENDOR response which detected the nuclear resonance of distant atomic sites without providing hyperfine results, that is without providing information about the interaction between the observed nuclei and the unpaired electron at the paramagnetic site. In the amorphous boron and amorphous hydrogenated silicon measurements, we were able to extract some hyperfine results.

One might ask: why report on these three materials systems? We had hoped to investigate more systems and hope we may at some point do this. However, we believe our measurements on these three very different systems provide very direct completely unambiguous demonstrations that we are indeed observing EDENDOR. The ENDOR frequencies observed were, within experimental error, exactly what would be anticipated of the relevant nuclei. In the case of the heavily nitrogen doped diodes, we observed the EDENDOR response at exactly that of nitrogen NMR at the magnetic fields utilized. For amorphous hydrogenated silicon, we observed the EDENDOR response at exactly that of hydrogen NMR at the magnetic fields utilized. In the amorphous boron films, we observed the EDENDOR response at exactly that of the NMR frequencies of the two boron isotopes. (By "exactly," I mean within one or two per cent of the very precisely known values.)

Furthermore, the three systems involved significantly different detection methods. In the SiC pn junction diodes, we utilized spin dependent recombination for the EDENDOR detection. In the amorphous boron and amorphous hydrogenated silicon devices we utilized spin dependent trap assisted tunneling detection. In the SiC pn junction and the amorphous silicon film, the measurements were made at room temperature. In the case of the amorphous boron samples, the measurements were made at slightly lower temperatures, about 250K.

The work in this project involved the construction of an EDENDOR spectrometer and, in so doing, solving moderately challenging technology problems which initially limited our progress. The EDENDOR spectrometer design is discussed in a paper which we published in the Review of Scientific Instruments. The observations of EDENDOR in the SiC pn junction diode and in amorphous hydrogenated silicon are discussed in two papers in Applied Physics Letters. A paper dealing with the amorphous boron EDENDOR has also recently been submitted to Applied Physics Letters.

Several other papers have resulted from this AFOSR sponsored study which do not directly focus on EDENDOR, but which grew out of some aspect of the work. Most significantly among this work is a paper in the Journal of Applied Physics, first authored by (now former) graduate student Mark Anders and co-authored by AFRL physicists Arthur Edwards and Renee van Ginhoven and Sandia physicist Peter Schultz. The work deals with an indirect measure of nearby nitrogen hyperfine interactions with silicon vacancies very near the SiC-oxide interface of 4H SiC MOSFETs. The work compares experiment and theory: fairly crude hyperfine measurements and electronic interface density of states determined from EDMR with theoretical calculations of the same things.

We also published two papers dealing with ultra-low field and frequency EDMR in SiC devices. These papers were first authored by James Ashton who has recently joined NIST, Gaithersburg. This work was supported in part by the AFOSR contract but also by the US Army Research Laboratory At the extremely low magnetic fields used in these studies, a few tenths of a milli Tesla to a few milli Tesla, EDENDOR would involve audio frequency NMR. Audio frequencies have, to the best of our knowledge, never been utilized in ENDOR of any kind. The very low frequencies would eliminate some of the electronic problems in the EDEDMR measurements and would also allow us to apply extremely large amplitude oscillating magnetic fields for both the electron paramagnetic resonance and nuclear magnetic resonance involved the EDENDOR measurement. Unfortunately, in part due to the COVID restrictions placed on my laboratory, we were not able to extend these studies to EDENDOR. However, we were able to observe some ultra-low field resonance effects which have rarely been observed in any spin system.

Several students who were supported in significant part by this contract have completed their Ph.D. studies:

Brian Manning (now at Keysight Technology R and D Center, Santa Rosa, California)

Mark Anders (now at NIST, Gaithersburg)

Duane McCrory (now at Keysight, Santa Rosa)

James Ashton (now at NIST Gaithersburg).

References

1.) L. Kevan and L.D. Kispert, Electron Spin Double Resonance Spectroscopy (John Wiley and Sons, New York.1976)
2.) C.P. Poole, Electron Spin Resonance, A Comprehensive Treatise on Experimental Techniques, Second Edition (John Wiley and Sons, New York, 1983)
3.) D. Kaplan, I. Solomon, and N.F. Mott, J. Phys. Lett., vol.39, 51 (1978)
4.) P.M. Lenahan, C.J. Cochrane, J.P. Campbell, and J. T. Ryan, ECS Trans. Vol.35605 (2011)
5.) F. Hoehne, L. Dreher, H. Huebel, M. Stutzmann, and M.S. Brandt, Phys. Rev. Lett. Vol.106,187706
6.) B. Stich, S. Greulich-Weber, and J.M. Spaeth, Appl. Phys. Lett. vol.68,1102 (1996)

The publications resulting from this work constitute the rest of this report.

Journal of Applied Physics ARTICLE scitation.org/journal/jap

Electrically detected electron nuclear double resonance in 4H-SiC bipolar junction transistors

Cite as: J. Appl. Phys. **126**, 125709 (2019); doi: 10.1063/1.5108961
Submitted: 4 May 2019 · Accepted: 12 September 2019 ·
Published Online: 30 September 2019

View Online Export Citation CrossMark

Ryan J. Waskiewicz,[a] Brian R. Manning, Duane J. McCrory, and Patrick M. Lenahan

AFFILIATIONS

Department of Engineering Science and Mechanics, The Pennsylvania State University, University Park, Pennsylvania 16802, USA

[a]**Author to whom correspondence should be addressed:** rjw5352@psu.edu

ABSTRACT

We demonstrate high signal-to-noise electrically detected electron-nuclear double resonance measurements on fully processed bipolar junction transistors at room temperature. This work indicates that the unparalleled analytical power of electron-nuclear double resonance in the identification of paramagnetic point defects can be exploited in the study of defects within fully functional solid-state electronic devices.

INTRODUCTION

The performance of nearly all present-day solid-state electronic devices is strongly influenced by the presence of various point defects, both intrinsic and extrinsic. The family of electron paramagnetic resonance (EPR) techniques has unparalleled analytical power to identify the structural and chemical nature of point defects in semiconductors and insulators.[1,2] Among all EPR techniques, arguably, electron-nuclear double resonance (ENDOR) is the most powerful one to characterize the nuclei responsible for hyperfine splitting.[3] ENDOR combines EPR and nuclear magnetic resonance (NMR). In ENDOR, one observes a change in the EPR response due to NMR at nearby magnetic nuclei. ENDOR can often provide extremely detailed information about the point defect structure and chemistry. Unfortunately, conventional EPR measurements are almost never capable of measurements in practical solid-state electronic devices. Conventional EPR has a sensitivity on the order of 10×10^9 total paramagnetic sites.[4] ENDOR sensitivity is typically several orders of magnitude less than that of EPR. These numbers are far higher than the number of defect centers in most modern micro- and nanoscale devices.

Electrically detected magnetic resonance (EDMR) measurements involve the observation of EPR through changes in current or voltage in a solid-state device.[5] EDMR detected EPR offers a sensitivity of at least 10^7 times better than that of conventional EPR and is exclusively sensitive to defects that directly affect the device performance.[6] EDMR thus allows EPR measurements to be made in state-of-the-art semiconductor devices and to directly identify defect centers involved in the device performance.[7] In this work, we show that EDMR detection can be utilized to observe ENDOR in a fully processed device, a bipolar junction transistor (BJT) at room temperature, with a relatively high signal-to-noise ratio. This work indicates that electrically detected electron-nuclear double resonance (EDENDOR) has the potential to provide enormous analytical power in the study of performance limiting (and performance enhancing) defects in electronic devices of technological interest.

ELECTRON PARAMAGNETIC RESONANCE (EPR)

A basic understanding of the conventional EPR measurement is required to understand both EDMR and EDENDOR. In continuous wave EPR measurements, the response of paramagnetic centers to a large slowly varying magnetic field in combination with an oscillating magnetic field is observed. For paramagnetic defects with spin $S = 1/2$, this slowly varying magnetic field provides an energy difference between the two values of the electron spin quantum number: $m_s = +\frac{1}{2}$ and $m_s = -\frac{1}{2}$. When the frequency of the oscillating magnetic field, ν, times Planck's constant, h, is equal to this energy difference, electron spins can be "flipped." In the case of the free electron, that is, the case in which the unpaired electron is otherwise unaffected by its surroundings, the resonance condition is expressed as[2]

$$h\nu = g_e \mu_B B. \quad (1)$$

Here, g_e is the Landé g value ($g_e = 2.00232\ldots$), μ_B is the Bohr magneton, and B is the magnitude of the applied magnetic field. In nearly all conventional EPR measurements, the sample is placed into a microwave resonator with a high quality factor (Q) providing the oscillating magnetic field of frequency ν and subjected to a perpendicular magnetic field, which slowly varies at approximately 1 G/s. EPR measurements are most commonly performed using X-band frequencies ($\nu \approx 9.75$ GHz) in combination with large magnetic fields in the range of $B \approx 3500$ G. The analytical power of EPR comes from deviations from the free electron resonance case of (1). When the electron is placed in a paramagnetic defect in real material systems, the EPR response is altered by the local environment. There are two primary factors that make the resonance condition system dependent: spin orbit coupling and electron-nuclear hyperfine interactions (other factors play important roles under some circumstances). Spin orbit coupling changes the Landé g_e to an orientation dependent value generally expressed as a second rank tensor. Electron-nuclear hyperfine interactions are interactions between the paramagnetic defect site and nearby nuclei with magnetic moments. These hyperfine interactions result in a splitting of the energy levels of the system. Considering both spin orbit coupling and electron-nuclear hyperfine interactions with a single nearby magnetic nucleus, the resonance condition becomes[2,8]

$$h\nu = g\mu_B B \pm mA. \tag{2}$$

The free electron g_e is replaced by an orientation dependent g, which is usually expressed as a second rank tensor, m is the nuclear spin quantum number of the nearby magnetic nucleus, and A is the electron-nuclear hyperfine coupling due to that nucleus also is usually expressed as a second rank tensor. Expressing the hyperfine coupling as a second rank tensor accounts for anisotropy in the parameter. Accurately measuring the frequency ν of the microwave resonance field and the magnetic field at resonance allows for the identification of the chemical and physical nature of atomic scale defects as the resonance condition is highly dependent upon the defect and local surroundings of the defect. In general, adding more nearby magnetic nuclei complicates the EPR response. This can result in unresolved or poorly resolved hyperfine interactions, which can make the detailed analysis of conventional EPR measurements extremely hard, if not impossible.

ELECTRICALLY DETECTED MAGNETIC RESONANCE (EDMR)

As mentioned previously, conventional EPR sensitivity is about 10^{10} total paramagnetic defects in a sample, greatly limiting its application to the study of defects in state-of-the-art micro- and nanoscale devices. EDMR is a variation of EPR in which a change in the device current is measured at resonance rather than a change in microwave absorption. EDMR may be detected using (primarily) two different techniques: spin dependent recombination (SDR)[9–11] and spin dependent trap assisted tunneling (SDTAT).[12–16] In this study, we detect EDMR via SDR in the base-emitter junction of a 4H-SiC bipolar junction transistor (BJT).[17] A qualitative understanding of SDR/EDMR can be provided by the Shockley-Read-Hall model for recombination. An electron in the conduction band is trapped by a deep level defect. A hole in the valence band is then trapped by the same defect, resulting in electron and hole recombination. (The sequence of the electron and hole capture can, of course, be reversed.) This process can be spin dependent. For example, if the conduction band electron and a paramagnetic defect electron have the same spin quantum number, the capture event will be forbidden by the Pauli Exclusion Principle. When the resonance condition for the defect is met, the spin of the defect electron flips and the forbidden transition becomes allowed. SDR is most effective for defect centers near the middle of the energy gap.

ELECTRON-NUCLEAR DOUBLE RESONANCE (ENDOR)

The most powerful technique for deconvoluting electron-nuclear hyperfine interactions and identifying the structural environment of paramagnetic defects in semiconductors and insulators is ENDOR.[3,18–22] In a conventional ENDOR measurement, the EPR response is first measured. The magnetic field is then fixed at the field that results in (typically) the maximum microwave absorption, and a radio frequency (RF) is swept. When the RF induces nuclear resonance at a site near the defect observed in EPR, a change in the EPR amplitude is observed. Every atomic isotope with a nuclear moment has a unique relationship between the NMR RF and the magnetic field. Measuring the response of the EPR amplitude as a function of applied NMR RF thus directly allows for the identification of the nuclear species. It can also provide quite detailed information about the physical location of magnetic nuclei near the paramagnetic defect under observation. This is easiest to visualize for the simple case of a defect electron spin $(S) = 1/2$ and a nearby nuclear spin $(I) = 1/2$ for a single value of isotropic hyperfine interaction, a. In this case, the ENDOR response condition will be given by $\nu \cong \left|\nu_n \pm \frac{a}{2}\right|$. Thus, there are two responses to be considered: when half the hyperfine coupling constant is greater than the nuclear frequency $\left(\left|\frac{a}{2}\right| > \nu_n\right)$ and when half the hyperfine coupling constant is less than the nuclear frequency $\left(\left|\frac{a}{2}\right| < \nu_n\right)$. For the first case, the expected ENDOR response would be two lines centered about $\left|\frac{a}{2}\right|$ and split by $2\nu_n$. For the second case, the expected ENDOR response would be two lines centered about ν_n and split by $|a|$. Somewhat more complex responses can occur for $I > 1/2$ due to the presence of nuclear quadrupole moments. The presence of a nuclear quadrupole moment changes the ENDOR response frequency conditions to $\nu \cong \left|\frac{a}{2} \pm \nu_n \pm Q\right|$, where Q depends upon the electric field gradient at the nucleus and the nuclear quadrupole moment.

TABLE I. Select nuclear frequencies for a magnetic field of 3366 G.

Nucleus	Spin I	Natural abundance (%)	ν_n (MHz)
^{1}H	1/2	99.9885	14.3337
^{13}C	1/2	1.07	3.605
^{14}N	1	99.636	1.0361
^{17}O	5/2	0.038	1.9439
^{27}Al	5/2	100	3.7379
^{29}Si	1/2	4.685	2.8499
^{31}P	1/2	100	5.8077

If relatively distant nuclei are involved with a relatively small hyperfine interactions and quadrupole contributions, multiple closely spaced ENDOR lines will yield a single response centered upon the NMR frequency corresponding to the magnetic field utilized in the measurement. Our EDENDOR measurements correspond to this set of circumstances. A list of nuclear frequencies of relevant atomic nuclei is provided in Table I.[23]

ELECTRICALLY DETECTED ELECTRON-NUCLEAR DOUBLE RESONANCE (EDENDOR)

EDENDOR has not previously been demonstrated in a fully functional device of any kind. (The limited number of EDENDOR studies that have been performed involved spin dependent photoconductivity measurements on shallow P donors in Si and P_b centers at the Si/SiO_2 interface. Both studies involved metal/insulator/semiconductor structures.)[24,25] The EDENDOR spectrometer is schematically shown in Fig. 1. There are several additions to a standard EDMR spectrometer. The sample is placed into the microwave cavity and aligned with a single loop antenna. The NMR RF sweep is supplied to this loop via a Fluke arbitrary waveform generator (AWG), which is 100% amplitude modulated at a frequency of 250 Hz. This essentially turns the signal on and off at 250 Hz in order to obtain the highest possible signal-to-noise ratio. To perform the EDENDOR measurement, the EDMR response is first measured. Next, the magnetic field is held constant at various positions along the EDMR response and the NMR RF sweep is performed from 10 kHz to 15 MHz while the device current is measured.

EXPERIMENTAL DETAILS

All measurements are performed on 4H-SiC BJTs mounted onto a simple printed circuit board (PCB). The device fabrication and characterization have been described elsewhere.[26] Electrical contact is made to the device using standard wire bonds. The device base-emitter junction is forward biased below the built-in voltage and current is measured out of the base contact with the collector grounded. The BJTs are heavily doped with nitrogen as the n-type dopant and aluminum for the p-type dopant.[26] The device is placed inside the homemade spectrometer as depicted in Fig. 1. The spectrometer consists of a 4 in. Resonance Instruments electromagnet, a HP 6268B DC power supply, and a LakeShore Cryotronics 475 DSP temperature-compensated Gaussmeter and Hall probe for the magnetic field control. Microwaves of frequency $\nu = 9.358$ GHz are generated by a Micro-Now model 8330A microwave bridge and guided using standard microwave plumbing to a TE_{102} microwave cavity. A Fluke 291AWG supplied the NMR RF sweep in combination with a LeCroy WaveRunner 6100A 1 GHz oscilloscope for power flattening and Rigol DG4162 for frequency counting. For EDENDOR, a SR 830 DSP lock-in provides lock-in detection to the amplitude modulation scheme. For EDMR, the computer provides lock-in detection. All data acquisition is performed in custom-made software.

RESULTS

The EDMR response obtained on the BJT using the previously described biasing conditions is shown in Fig. 2. The linewidth of the central part of the spectrum is 3.4 G and zero-crossing

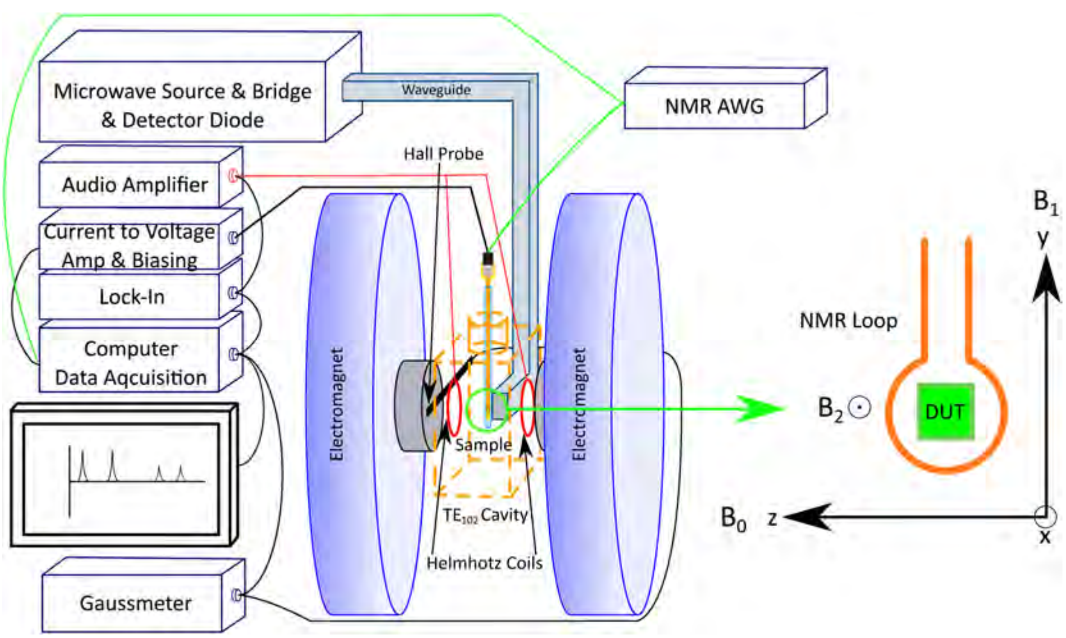

FIG. 1. A schematic of the EDENDOR spectrometer. For EDMR, the NMR RF loop and NMR AWG are bypassed, and the device current is monitored as the magnetic field is swept. For EDENDOR, the magnetic field is held constant, while the NMR AWG supplies a RF sweep and the device current is monitored.

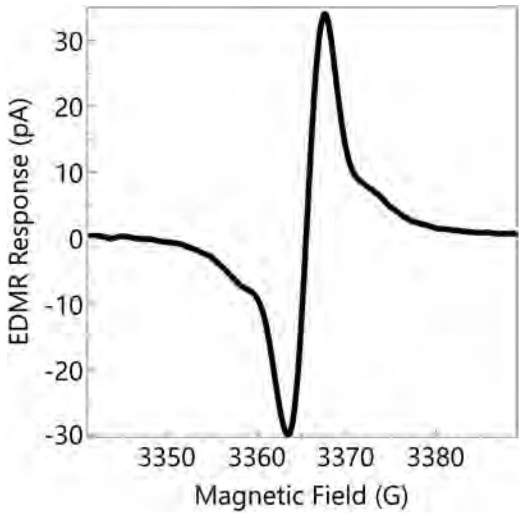

FIG. 2. Measured EDMR response as a function of the applied magnetic field. The central feature has zero-crossing $g = 2.003$ and a linewidth of 3.4 G. A very similar EDMR spectrum has been linked to a V_{Si} defect in 4H-SiC MOSFETs.

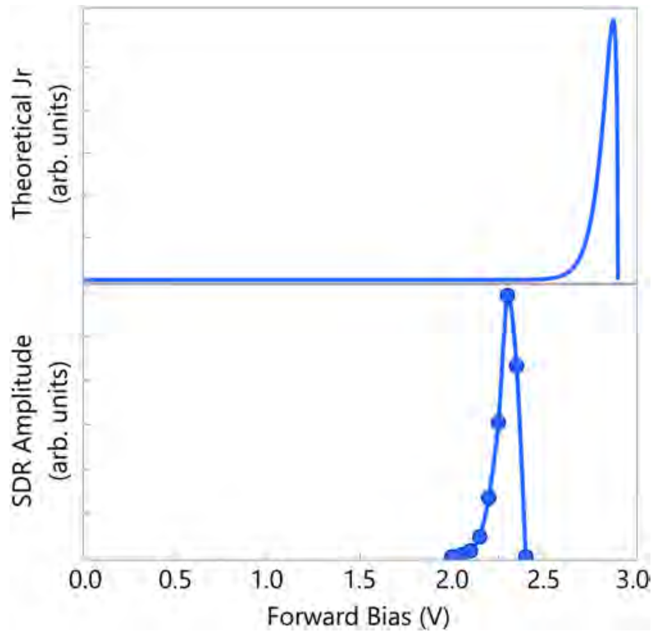

FIG. 3. Calculated recombination current J_r (top) vs SDR (bottom) as a function of junction bias. Note that the SDR response closely corresponds to the calculated response except for a shift of several tenths of a volt. This shift is primarily due to a modest bias provided by the microwave field.

$g = 2.003 \pm 0.0003$. This main EDMR response is isotropic. It should be mentioned that a very similar EDMR spectrum has been linked to a silicon vacancy (V_{Si}) in 4H-SiC MOSFETs.[17] Assuming that recombination centers are evenly distributed within the space charge region, the recombination current of the junction to a reasonable approximation is[17,27]

$$J_r = \left(\frac{q n_i W}{2}\right)(v_{th} N_t \sigma)\exp(qV_a/2kT). \tag{3}$$

Here, v_{th} is the thermal velocity, N_t is the density of recombination defects, σ is the defect capture cross section, n_i is the intrinsic carrier concentration, V_a is the forward bias, and W is the width of the depletion region. The width of the depletion region is[17,27]

$$W = \sqrt{\frac{2\varepsilon(N_a + N_d)(V_{bi} - V_a)}{qN_aN_d}}. \tag{4}$$

Here, ε is the permittivity, N_a is the density of ionized acceptor atoms, N_d is the density of ionized donor atoms, and V_{bi} is the built-in voltage of the pn junction. Figure 3 provides a comparison between the theoretical recombination current and the measured EDMR via SDR response as a function of applied forward bias. There is a semiquantitative correlation between the experiment and the simple theory. (The primary cause for the difference between the calculated and observed peak response is external device biasing due to the microwaves.) The EDMR response observed in these 4H-SiC BJTs is due to recombination at defects in the space charge region.

The EDENDOR response obtained with the magnetic field held constant near the maximum of the EDMR response

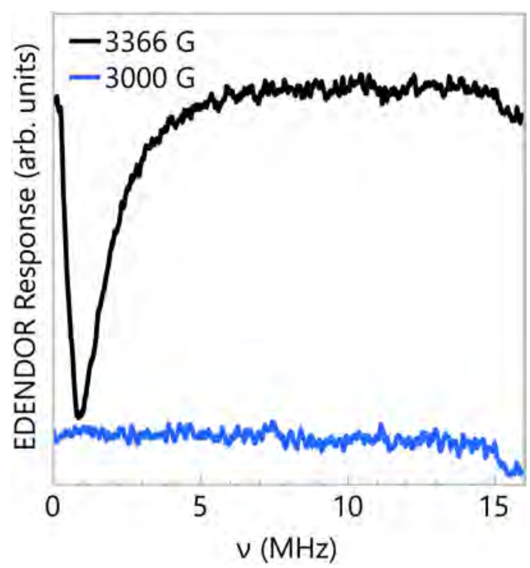

FIG. 4. The EDENDOR response (black) measured for a constant magnetic field of 3366 G. The large response peaks at 1.04 MHz. The nuclear frequency for nitrogen at this field is 1.036 MHz. The EDENDOR response for a constant magnetic field of 3000 G is shown in blue for comparison.

("on resonance" = 3366 G) is compared to the EDENDOR response with the magnetic field held constant when there is no EDMR response ("off resonance" = 3000 G) in Fig. 4. A large EDENDOR response is observed at an NMR RF of $\nu = 1.04$ MHz. Referring back to Table I, the only magnetic nucleus that could generate this response is ^{14}N, with a 99.636% naturally abundant spin 1 magnetic nucleus and corresponding ENDOR frequency of $\nu_n = 1.036$ MHz at this magnetic field. The results demonstrate that nitrogen nuclei in the vicinity of the V_{Si} defect centers are being detected with EDENDOR.

A comment should be made about the asymmetry of the EDENDOR response shown in Fig. 4. Features associated with distant ENDOR can be asymmetric, in which one side rises quickly and the other decays slowly. Such behavior has been as linked to long nuclear spin relaxation times.[19,28]

Further confirmation that the observed response is indeed EDENDOR is shown in Fig. 5. The top portion of the figure contains the EDMR response as shown in Fig. 2 previously. The middle portion of the figure contains the integrated intensity of this EDMR response. The bottom portion of the figure shows the amplitude of the 1.04 MHz EDENDOR response as a function of the constant magnetic field. The amplitude of the response tracks quite well with the EDMR response, as would be expected of a conventional ENDOR response.

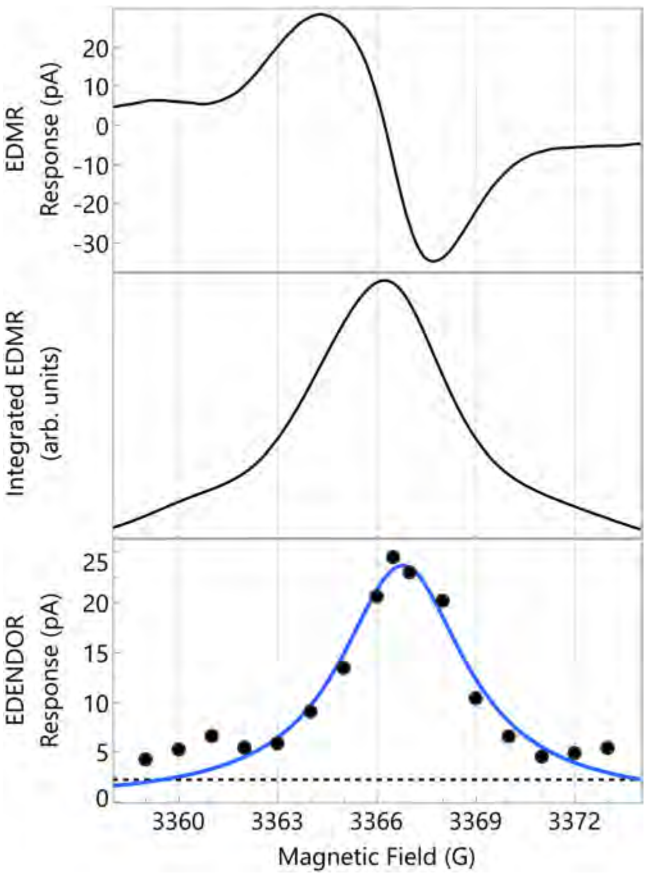

FIG. 5. EDMR response (top), integrated EDMR response (middle), and corresponding EDENDOR response (bottom) as a function of the magnetic field. In the EDENDOR measurement, the noise level is indicated in a black dashed line and a standard Lorentzian fit to the data is indicated in a blue solid line.

CONCLUSIONS

In this work, we show that the powerful magnetic resonance technique known as ENDOR can be utilized in a fully processed solid-state device, a bipolar junction transistor, using EDMR detection. Although this work is not the first observation of electrically detected ENDOR, to the best of our knowledge, the technique has not previously been demonstrated in a fully functional device of any kind. The apparatus and overall approach are relatively straightforward. Our work indicates that this approach could be widely applicable in semiconductor device studies.

ACKNOWLEDGMENTS

This work was supported by the Air Force Office of Scientific Research under Award No. FA9550-17-1-0242.

REFERENCES

[1] P. Lenahan and J. Conley, J. Vac. Sci. Technol. B **16**, 2134 (1998).
[2] J. A. Weil, J. R. Bolton, and J. E. Wertz, *Electron Paramagnetic Resonance: Elementary Theory and Practical Applications* (John Wiley & Sons, Inc., New York, 1994).
[3] L. Kevan and L. D. Kispert, *Electron Spin Double Resonance Spectroscopy* (John Wiley & Sons, Inc., New York, 1976).
[4] G. R. Eaton, S. S. Eaton, D. P. Barr, and R. T. Weber, *Quantitative EPR* (Springer, New York, 2010).
[5] C. J. Cochrane, P. M. Lenahan, and A. J. Lelis, J. Appl. Phys. **109**, 014506 (2011).
[6] P. M. Lenahan, C. J. Cochrane, J. P. Campbell, and J. T. Ryan, ECS Trans. **35**, 605 (2011).
[7] C. J. Cochrane, P. M. Lenahan, and A. J. Lelis, J. Appl. Phys. **105**, 064502 (2009).
[8] W. Gordy, *Theory and Applications of Electron Spin Resonance* (John Wiley & Sons, Inc., New York, 1980).
[9] D. Kaplan, I. Solomon, and N. F. Mott, J. Phys. Lett. **39**, 51 (1978).
[10] D. J. Lepine, Phys. Rev. B **6**, 436 (1972).
[11] D. J. McCrory, M. A. Anders, J. T. Ryan, P. R. Shrestha, K. P. Cheung, P. M. Lenahan, and J. P. Campbell, IEEE Trans. Device Mater. Reliab. **18**, 139 (2018).
[12] M. J. Mutch, P. M. Lenahan, and S. W. King, J. Appl. Phys. **119**, 094102 (2016).
[13] R. J. Waskiewicz, M. J. Mutch, P. M. Lenahan, and S. W. King, in *IEEE International Integrated Reliability Workshop* (IEEE, 2016), p. 99.
[14] M. J. Mutch, P. M. Lenahan, and S. W. King, Appl. Phys. Lett. **109**, 062403 (2016).
[15] M. J. Mutch, T. Pomorski, B. C. Bittel, C. J. Cochrane, P. M. Lenahan, X. Liu, R. J. Nemanich, J. Brockman, M. French, M. Kuhn, B. French, and S. W. King, Microelectron. Reliab. **63**, 201 (2016).
[16] J. T. Ryan, P. M. Lenahan, A. T. Krishnan, and S. Krishnan, J. Appl. Phys. **108**, 064511 (2010).
[17] C. J. Cochrane, P. M. Lenahan, and A. J. Lelis, Appl. Phys. Lett. **90**, 123501 (2007).
[18] W. L. Warren and P. M. Lenahan, Phys. Rev. B **42**, 1773 (1990).
[19] G. Feher, Phys. Rev. **114**, 1219 (1959).
[20] G. D. Watkins and J. W. Corbett, Phys. Rev. **134**, A1359 (1964).
[21] B. M. Hoffman, J. Martinsen, and R. A. Venters, J. Magn. Reson. **59**, 110 (1984).

[22]B. M. Hoffman, R. A. Venters, and J. Martinsen, J. Magn. Reson. **62**, 537 (1985).
[23]B. Biospin, in *Almanac 2012* (Bruker Instruments, 2012).
[24]B. Stich, S. Greulich-Weber, and J. M. Spaeth, Appl. Phys. Lett. **68**, 1102 (1996).
[25]F. Hoehne, L. Dreher, H. Huebl, M. Stutzmann, and M. S. Brandt, Phys. Rev. Lett. **106**, 187601 (2011).
[26]Q. J. Zhang, C. Jonas, A. A. Burk, C. Capell, J. Young, R. Callanan, A. K. Agarwal, J. W. Palmour, B. Geil, and C. Scozzie, Mater. Sci. Forum **600–603**, 1159 (2009).
[27]A. S. Grove, *Physics and Technology of Semiconductor Devices* (John Wiley & Sons, Inc., New York, 1967).
[28]A. L. P. Houseman, B.-H. Oh, M. C. Kennedy, C. Fan, M. M. Werst, H. Beinert, J. L. Markley, and B. M. Hoffman, Biochemistry **31**, 2073 (1992).

Applied Physics Letters ARTICLE scitation.org/journal/apl

Observation of electrically detected electron nuclear double resonance in amorphous hydrogenated silicon films

Cite as: Appl. Phys. Lett. **118**, 082401 (2021); doi: 10.1063/5.0041059
Submitted: 18 December 2020 · Accepted: 9 February 2021 ·
Published Online: 22 February 2021

View Online Export Citation CrossMark

Brian R. Manning,[a] James P. Ashton, and Patrick M. Lenahan

AFFILIATIONS

The Pennsylvania State University, University Park, Pennsylvania 16802, USA

[a]Author to whom correspondence should be addressed: brm5293@psu.edu

ABSTRACT

We report on the electrical detection of electron nuclear double resonance (EDENDOR) through spin-dependent tunneling transport in an amorphous hydrogenated silicon thin film. EDENDOR offers a many orders of magnitude improvement over classical ENDOR and is exclusively sensitive to paramagnetic defects involved in electronic transport. We observe hyperfine interactions with ^{1}H nuclei very close to silicon dangling bond defects. These observations substantially extend recent EDENDOR observations involving silicon vacancy defects and ^{14}N hyperfine interactions with fairly distant nitrogen atoms in 4H-SiC bipolar junction transistors. We have improved the detection scheme utilized in the earlier study by combining magnetic field modulation with RF amplitude modulation; this combination significantly improves the operation of the automatic power leveling scheme and the overall sensitivity.

The performance and reliability of solid-state electronic devices are dominated by point defects. Magnetic resonance techniques offer unparalleled analytical power in the identification of paramagnetic defects in semiconductors and insulators.[1] The basis for this magnetic resonance detection is electron paramagnetic resonance (EPR). Analysis of the EPR response provides information about the chemical nature and atomic-scale structure of defects present in the sample. The sensitivity of conventional EPR is roughly 10^{11} paramagnetic defects per mT linewidth.[2] Unfortunately, this number far exceeds the number of performance-limiting defects in technologically relevant nanoscale solid-state devices. The related EPR technique, electron nuclear double resonance (ENDOR), can provide extremely detailed information about the immediate surroundings of paramagnetic defects by observing small hyperfine interactions between paramagnetic defects and nearby magnetic nuclei.[3–6] Since the ENDOR response is typically several orders of magnitude smaller than that of conventional EPR, it is even less suitable than conventional EPR for studies of nanoscale devices. The sensitivity of conventional EPR can be enormously improved via electrically detected magnetic resonance (EDMR). EDMR is an EPR-based technique in which the EPR response is extracted from an electrical measurement that monitors spin-dependent transport.[7–14] EDMR sensitivity is typically around seven orders of magnitude better than classical EPR detection.[15,16] EDMR has proven to be quite valuable in studies of atomic-scale imperfections in nanoscale solid-state electronics as well as semiconducting and insulating materials.[11–14] By utilizing EDMR detection, the sensitivity of ENDOR may be enhanced by many orders of magnitude with electrically detected ENDOR (EDENDOR). EDENDOR was first reported on relatively large volume samples.[6,17] Quite high sensitivity EDENDOR was recently reported in measurements on a fully functional 4H-SiC bipolar junction transistor.[18,19] In this study, we extend the earlier work, all of which involves spin dependent recombination (SDR), to EDEDNOR detected through spin dependent trap assisted tunneling (SDTAT). More importantly, the earlier studies all dealt with matrix ENDOR. In matrix ENDOR, the response from magnetic nuclei distant from paramagnetic defects is observed in which hyperfine interactions are not measured. In this work, we extract hyperfine parameters with modest precision.

In EPR, the response of paramagnetic defect centers to the simultaneous application of a quasi-static field and small RF or microwave-frequency field is observed. A difference in energy is caused by the interactions of the electron magnetic moment with a magnetic field. The application of an oscillating magnetic field with frequency, ν, times Planck's constant, h, equal to this difference in energy induces resonance. For a free electron unperturbed by its local surroundings, the resonance condition is[1]

$$\Delta E = h\nu = g_e \mu_B B. \quad (1)$$

Here, ΔE is the difference in energy between the spin states, g_e is the Landé g value ($g_e = 2.002\,32\ldots$), μ_B is the Bohr magneton, and B is the magnitude of the large quasi-static magnetic field. The resonance condition is altered by a defect's surroundings. The most common mechanisms of these alterations are spin–orbit coupling and electron-nuclear hyperfine interactions. Taking into account these factors, the resonance condition is modified and becomes[1,20]

$$\Delta E = h\nu = g\mu_B B + \sum\nolimits_i m_i A_i. \quad (2)$$

Here, g is a second rank tensor and m_i is the nuclear spin quantum number of the ith nearby magnetic nucleus; A_i is also typically represented by a second rank tensor representing the electron-nuclear hyperfine coupling. However, for the observation reported herein, the hyperfine interactions may be taken to be constants. By measuring the magnetic field at resonance and the frequency ν, the physical and chemical nature of atomic scale defects can be identified.

The EDMR in this study is detected through SDTAT.[21–23] In SDTAT, electrons tunnel from defect to defect. The tunneling is forbidden between two adjacent defects if unpaired electrons at both defects have the same spin quantum number by the Pauli exclusion principle. However, if we flip the spin of one of the unpaired electrons, the previously forbidden tunneling event becomes allowed. This is observed as an increase in current through the device.[24]

In classical ENDOR measurements, the EPR response is first measured.[25] The magnetic field is then held constant at a field that results in EPR microwave absorption. An oscillating magnetic field with the field vector perpendicular to the large applied field is swept over a frequency range that induces nuclear resonance at a site near the defect observed in EPR. When this occurs, the amplitude of the EPR response can change.[25] Measuring the EPR amplitude as a function of frequency allows for a measurement of the frequency, ν_n, at which nuclear magnetic resonance (NMR) takes place.

The ENDOR response is easiest to describe for the case of a defect with electron spin $(S) = \frac{1}{2}$ and a nearby nuclear spin $(I) = \frac{1}{2}$ for a single isotropic value of hyperfine interaction, a. In this case, the ENDOR response condition will be given by $\nu \cong \left|\nu_n \pm \frac{a}{2}\right|$ (this is the case for our study). Somewhat more complex responses can occur. For example, if $I > \frac{1}{2}$, the presence of nuclear quadrupole moments changes the ENDOR response frequency conditions to $\nu \cong \left|\frac{a}{2} \pm \nu_n \pm Q\right|$, where Q depends upon the electric field gradient at the nucleus and the nuclear quadrupole moment.

The EDENDOR spectrometer design used in that study is shown in Fig. 1 and is described in detail in a recent paper.[19] The EDENDOR spectrometer used in this study is somewhat modified from the one described in earlier work. The sample is placed into the microwave cavity and aligned with a single loop antenna. The NMR RF sweep is supplied to this loop via a Fluke-291 arbitrary waveform generator (AWG). In prior EDENDOR experiments, the magnetic field, B_0, was fixed and the NMR frequency sweep was 100% amplitude modulated for phase-sensitive detection. In the work reported here, we improve upon the detection sensitivity of the earlier study by using double modulation. We modulated both the B_0 field and utilized a 100% amplitude modulation of the NMR RF frequency sweep. Double modulation was used in conjunction with an automatic power leveling scheme via a proportional integral differential (PID) controller, which almost completely removes the non-resonant-background that otherwise obscures the EDENDOR spectrum.[17,19]

We conducted an EDENDOR experiment on a 10 nm amorphous hydrogenated silicon thin film (a-Si:H) (99% Si, 1% H) on p-Si (100) wafers with Ti/Al metal contacts with an area of 0.020 cm^2. The spin density in these structures is approximately 5×10^{18} cm^{-3}; thus, the number of paramagnetic defect sites in the sample is about 10^{11} spins. The film in this study was deposited via plasma enhanced chemical vapor deposition. The device was diced from the wafer via a diamond scribe and mounted to a printed circuit board. The electrical

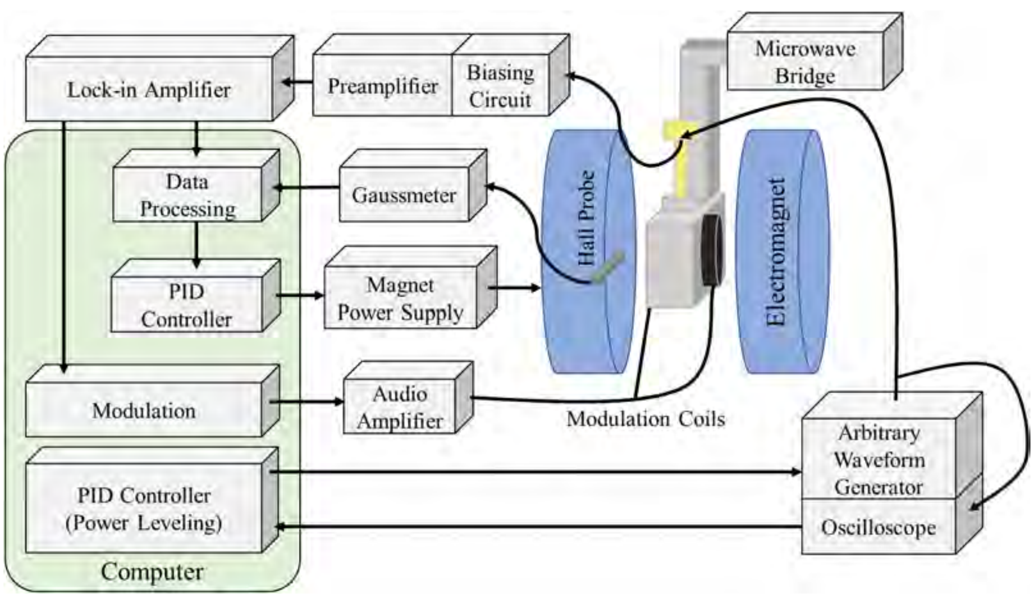

FIG. 1. EDMR/EDENDOR spectrometer schematic.

connections from the device to the leads were made via wire bond. These measurements were performed at room temperature. The EDENDOR measurements were taken at the magnetic field at the center of the EDMR spectrum (zero-crossing), as well as several points on each side of the center. The representative EDMR spectrum is illustrated in Fig. 2. EDENDOR measurements are limited by multiple sources of noise, which influence the EDMR detection such as shot, flicker, and thermal noise.[26] Due to the extremely high defect density of this device, the EDMR response is quite strong and these noise sources do not prevent an extremely high EDMR signal-to-noise ratio. The EDMR response is consistent with SDTAT currents through silicon dangling bond sites.[27] The center field of the EDMR response is 332.2 mT and the response is ≈0.7 mT wide. The measured zero-crossing $g = 2.0055 \pm 0.0003$ is consistent with silicon dangling bonds, a result widely reported on a-Si:H samples analyzed using EPR techniques.[12,15,28,29]

To observe the EDENDOR response, the magnetic field was modulated at 3350 Hz with an amplitude of 0.4 mT (approximately half the linewidth). The RF was 100% amplitude modulated at 250 Hz. This modulated response is detected through a virtual lock-in amplifier (VLIA) with two demodulation stages. The VLIA was written in LabVIEW 2018 and utilizes two mixing stages in which it is multiplied by a reference sinusoid with an adjustable phase. After each mixing phase, there is a low-pass filter with an adjustable time constant. The first demodulates the field modulated response with a small time constant of approximately 0.6 ms. The short first stage time constant is necessary in order to pass the 250 Hz amplitude modulated response to the second lock-in. To demonstrate that the response of the system is EDENDOR and not some artifact, we repeated the identical measurement but with the field shifted from the EDMR resonance condition of 332.2 mT to 300 mT, far from the EDMR resonance condition. EDENDOR results of the on- and off-EDMR resonance field are illustrated in Fig. 3. The signal-to-noise ratio was optimized using adaptive signal averaging.[30–32] The extremely large difference between the on- and off-EDMR resonance conditions clearly identifies the upper trace taken at the resonance field of 332.2 mT as EDENDOR. Note the arrows directed at the peaks of the ENDOR response at 12.58 MHz and 15.63 MHz. The two peaks correspond to the EDENDOR response of silicon dangling bonds interacting with nearby ^{1}H nuclei. We know that this is so because at a field of 332.2 mT, the ENDOR response for ^{1}H nuclei close to the dangling bond defects should be a two-line spectrum centered around the isolated hydrogen nucleus NMR frequency of 14.11 MHz. The center of the two peaks we observe is at $\frac{(12.58+15.68)}{2}$ MHz $= 14.10$ MHz, within experimental error of the anticipated value of 14.11 MHz. The asymmetry of the peaks is to be expected and is indicative of the sign of the coupling constant.[25,33] From inspection of the separation of the two ^{1}H peaks, we extract a hyperfine coupling of ≈3 MHz (±0.2 MHz). This value is consistent within the range of hyperfine couplings reported for ^{1}H in a-Si:H observed in prior work by Brandt *et al.*[28] A weak peak is apparently present in our response around 10 MHz. It is possible that this peak corresponds to hyperfine interactions with nearby ^{29}Si nuclei. However, due to the asymmetry of the peaks, it is likely we observe the high frequency peak and the low frequency peak is underneath the noise floor of our measurement.

Additional verification that the response shown in Fig. 4 is EDENDOR is provided by a plot of the 15.63 MHz peak amplitude as a function of magnetic field. The peak amplitude should approximately track the field modulated EDMR response.[25] Figure 4 shows that this is the case.

The close correspondence between the EDENDOR amplitude and the EDMR response strongly supports the identification ^{1}H

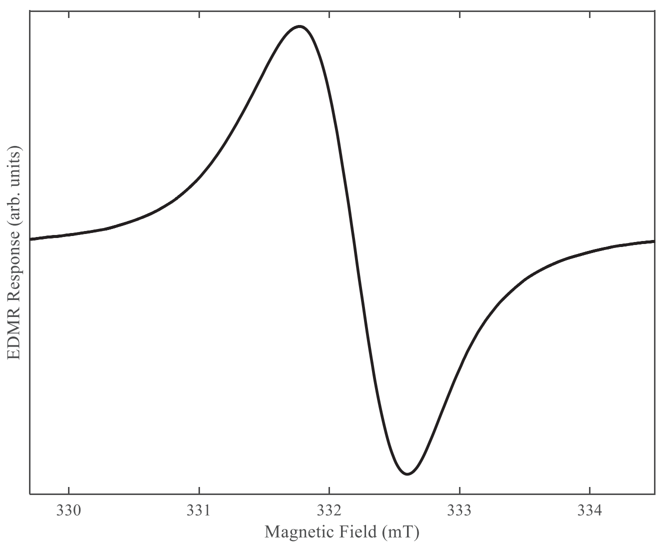

FIG. 2. A representative EDMR trace on an a-Si:H sample utilized in EDENDOR measurements. The peak-to-peak linewidth is about 0.7 mT and the zero-crossing *g*, which is the g-value corresponding to the magnetic field halfway between the top and bottom peaks of the spectrum, is 2.0055, the value generally found for silicon dangling bonds in amorphous hydrogenated silicon.

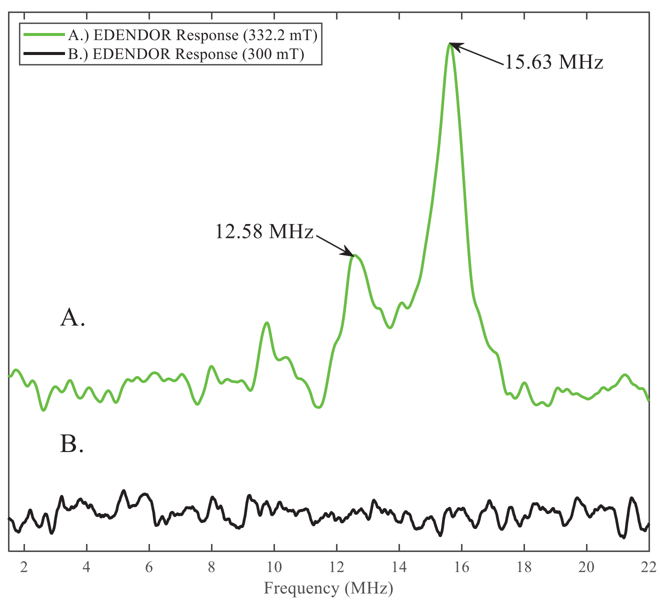

FIG. 3. EDENDOR response of the a-Si:H sample. The upper trace (in green) was taken at the magnetic field corresponding to the center of the EDMR response, in this case 332.2 mT. The lower (black) trace was taken at a field of 300 mT, which is at a field far off the EDMR resonance.

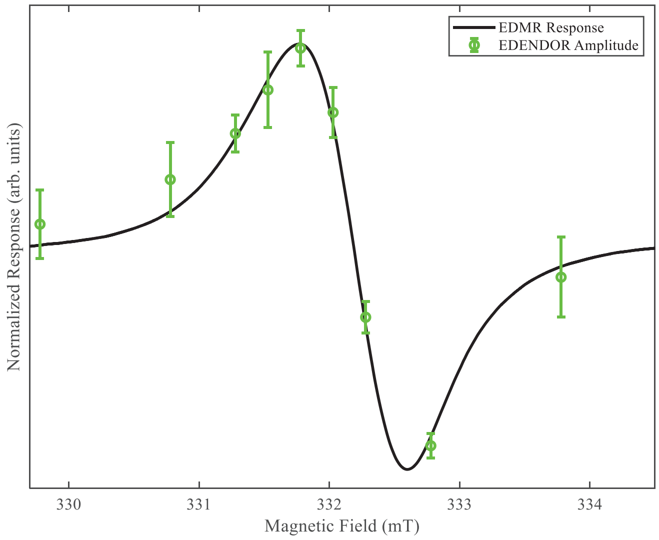

FIG. 4. EDENDOR response of the a-Si:H sample at 15.63 MHz vs magnetic field. Error bars are representative of the amplitude of noise and scale with the number of scans taken at each field point. The ENDOR points are shifted slightly toward the lower field to account for a field offset introduced by the software.

interactions with Si dangling bonds. Most importantly, these observations extend our earlier observations of EDENDOR from nuclei more distant from the paramagnetic defects. Those earlier observations did not allow any measure of hyperfine parameters. The EDENDOR results reported here allows the measurement, albeit with modest precision, of ^{1}H-Si hyperfine interactions.

In conclusion, we demonstrate EDENDOR detection of ^{1}H nuclei interactions nearby Si dangling bond defects in a-Si:H. We extract a ^{1}H hyperfine coupling of 3 MHz, consistent with coupling constants corresponding to ^{1}H hyperfine interactions in a-Si:H from prior measurements.[28] These observations extend recent EDENDOR measurements in a 4H-SiC bipolar junction transistor.[12,13] The results presented are consistent with ENDOR of magnetic nuclei fairly close to the defect. We believe this approach would be widely applicable to ENDOR studies of many semiconducting and insulating materials and solid-state electronic devices. The most important criterion for this approach is the ability to observe EDMR with a reasonable high signal-to-noise ratio in a system with a significant population of magnetic nuclei.

See the supplementary material for a picture of the virtual lock-in amplifier's LabVIEW code (Fig. S1). The picture shows the case for double modulation as described within this manuscript.

This work was supported by the Air Force Office of Scientific Research under Award No. FA9550-17-1-0242.

DATA AVAILABILITY

The data that support the findings of this study are available from the corresponding author upon reasonable request.

REFERENCES

[1] J. A. Weil, J. R. Bolton, and J. E. Wertz, *Electron Paramagnetic Resonance: Elementary Theory and Practical Applications* (John Wiley & Sons, Inc., New York, 1994).
[2] G. R. Eaton, S. S. Eaton, D. P. Barr, and R. T. Weber, *Quantitative EPR* (Springer Wien New York, 2010).
[3] L. D. Kispert and L. Piekara-Sady, *ENDOR Spectroscopy* (Springer Science, New York, 2006).
[4] A. B. Wolbarst, Rev. Sci. Instrum. **47**, 255 (1976).
[5] B. M. Hoffman, J. Martinsen, and R. A. Venters, J. Magn. Reson. **59**, 110 (1984).
[6] B. Stich, S. Greulich-Weber, and J. M. Spaeth, Appl. Phys. Lett. **68**, 1102 (1996).
[7] C. Boehme and H. Malissa, eMagRes **6**, 83 (2017).
[8] C. J. Cochrane, P. M. Lenahan, and A. J. Lelis, J. Appl. Phys. **109**, 014506 (2011).
[9] D. Kaplan, I. Solomon, and N. F. Mott, J. Phys. Lett. **39**, 51 (1978).
[10] P. M. Lenahan and M. A. Jupina, Colloids Surf. **45**, 191 (1990).
[11] C. J. Cochrane, P. M. Lenahan, and A. J. Lelis, J. Appl. Phys. **105**, 064502 (2009).
[12] M. J. Mutch, P. M. Lenahan, and S. W. King, J. Appl. Phys. **119**, 094102 (2016).
[13] C. J. Cochrane, P. M. Lenahan, and A. J. Lelis, Appl. Phys. Lett. **100**, 023509 (2012).
[14] D. J. Meyer, P. M. Lenahan, and A. J. Lelis, Appl. Phys. Lett. **86**, 023503 (2005).
[15] M. Stutzmann, M. S. Brandt, and M. W. Bayerl, J. Non-Cryst. Solids **266-269**, 1 (2000).
[16] G. Kawachi, C. F. O. Graeff, M. S. Brandt, and M. Stutzmann, Phys. Rev. B **54**, 7957 (1996).
[17] F. Hoehne, L. Dreher, H. Huebl, M. Stutzmann, and M. S. Brandt, Phys. Rev. Lett. **106**, 187601 (2011).
[18] R. J. Waskiewicz, B. R. Manning, D. J. McCrory, and P. M. Lenahan, J. Appl. Phys. **126**, 125709 (2019).
[19] B. R. Manning, R. J. Waskiewicz, D. J. McCrory, and P. M. Lenahan, Rev. Sci. Instrum. **90**, 123111 (2019).
[20] W. Gordy, *Theory and Applications of Electron Spin Resonance* (John Wiley & Sons, Inc., New York, 1980).
[21] J. T. Ryan, P. M. Lenahan, A. T. Krishnan, and S. Krishnan, J. Appl. Phys. **108**, 064511 (2010).
[22] C. Boehme, J. Behrends, K. v Maydell, M. Schmidt, and K. Lips, J. Non-Cryst. Solids **352**, 1113 (2006).
[23] D. J. McCrory, P. M. Lenahan, D. M. Nminibapiel, D. Veksler, J. T. Ryan, and J. P. Campbell, IEEE Trans. Nucl. Sci. **65**, 1101 (2018).
[24] J. P. Campbell, P. M. Lenahan, A. T. Krishnan, and S. Krishnan, J. Appl. Phys. **103**, 044505 (2008).
[25] L. Kevan and L. Kispert, *Electron Spin Double Resonance Spectroscopy* (John Wiley & Sons, Inc., New York, 1994).
[26] A. Van der Ziel, *Noise in Solid State Devices and Circuits* (Wiley, 1986).
[27] M. A. Anders, P. M. Lenahan, C. J. Cochrane, and J. Van Tol, J. Appl. Phys. **124**, 215105 (2018).
[28] M. S. Brandt, M. W. Bayerl, M. Stutzmann, and C. F. O. Graeff, J. Non-Cryst. Solids **227-230**, 343 (1998).
[29] T. W. Herring, S. Y. Lee, D. R. McCamey, P. C. Taylor, K. Lips, J. Hu, F. Zhu, A. Madan, and C. Boehme, Phys. Rev. B **79**, 195205 (2009).
[30] C. J. Cochrane and P. M. Lenahan, J. Magn. Reson. **195**, 17 (2008).
[31] C. J. Cochrane, Rev. Sci. Instrum. **83**, 105108 (2012).
[32] B. R. Manning, C. J. Cochrane, and P. M. Lenahan, Rev. Sci. Instrum. **91**, 033106 (2020).
[33] G. Feher, C. S. Fuller, and E. A. Gere, Phys. Rev. **107**, 1462 (1957).

Submitted to *Applied Physics Letters*, August 6, 2021

"Electrically Detected Electron Nuclear Double Resonance in Amorphous Hydrogenated Boron Thin Films"

By: K.J. Myers, B.R. Manning, and P.M. Lenahan

TITLE

Electrically Detected Electron Nuclear Double Resonance in Amorphous Hydrogenated Boron Thin Films

AUTHORS

Kenneth J. Myers[1,a)], Brian Manning[2], Patrick M. Lenahan[3]

AFFILIATIONS

[1]Intercollege Graduate Degree Program in Materials Science and Engineering, The Pennsylvania State University, University Park, PA 16802, USA

[2]High Frequency Technology Center, Keysight Technologies, Santa Rosa, CA 95403, USA

[3]Department of Engineering Science and Mechanics, The Pennsylvania State University, University Park, PA 16802, USA

[a)]Author to whom correspondence should be addressed: kjm5579@psu.edu

ABSTRACT

We observe electrically detected electron nuclear double resonance (EDENDOR) via spin-dependent trap-assisted tunneling in amorphous hydrogenated boron thin films. This is useful because combining electrical detection with the classical ENDOR allows for much greater sensitivity and specific selectivity to defects involved in electronic transport. In this study, we observe EDENDOR responses from both ^{10}B and ^{11}B likely interacting with carbon impurity sites.

BODY

Electron paramagnetic resonance (EPR) and its related techniques have long been the most powerful tools for studying the physical and chemical nature of point defects in semiconducting and insulating materials.[1,2] Conventional continuous wave EPR, the most common form of the measurement, has a sensitivity of about 10^{11} paramagnetic defects per mT linewidth.[3] Of the techniques that stem from EPR, electron nuclear double resonance (ENDOR) provides the most detailed information about paramagnetic point defects and nearby magnetic nuclei.[2,4,5]. Neither conventional EPR nor the much less sensitive conventional ENDOR technique has the sensitivity to detect defects in fully processed nano-/micro-scale devices.

The sensitivity of conventional EPR can be greatly improved through the utilization of electrically detected magnetic resonance (EDMR).[6,7] EDMR detects EPR through spin-dependent changes in device current (or voltage) at the resonance condition. EDMR not only improves the sensitivity of EPR from 10^{11} to 10^{4} defects per mT linewidth, but it also makes the measurement exclusively sensitive to defects involved in electronic transport.[8,9] By utilizing ENDOR via EDMR detection, we can improve its sensitivity while allowing for measurements in device structures such as bipolar junction transistors and capacitors.[4,5,10–12] This process is called electrically detected ENDOR (EDENDOR). Initial reports of EDENDOR involved photoconductivity-based techniques on fairly large Si/SiO_2 metal-oxide-semiconductor capacitors.[5,12] More recently, EDENDOR has been reported on fully processed semiconductor devices and on an amorphous hydrogenated silicon thin films. These recent observations utilize spin-dependent recombination (SDR) and spin-dependent trap-assisted tunneling (SDTAT). The recent work offers quite high sensitivity, extending the capabilities of ENDOR to micro-/nano-scale devices. In this report, we extend this highly sensitive EDENDOR approach to measurements in a new system: carbon-doped amorphous hydrogenated boron thin films. We observe matrix ENDOR responses from both ^{10}B and ^{11}B, presumably interacting with carbon-related impurities involved in trap-assisted tunneling.[13–17]

A brief explanation of EPR and ENDOR may be useful. In conventional EPR, the sample under study is exposed to microwave radiation with frequency ν and a large, slow varying magnetic field ($\overrightarrow{B_0}$). For the simplest case of an electron which does not otherwise interact with its environment, the energy difference between the two allowed spin states is given by:

$$\Delta E = g_e \mu_B B_0, \tag{1}$$

where g_e is the free electron's Landé g-factor ($g_e = 2.00232 \ldots$) and μ_B is the Bohr magneton. When ν times Planck's constant is equal to the separation between the spin states, the electron will transition from one spin state to the other. In this simple case, the resonance condition is given by:

$$h\nu = g_e \mu_B B_0. \tag{2}$$

In a real paramagnetic site, the resonance condition is generally more complex. The two most commonly observed deviations from expression (2) are due to spin-orbit coupling and nuclear hyperfine interactions. Spin-orbit coupling changes the Landé g-factor to a second-ranked tensor while nuclear hyperfine interactions with nearby magnetic nuclei add additional terms which depend on the location of the nuclei. These effects make the resonance condition:

$$h\nu = g\mu_B B_0 + \sum_i m_i A_i, \tag{3}$$

where m_i is the nuclear spin quantum number of the ith nucleus near the defect and A_i is the nuclear hyperfine contribution of the ith nucleus. A_i is often also expressed as a second-ranked tensor; however, for the purposes of this study, the nuclear hyperfine interactions can be considered as isotropic.

In this study we detect EDENDOR through SDTAT EDMR. SDTAT is observed when an electron tunnels between two defects.[18–23] In SDTAT, these two paramagnetic sites contain an unpaired electron. If both electrons have the same spin quantum number, it is impossible for an electron to tunnel from one defect to the other due to the Pauli Exclusion Principle. However, at resonance one of the spins may be flipped, allowing tunneling to occur. This alters the tunneling current and results in the observed EDMR signal.

A classical ENDOR measurement[24] typically begins by making an EPR measurement on the sample under study. Once the EPR spectrum is observed, the magnetic field is then set to a field at which the EPR response is detected. An RF frequency oscillating field is applied and swept to induce the nuclear magnetic resonance (NMR) response of magnetic nuclei. This changes the amplitude of the EPR response when the NMR resonance condition of nearby nuclei is satisfied. By measuring the change of the EPR signal as a function of the RF oscillation, one extracts the frequencies at which magnetic resonance of nearby nuclei takes place. These frequencies allow for the identification of magnetic nuclei near the defect and, in some cases, their location with respect to said defect. The ENDOR spectrum is most easily described in the case of a defect containing an electron spin with a nearby nuclear spin of $I = \frac{1}{2}$ and an isotropic hyperfine constant a. For such a system, the ENDOR response is located at $\nu = \left|\nu_n \pm \frac{a}{2}\right|$, where ν_n is the nuclear frequency. The two possible responses in this case are when half the hyperfine coupling constant is greater than the nuclear frequency $\left(\left|\frac{a}{2}\right| > \nu_n\right)$ or when half the hyperfine coupling constant is less than half the nuclear frequency $\left(\left|\frac{a}{2}\right| < \nu_n\right)$, as is the case for our study. The former will result a spectrum with two lines centered about $\left|\frac{a}{2}\right|$ and split by $2\nu_n$, while the latter gives a similar two-line spectrum centered about ν_n and separated by $|a|$. More complex spectra can occur depending on the system's spin states. For example, higher spin nuclei with $I > \frac{1}{2}$, nuclear quadrupole moments can alter the ENDOR response to $\nu = \left|\nu_n \pm \frac{a}{2} \pm Q\right|$, wherein Q accounts for the interaction between the nuclear quadrupole moment and local electric field gradients. In our study, both boron nuclei have high spin and thus quadrupole moments. We are only able to observe fairly distant nuclei and presumably detect the quadrupole interactions through a substantial broadening of the EDENDOR response.

Our EDENDOR spectrometer is described in recent papers with alterations described herein.[11,25] The device is mounted on a thin circuit board and connected to a set of electrical leads and placed inside of a TE_{102} cavity in which a 5-turn solenoid used for the ENDOR frequency sweep is placed around the device. An Agilent 83732B Synthesizer, capable of providing 15 dBm (32mW) of microwave power, is connected to an isolator, circulator, and detector diode before reaching the microwave cavity. Additionally, a Marconi 2026Q RF generator supplies a 100% amplitude modulated frequency sweep to the solenoid in conjunction with a LeCroy WaveRunner 6100A 1GHz oscilloscope for output power control. The LeCroy oscilloscope is used in tandem with an in-house PID controlling software in order to idealize the waveform shape and power control. A Bruker ER4111VT cold finger temperature system maintains a stable low temperature at the sample. The spectrometer includes a 4-inch Resonance Instruments electromagnet, a Lakeshore 475 DSP Temperature Compensated Gaussmeter and Hall probe, and a HP 6268B power supply. The preamplifier/voltage source for the device is a Stanford Research Systems Model SR570.

The devices utilized in this study are 500nm a-B:H thin films deposited via PECVD on (100) Si substrates with 1μm Al gates capped with 10nm Ti. The a-B:H contains approximately

9% hydrogen and 4% carbon. We utilized a bias of +5V to the metal to monitor the spin-dependent tunneling current through the boron films. All measurements were performed at 250K.

The SDTAT EDMR response of the a-B:H films at 250K is shown in Fig. 1. This response is independent of orientation in the external magnetic field, indicating that the measured defects are present in the bulk a-B:H film and not located at the a-B:H/Si interface. The measured EDMR spectrum contains a broad line and a much sharper response in the middle. The response is approximately 1mT wide and the broader feature is roughly 4mT wide. We tentatively assign the narrow center line to paramagnetic defects involving carbon atoms while the broad line is attributed to boron-related paramagnetic centers.[17] The boron-related EPR spectra are broad and featureless as would be expected due to the presence of hyperfine interactions from the 20% naturally abundant ^{10}B ($S = 3$) and 80% naturally abundant ^{11}B $\left(S = \frac{3}{2}\right)$. The resulting EDMR spectrum is the broad line shown in Fig. 1.

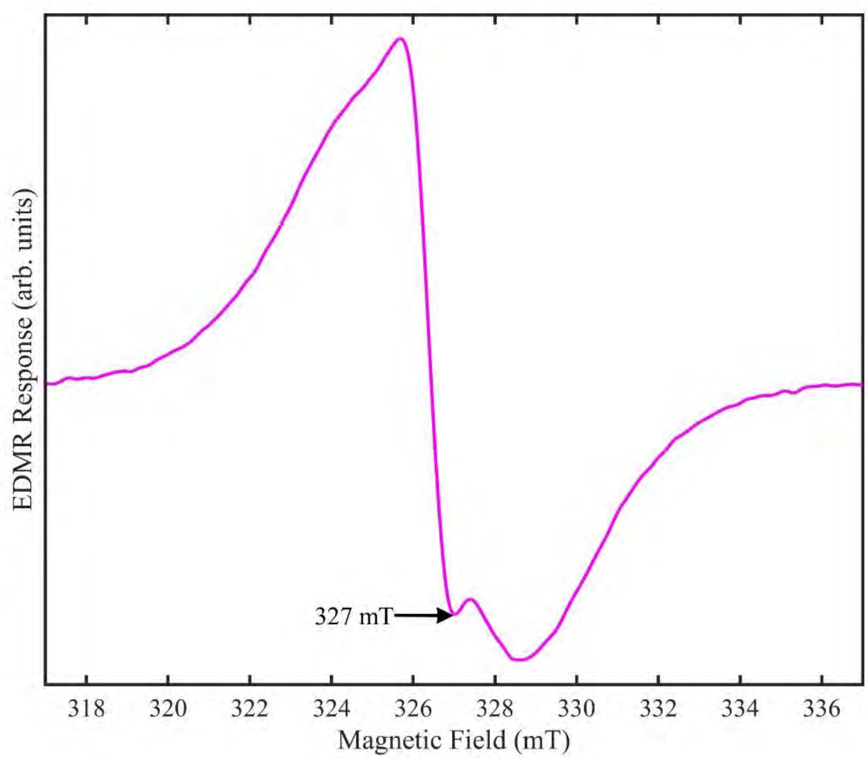

Fig. 1: The SDTAT EDMR response of the a-B:H films at +5V and 250K for a supplied microwave frequency of $\nu \cong 9.173$GHz. The arrow indicates the static magnetic field at which we perform EDENDOR.

Fig. 2A shows the EDENDOR response in the a-B:H films using the adaptive signal averaging method introduced by Manning *et al*.[26] As previously mentioned, the externally applied magnetic field is held constant at 327mT. For this magnetic field, three EDENDOR peaks are observed. The low-frequency peak is extremely wide and centered about the nuclear frequency of ^{10}B (≈1.45MHz). Two arrows in the figure on the low-frequency end indicate a potential splitting in this peak, however this may be a result of the marginal signal to noise ratio. The frequency of the measured response is centered at 1.43MHz ± 0.03MHz. The higher frequency peaks appear at 3.15MHz and 5.81MHz which are centered at 4.48MHz ± 0.03MHz $\left(\frac{3.15+5.81}{2} MHz = 4.48MHz\right)$. The nuclear frequency of isolated ^{11}B is 4.47MHz, a frequency consistent with our observations. Additionally, we are able to extract the approximate hyperfine coupling constant of ^{11}B due to the separation in the EDENDOR peaks. Our estimated hyperfine constant for ^{11}B is ≈2.65MHz. Fig. 2B shows a trace at a field far off the resonance condition, at 297mT, with equivalent signal averaging. The observed peaks are no longer present at this magnetic field, confirming that the response observed at 327mT is due to EDENDOR. We are unable to extract any information about the quadrupole interactions except to note that the EDENDOR response is quite broad. Some of this broadening is likely due to unresolved quadrupole interactions.

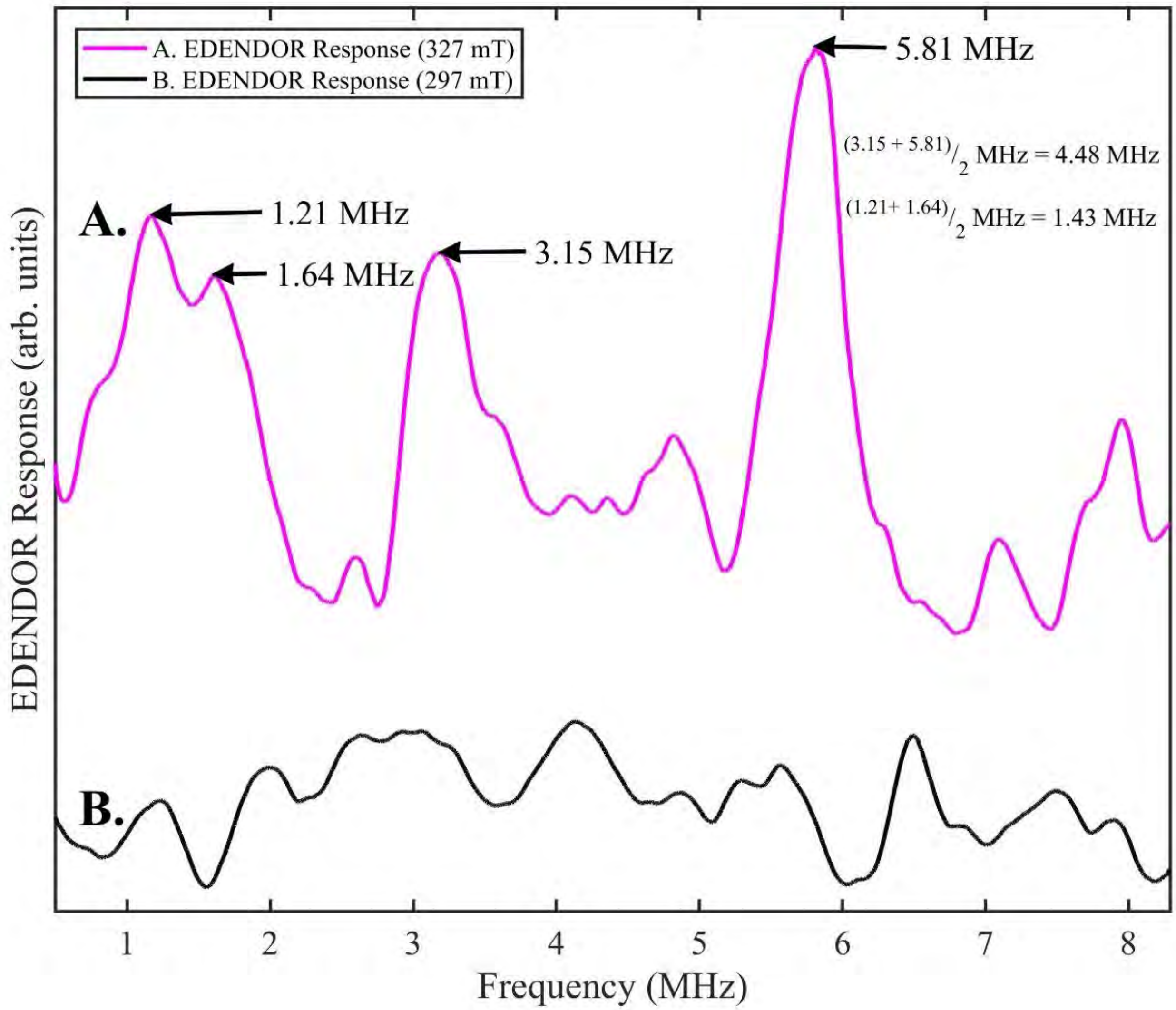

Fig. 2: The SDTAT EDENDOR response of the a-B:H films at A. 327mT (pink) for on-resonance and B. 297mT (black) for off-resonance. All EDMR variables were kept constant as described in Fig. 1.

In conclusion, we demonstrate EDENDOR in a-B:H films, detecting ENDOR from both ^{10}B and ^{11}B isotopes. Our results, coupled with two other recent reports,[10,11] show that the EDENDOR technique measurements using a relatively simple apparatus should be possible in many systems. To the extent that this is the case, our work suggests that EDENDOR may be widely applicable in studies of transport in semiconductor devices.

ACKNOWLEDGEMENTS

This work was supported by the Air Force Office of Scientific Research under Award No. FA9550-17-1-0242. Additionally, we would like to thank Dr. Sean King and Intel Corporation for supplying the devices used in this study.

DATA AVAILABILITY

The data that support the findings of this study are available from the corresponding author upon reasonable request.

REFERENCES

[1] W. Gordy, *Theory and Applications of Electron Spin Resonance* (John Wiley & Sons, New York, 1980).

[2] L. Kevan and L.D. Kispert, *Electron Spin Double Resonance Spectroscopy* (John Wiley & Sons, New York, 1976).

[3] G.R. Eaton, S.S. Eaton, D.P. Barr, and R.T. Weber, *Quantitative EPR* (Springer Vienna, Vienna, 2010).

[4] B.M. Hoffman, J. Martinsen, and R.A. Venters, J. Magn. Reson. **59**, 110 (1984).

[5] B. Stich, S. Greulich-Weber, and J.M. Spaeth, Appl. Phys. Lett. **68**, 1102 (1996).

[6] D. Kaplan, I. Solomon, and N.F. Mott, J. Phys. Lettres **39**, 51 (1978).

[7] D.J. Lepine, Phys. Rev. B **6**, 436 (1972).

[8] G. Kawachi, C.F.O. Graeff, M.S. Brandt, and M. Stutzmann, Phys. Rev. B - Condens. Matter Mater. Phys. **54**, 7957 (1996).

[9] M. Stutzmann, M.S. Brandt, and M.W. Bayerl, J. Non. Cryst. Solids **266–269**, 1 (2000).

[10] R.J. Waskiewicz, B.R. Manning, D.J. McCrory, and P.M. Lenahan, J. Appl. Phys. **126**, (2019).

[11] B.R. Manning, J.P. Ashton, and P.M. Lenahan, Appl. Phys. Lett. **118**, (2021).

[12] F. Hoehne, L. Dreher, H. Huebl, M. Stutzmann, and M.S. Brandt, Phys. Rev. Lett. **106**, 1 (2011).

[13] J. Reinke, R. Mueller, M. Feege, S. Greulich-Weber, and J.M. Spaeth, Mater. Sci. Forum **143–**

4, 63 (1994).

[14] G. Jeschke, M. Kroschel, and M. Jansen, J. Non. Cryst. Solids **260**, 216 (1999).

[15] J.R. Toledo, D.B. De Jesus, M. Kianinia, A.S. Leal, C. Fantini, L.A. Cury, G.A.M. Sáfar, I. Aharonovich, and K. Krambrock, Phys. Rev. B **98**, 1 (2018).

[16] H. Tezuka, A.R. Stegner, A.M. Tyryshkin, S. Shankar, M.L.W. Thewalt, S.A. Lyon, K.M. Itoh, and M.S. Brandt, Phys. Rev. B - Condens. Matter Mater. Phys. **81**, 4 (2010).

[17] U. Gercke and C.D. Stems, J. Less-Common Met. **67**, 245 (1979).

[18] M.J. Mutch, P.M. Lenahan, and S.W. King, J. Appl. Phys. **119**, (2016).

[19] S.J. Moxim, J.P. Ashton, P.M. Lenahan, M.E. Flatte, N.J. Harmon, and S.W. King, IEEE Trans. Nucl. Sci. **67**, 228 (2020).

[20] J.H. Stathis, Appl. Phys. Lett. **68**, 1669 (1996).

[21] J.T. Ryan, P.M. Lenahan, A.T. Krishnan, and S. Krishnan, J. Appl. Phys. **108**, (2010).

[22] Y. Miura and S. Fujieda, Japanese J. Appl. Physics, Part 1 Regul. Pap. Short Notes Rev. Pap. **40**, 2840 (2001).

[23] M.S. Brandt, M.W. Bayerl, M. Stutzmann, and C.F.O. Graeff, J. Non. Cryst. Solids **227–230**, 343 (1998).

[24] C.P. Slichter, *Principles of Magnetic Resonance*, 3rd ed. (Springer Berlin Heidelberg, Berlin, Heidelberg, 1990).

[25] B.R. Manning, R.J. Waskiewicz, D.J. McCrory, and P.M. Lenahan, Rev. Sci. Instrum. **90**, (2019).

[26] B.R. Manning, C.J. Cochrane, and P.M. Lenahan, Rev. Sci. Instrum. **91**, (2020).

Review of Scientific Instruments | ARTICLE | scitation.org/journal/rsi

Apparatus for electrically detected electron nuclear double resonance in solid state electronic devices

Cite as: Rev. Sci. Instrum. 90, 123111 (2019); doi: 10.1063/1.5123619
Submitted: 7 August 2019 • Accepted: 30 November 2019 •
Published Online: 23 December 2019

View Online Export Citation CrossMark

Brian R. Manning,[1,a] Ryan J. Waskiewicz,[1,b] Duane J. McCrory,[2,c] and Patrick M. Lenahan[1,d]

AFFILIATIONS

[1] The Pennsylvania State University, University Park, Pennsylvania 16802, USA
[2] High Frequency Technology Center, Santa Rosa, California 95403, USA

[a] brm5293@psu.edu
[b] rjw5352@psu.edu
[c] duane.mccrory@keysight.com
[d] pmlesm@engr.psu.edu

ABSTRACT

We have developed a sensitive electron nuclear double resonance spectrometer in which the detection takes place through electrically detected magnetic resonance. We demonstrate that the spectrometer can provide reasonably high signal to noise spectra of ^{14}N interactions with deep level centers in a fully processed bipolar junction transistor at room temperature.

INTRODUCTION

The identification of defects that alter the performance of solid-state electronic devices is a topic of widespread interest. The family of electron paramagnetic resonance (EPR) techniques offer unrivaled analytical power in the identification of these defects; however, the sensitivity of conventional EPR under typical circumstances is about 10×10^9 defects.[1] This number far exceeds the number of performance-limiting defects in technologically relevant solid-state devices. Electrically detected magnetic resonance (EDMR) has proven to be an extremely sensitive technique for identifying such defects in semiconductor devices.[2,3] This is possible because EDMR is at least 7 orders of magnitude more sensitive than its parent technique, electron paramagnetic resonance.[4] EDMR is also exclusively sensitive to defects directly involved in device performance. Although EDMR is a powerful tool, its analytical power could be greatly enhanced with the addition of a nuclear magnetic resonance (NMR) component. The conventional double resonance technique, known as electron nuclear double resonance (ENDOR), combines EPR and NMR and has the analytical power to provide detailed atomic scale information about paramagnetic defects in semiconductors as well as in insulators.[5] Unfortunately, the absolute sensitivity of conventional ENDOR is several orders of magnitude lower than that of classical EPR, making the technique essentially impossible in studies of micro- and nanoscale electronic devices. We demonstrate that by utilizing EDMR detection, ENDOR sensitivity may be enhanced by many orders of magnitude, opening possibilities for electrically detected ENDOR (EDENDOR) to contribute substantially to solid-state device physics. Although EDENDOR has been reported in the past,[6,7] to the best of our knowledge, this is the first time ENDOR has been observed within a transistor or, for that matter, any fully operational semiconductor device.

BACKGROUND

In EPR measurements, one observes the response of paramagnetic centers to a large magnetic field in combination with an oscillating magnetic field. The magnetic field provides an energy difference between the two values of the electron spin quantum number. When the frequency of the oscillating magnetic field, ν, times the Planck's constant, h, is equal to this energy difference, electron spins can be "flipped." If an unpaired electron is otherwise unaffected by its surroundings, the resonance condition for that electron is:[4]

$$h\nu = g_e\mu_B B. \tag{1}$$

Here, g_e is the Landé g value (g_e = 2.00232...), μ_B is the Bohr magneton, and B is the magnitude of the applied magnetic field. The analytical power of EPR comes from deviations from Eq. (1). The EPR response of a paramagnetic defect in real material systems is altered by the local environment. There are two primary factors that make the resonance condition system dependent: spin orbit coupling and electron-nuclear hyperfine interactions (other factors play important roles under some circumstances). Spin orbit coupling changes the Landé g_e to an orientation dependent value. Electron-nuclear hyperfine interactions, interactions between the paramagnetic defect site and nearby nuclei with magnetic moments, also affect the resonance condition. Considering both spin orbit coupling and electron-nuclear hyperfine interactions, the resonance condition becomes[4,8]

$$h\nu = g\mu_B B + \sum_i m_i A_i. \tag{2}$$

Here, g is an orientation dependent value usually expressed as a second rank tensor, m_i is the nuclear spin quantum number of the ith nearby magnetic nuclei, and A_i is the electron-nuclear hyperfine coupling due to that nucleus, also usually expressed as a second rank tensor. Measuring the frequency ν and the magnetic field at resonance allows for the identification of the chemical and physical nature of atomic scale defects.

ELECTRICALLY DETECTED MAGNETIC RESONANCE (EDMR)

EDMR is a variation of EPR in which the EPR response is detected as a change in the device current. EDMR is usually detected by one of the two techniques: spin dependent recombination (SDR)[9–11] and spin dependent trap assisted tunneling (SDTAT).[3,12–14] In this work, we detect EDMR via SDR in the base-emitter junction of a 4H-SiC bipolar junction transistor (BJT).[15] A qualitative understanding of the SDR/EDMR response can be provided by the Shockley-Read-Hall model for recombination. An electron in the conduction band is first trapped by a deep level defect. A hole in the valence band is then trapped by the same defect, resulting in electron and hole recombination. (The sequence of electron and hole capture can, of course, be reversed.) This process can be spin dependent. If the conduction electron and a paramagnetic deep level defect electron have the same spin quantum number, the capture event will be forbidden by the Pauli exclusion principle. When the resonance condition for the defect is met, the spin of the defect electron flips and the forbidden transition becomes allowed.

In a conventional ENDOR measurement,[1,16–20] the EPR response is first measured. The magnetic field is then fixed at the field that results in (typically) the maximum microwave absorption, and a radio frequency (RF) is swept while maintaining the EPR microwave oscillating magnetic field. When the RF induces nuclear resonance at a site near the defect observed in EPR, a change in the EPR amplitude is observed. Measuring the response of the EPR amplitude as a function of the NMR RF allows one to measure both the hyperfine interactions and the frequency ν_n at which NMR would be observed for the isolated nucleus. Thus, the ν_n value directly identifies the chemical nature of the nucleus observed. The observation of the hyperfine parameter provides direct information about the relationship between the paramagnetic site electron wave function and the nearby nuclei so observed. This is the easiest to describe for the case of a defect electron spin $(S) = \frac{1}{2}$ and a nearby nuclear spin $(I) = \frac{1}{2}$ for a single value of hyperfine interaction, a. In this case, the ENDOR response condition will be given by $\nu \cong \left|\nu_n \pm \frac{a}{2}\right|$. Somewhat more complex responses can occur for $I > \frac{1}{2}$ due to the presence of nuclear quadrupole moments. The presence of a nuclear quadrupole moment changes the ENDOR response frequency conditions to $\nu \cong \left|\frac{a}{2} \pm \nu_n \pm Q\right|$, where Q depends on the electric field gradient at the nucleus and the nuclear quadrupole moment.

When relatively distant nuclei are involved with relatively small hyperfine interactions and quadrupole contributions, multiple closely spaced ENDOR lines will yield a single response centered on the NMR frequency corresponding to the magnetic field utilized in the measurement. This is the ENDOR response observed within this report and is referred to as "distant ENDOR."

EDENDOR APPARATUS

The EDENDOR spectrometer utilizes a single loop nonresonant "antenna" that is placed vertically within a TE_{102} microwave cavity adjacent to the sample to generate the NMR oscillating magnetic field. The NMR loop is fashioned out of gold on a printed circuit board (PCB), as illustrated in Fig. 1. The sample under test sits beneath this loop on the reverse side of the PCB.

The primary magnetic field, B_0, is supplied by an electromagnet with four-inch pole faces that surrounds the microwave cavity. The EDENDOR frequency sweep is supplied to the NMR coil loop via a Fluke 291 arbitrary waveform generator (AWG) capable of sweeping within the range of near DC to low radio frequencies. In addition, the AWG has a reference signal input that provides the modulation required for the frequency sweep to have

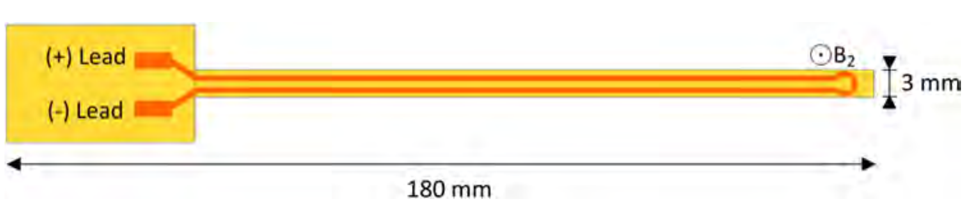

FIG. 1. T-shaped NMR PCB probe design with a 1 mm diameter nonresonant "antenna."

phase-locked modulation. Lock-in detection is utilized to limit the background noise. The device is biased, and the current response is converted to a voltage using a Stanford SR570 low-noise current preamplifier. That voltage is then read by a computer that also controls the output of the AWG. The microwave source generates a standing wave of the microwave frequency within the cavity. A schematic of an EDENDOR spectrometer is illustrated in Fig. 2.

The relationship of the magnetic field to electrical current in the center of a loop is given as

$$B_2 = \frac{\mu_0 I}{2r}, \tag{3}$$

where B_2 is the magnitude of the magnetic field, μ_0 is the permeability of free space, I is the current passing through the loop, and r is the diameter of the loop. The electric field lines generated by current flow through the loop are orthogonal to the direction of the magnetic field.

Potentially debilitating issues with this system are that the power delivered to the NMR coil by the AWG is not perfectly consistent over the swept frequency range. The magnitude of the RF NMR magnetic field is dependent on the AWG's output power which is related to the impedance of the NMR coil. As the frequency is swept, the impedance of the NMR coil will change, thus introducing spurious variations in the device current. These slight changes in the device current can completely obscure the EDENDOR response. Changes in power also change the magnitude of the RF electric field emitted tangent to the loop. There is a possibility that fluctuations in the electric field can cause small unwanted biasing effects. EDENDOR measurements detect changes in the device current. Slight instabilities in the NMR oscillating field amplitude obscure the ENDOR response which is a small resonant inducted change in the device current. The extraneous background is modestly reduced by implementing a high to low impedance buffer circuit to isolate the AWG from the load. The addition of the buffer circuit results in a minor improvement to the EDENDOR signal, but fluctuations in power observed by the load from the AWG still dominate the signal response.

PID CONTROLLER

A proportional-integral-derivative (PID) controller is implemented to provide real-time feedback in a much more effective method to reduce fluctuations in power. The PID controller controls the response of the AWG by comparing the up-to-date output (process variable) to a desired set point, thus generating a real-time error signal.[21] The PID controller's output adjusts in accordance with the magnitude of the error signal, resulting in the error being driven toward zero. The output response of the PID controller is

$$u(t) = K_p e(t) + K_i \int e(t)dt + K_d \frac{de(t)}{dt}, \tag{4}$$

where $u(t)$ is the output, $e(t)$ is the error signal, and K_p, K_i, and K_d are the controller gain parameters corresponding to proportional, integral, and derivative, respectively. The PID gain parameters require careful tuning to achieve the best control.[22] When the controller is properly tuned, the error is driven toward zero extremely quickly; the method behind the PID tuning procedure has been extensively discussed elsewhere.[23–25]

PID POWER LEVELING

For the PID-EDENDOR design, a low-tolerance 50 Ω resistor is placed in series with the NMR coil loop as the load. This is done in order to match the internal 50 Ω source impedance of the AWG to that of the load. For extremely low frequencies, this is a correct assumption as the impedance of the loop is approximately zero. However, the loop will behave as an inductor and the complex impedance increases as the frequency increases in accordance with the following equation:

$$Z = j2\pi f L, \tag{5}$$

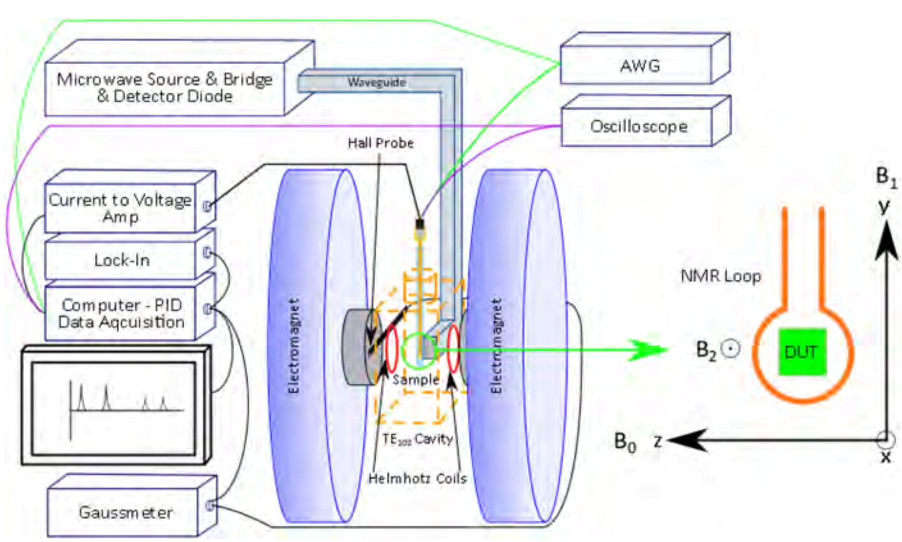

FIG. 2. A schematic of the EDENDOR spectrometer. The magnetic field is held constant, while the AWG supplies the RF sweep, and the device current is recorded.

DISTRIBUTION A: Distribution approved for public release.

where Z is the impedance, j is the imaginary constant, f is the frequency, and L is the inductance of the loop.

In order to observe the response, a 1 GHz oscilloscope with a 10 GS/s sampling rate is placed in parallel to the 50 Ω resistor and the coil loop via a high impedance 10X attenuation cable to ensure that there are no secondary loading effects. The high impedance cable features a compensation capacitor that must be properly calibrated in order to match the input capacitance of the oscilloscope. This ensures that the voltage drop across the oscilloscope's internal impedance is consistent with what is being measured. The circuit diagram of the PID-EDENDOR spectrometer is shown in Fig. 3.

The impedance of the cable and the scope is large in comparison with that of the load (NMR loop circuit); the oscilloscope has little to no effect on the circuit's operation. With that said, the AWG requires a constant 50 Ω load in order for the voltage measured across the load to be correct. Due to the internal 50 Ω source impedance of the AWG, half the voltage will drop over its internal impedance and the other half will drop over the 50 Ω load. The ratio of the voltage over the load to the actual output of the AWG is $\frac{V_L}{V_{AWG}} = \frac{1}{2}$, when the source impedance is matched to that of the load. This is important in high frequency applications as a mismatch in the impedance will cause power to be reflected back to the AWG.[26]

The AWG, 50 Ω resistor, and NMR loop network can be viewed as a simple voltage divider with respect to the voltage across the load. This relationship is shown as follows:

$$V_L = V_{AWG}\frac{R_L + Z_L}{R_s + (R_L + Z_L)} = V_{AWG}\frac{R_L + j2\pi f L}{R_s + (R_L + j2\pi f L)}, \tag{6}$$

where V_L is the voltage observed by the load, V_{AWG} is the voltage output of the AWG, R_L is the 50 Ω load resistor, R_s is the 50 Ω internal impedance of the AWG, and Z_L represents the complex impedance of the loop. However, the inductive component prevents this as larger frequencies cause the magnitude of the inductive impedance term to grow and eventually dominate the following equation:

$$|V_L| = |V_{AWG}|\frac{\sqrt{(R_L)^2 + (2\pi f L)^2}}{\sqrt{(R_s + R_L)^2 + (2\pi f L)^2}}. \tag{7}$$

This will force the $\frac{V_L}{V_{AWG}}$ ratio to approach a value of one, causing the voltage drop across the load to increase with frequency.

In addition to this, the small size of the NMR coil loop as well as the proximity of the PCB traces could lead to the presence of parasitic capacitances. This is especially devastating because this will cause resonant effects and spurious voltage fluctuations at frequencies within the circuit.[27]

In order to remedy this effect, the PID controller was implemented to measure the voltage over the load and compare it to the set voltage, illustrated in Fig. 4. If there are discrepancies between the set and measured voltage throughout the frequency sweep, the error signal will increase and the controller will drive the error toward zero, maintaining the voltage at a desired amplitude. This can be observed by altering Eq. (7), in which the AWG voltage is changed as a function of the error measured by the PID controller, shown in the following equation:

$$|V_L| = |V_{AWG}(e)|\frac{\sqrt{(R_L)^2 + (2\pi f L)^2}}{\sqrt{(R_s + R_L)^2 + (2\pi f L)^2}}. \tag{8}$$

This effect can also be observed by the power absorbed by the load. This relationship is shown as follows:

$$P = \frac{V^2}{Z} = \frac{|V_{AWG}(e)|^2}{\sqrt{(R_L)^2 + (2\pi f L)^2}}. \tag{9}$$

The impedance of the 50 Ω resistor in series with the NMR coil loop has a dependence on the frequency, and the voltage output of

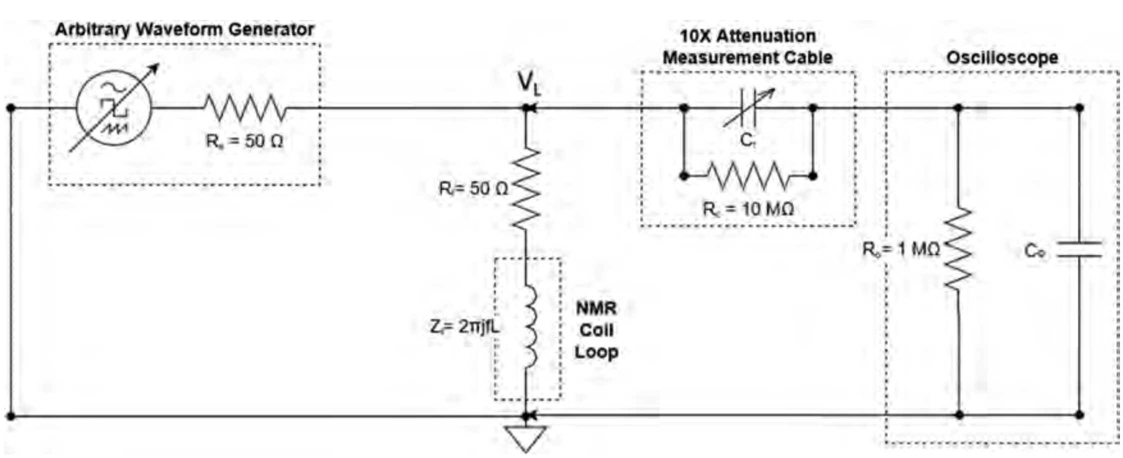

FIG. 3. PID-EDENDOR circuit diagram. R_s represents the internal impedance of the AWG, R_l represents the resistance of the load resistor, Z_l represents the complex impedance of the NMR coil loop, R_c represents the resistance of the 10X attenuation cable, C_t represents the capacitance of the compensation capacitor, and R_o and C_o represent the internal resistance and capacitance of the oscilloscope, respectively.

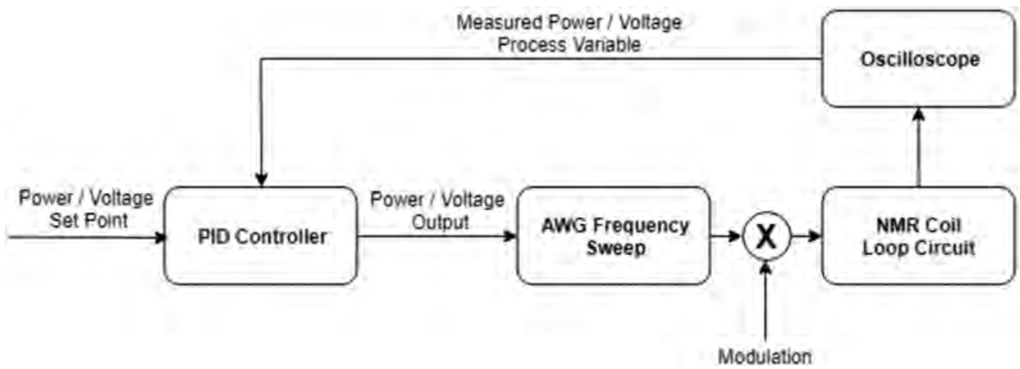

FIG. 4. PID-EDENDOR block diagram. The oscilloscope measures the real time voltage and feeds this value back to the PID controller to generate an error signal. The PID controller then adjusts the AWG output in order to reduce the incoming error to zero.

the AWG depends on the difference between the desired value and the measured value. As the frequency is swept, the power absorbed changes due to the varying impedance of the loop as well as parasitic effects. The PID controller quickly updates the AWG output to eliminate the effect of any measured changes.

RESULTS AND DISCUSSION

In earlier implementations of EDENDOR, in which EDENDOR was observed via spin-dependent photoconductivity in SiO_2/Si structures at room temperature by Hoehne *et al.*,[7] the EDENDOR response was a very small signal riding on a large nonresonant background, a result consistent with measurements made without the implementation of a PID controller. In order to observe the EDENDOR response, the nonresonant background had to be subtracted out. Doing this required twice the amount of time as the measurements had to be performed on and off resonance. The subtraction itself may be less than perfect, further degrading the measurements. In this study, we found that the PID-EDENDOR technique removed the nonresonant background almost completely up to 18 MHz in a 4H-SiC BJT. We observed the EDENDOR response of ^{14}N nuclei interacting with deep level defects involved in recombination events in the depletion region of the base-emitter junction of a 4H-SiC BJT. We know that the response is due to nitrogen nuclei because the NMR frequency of an isolated nitrogen atom at the magnetic field applied, 3366 G, is 1.04 MHz. No other magnetic nuclei present in significant quantities have an NMR response in the vicinity of 1.04 MHz. The EDMR spectrum involved in these EDENDOR measurements has an isotropic $g = 2.003 \pm 0.0003$ and a peak-to-peak linewidth of about 3.4 G. Such EDMR spectra have been linked to silicon vacancies in 4H-SiC metal-oxide-semiconductor field-effect transistors (MOSFETs).[28]

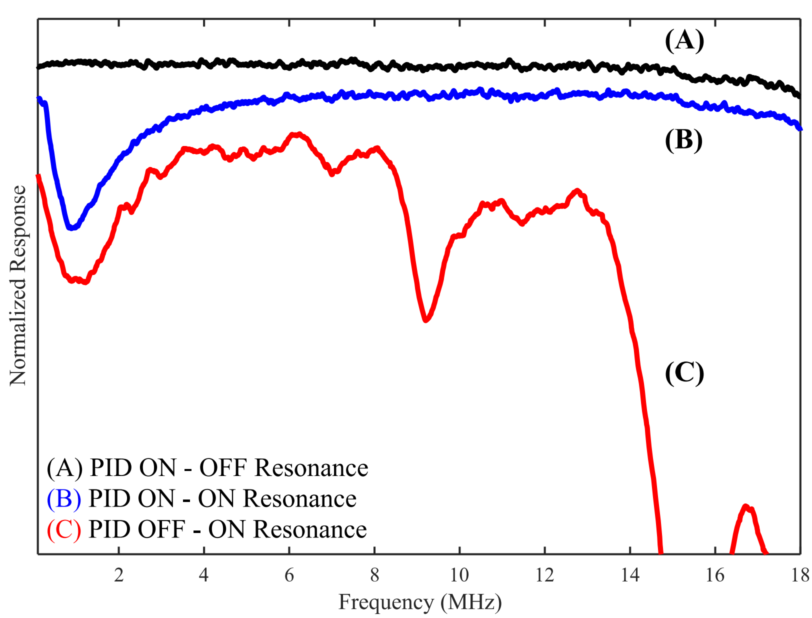

FIG. 5. (a) EDENDOR response with PID controller on–off resonance at a field of 3000 G. (b) EDENDOR response with PID controller on–on resonance at a field of 3366 G. (c) EDENDOR response with PID controller off–on resonance at a field of 3366 G.

This observation is consistent with distant ENDOR as only a single line was observed centered around the NMR frequency corresponding to nitrogen nuclei. The single line indicates that the nitrogen nuclei are sufficiently far from the paramagnetic sites. For this device the nitrogen serves as substitutional donors which reside at high symmetry carbon sites. Characterization and fabrication details about the device have been described elsewhere.[29] The response was observed before and after the PID controller was utilized. When the PID controller was off, the EDENDOR response was dominated by nonresonant effects that were larger than the signal in question; some effects even resembled the resonant peaks. Figure 5 shows the EDENDOR response with the results for the PID controller on and off normalized to the observed ^{14}N peak that is centered near 1.04 MHz; the EDENDOR response at a field far off resonance is also included for reference.

CONCLUSIONS

The PID controller's ability to maintain constant power through the loop is dependent on real-time changes in power. The voltage is directly measured and fed back to the PID controller from the oscilloscope, so power changes due to various reasons are corrected with sufficient accuracy. To assure that the PID controller is functioning to the best of its ability, it is important to sweep frequencies at a reasonable rate. This is because the PID controller responds quickly but not instantaneously. The more time the PID controller has to correct power fluctuations, the more efficiently it will perform. The PID controlled power leveling technique has demonstrated the ability to resolve EDENDOR signals when the response would normally be dominated by fluctuations in power. This technique has applications anywhere when a constant power frequency sweep is required. The PID controller's performance also depends on the precision of the oscilloscope's measurements, the precision of the AWG's output, and the speed at which both these instruments communicate with a computer. The more precise the measurement and output, the better the PID controller is able to detect and correct small changes. This work shows that it is possible to make extremely high sensitivity EDENDOR measurements in a fully functional transistor. Our work thus indicates that EDENDOR will be widely applicable to technologically relevant solid-state devices. Such measurements should be particularly useful in studies of device physics as they provide a direct link between the chemical and physical nature of defects and device performance.

ACKNOWLEDGMENTS

This work was supported by the Air Force Office of Scientific Research under Award No. FA9550-17-1-0242.

REFERENCES

1. G. R. Eaton, S. S. Eaton, D. P. Barr, and R. T. Weber, *Quantitative EPR* (Springer, Wien, New York, 2010).
2. C. J. Cochrane, P. M. Lenahan, and A. J. Lelis, J. Appl. Phys. **105**, 064502 (2009).
3. M. J. Mutch, P. M. Lenahan, and S. W. King, J. Appl. Phys. **119**, 094102 (2016).
4. J. A. Weil, J. R. Bolton, J. E. Wertz, and H. A. Buckmaster, *Electron Paramagnetic Resonance: Elementary Theory and Practical Applications* (John Wiley & Sons, Inc., New York, 1994).
5. L. Kevan and L. Kispert, *Electron Spin Double Resonance Spectroscopy* (John Wiley & Sons, Inc., New York, 1994).
6. B. Stich, S. Greulich-Weber, and J. M. Spaeth, Appl. Phys. Lett. **68**, 1102 (1996).
7. F. Hoehne, L. Dreher, H. Huebl, M. Stutzmann, and M. S. Brandt, Phys. Rev. Lett. **106**, 187601 (2011).
8. W. Gordy, *Theory and Applications of Electron Spin Resonance* (John Wiley & Sons, Inc., New York, 1980).
9. D. Kaplan, I. Solomon, and N. F. Mott, J. Phys., Lett. **39**, L51 (1978).
10. D. J. Lepine, Phys. Rev. B **6**, 436 (1972).
11. D. J. McCrory, M. A. Anders, J. T. Ryan, P. R. Shrestha, K. P. Cheung, P. M. Lenahan, and J. P. Campbell, IEEE Trans. Device Mater. Reliab. **18**, 139 (2018).
12. R. J. Waskiewicz, M. J. Mutch, P. M. Lenahan, and S. W. King, in *2016 IEEE International Integrated Reliability Workshop* (IEEE, 2016), p. 99.
13. M. J. Mutch, P. M. Lenahan, and S. W. King, J. Appl. Phys. **109**, 062403 (2016).
14. M. J. Mutch, T. Pomorski, B. C. Bittel, C. J. Cochrane, P. M. Lenahan, X. Liu, R. J. Nemanich, J. Brockman, M. French, M. Kuhn, B. French, and S. W. King, Microelectron. Reliab. **63**, 201 (2016).
15. C. J. Cochrane, P. M. Lenahan, and A. J. Lelis, Appl. Phys. Lett. **90**, 123501 (2007).
16. W. L. Warren and P. M. Lenahan, Phys. Rev. B **42**, 1773 (1990).
17. G. Feher, Phys. Rev. **114**, 1219 (1959).
18. J. D. Watkins and J. W. Corbett, Phys. Rev. **134**, A1359 (1964).
19. B. M. Hoffman, J. Martinsen, and R. A. Venters, J. Magn. Reson. **59**, 110 (1984).
20. B. M. Hoffman, R. A. Venters, and J. Martinsen, J. Magn. Reson. **62**, 537 (1985).
21. M. Rata, G. Rata, and V. Chatziathanasiou, in EPE 2014 International Conference and Exposition on Electrical and Power Engineering, 2014.
22. J. M. Dilhac, C. Ganibal, J. Bordeneuve, and N. Nolhier, IEEE Trans. Electron Devices **39**, 201 (1992).
23. S. Li and Q. Jiang, in *2011 IEEE 3rd International Conference on Communication Software and Networks* (IEEE, 2011), p. 408.
24. H. Wu, W. Su, and Z. Liu, in *2014 9th IEEE Conference on Industrial Electronics and Applications* (IEEE, 2014).
25. A. G. Daful, in 2018 Advances in Science and Engineering Technology International Conferences (ASET), 2018.
26. M. Bai and H. Liang, in 2010 International Forum on Information Technology and Applications (IEEE, 2010), p. 350.
27. T. Yu, X. Wang, R. Ni, and J. Liu, in 2010 Asia-Pacific Power and Energy Engineering Conference, 2010.
28. C. J. Cochrane, P. M. Lenahan, and A. J. Lelis, Appl. Phys. Lett. **100**, 023509 (2012).
29. Q. Zhang, C. Jonas, A. Burk, C. Capell, J. Young, R. Callanan, A. Agarwal, J. Palmour, B. Geil, and C. Scozzie, Mater. Sci. Forum **600-603**, 1159 (2009).

JOURNAL OF APPLIED PHYSICS **124**, 184501 (2018)

Effects of nitrogen on the interface density of states distribution in 4H-SiC metal oxide semiconductor field effect transistors: Super-hyperfine interactions and near interface silicon vacancy energy levels

Mark A. Anders,[1] Patrick M. Lenahan,[2] Arthur H. Edwards,[3] Peter A. Schultz,[4] and Renee M. Van Ginhoven[5]

[1]*National Institute of Standards and Technology (NIST), 100 Bureau Drive, Gaithersburg, Maryland 20899, USA*
[2]*Department of Engineering Science and Mechanics, Pennsylvania State University, 212 EES Bldg., University Park, Pennsylvania 16802, USA*
[3]*Space Vehicles Directorate, Air Force Research Laboratory, Kirtland Air Force Base, New Mexico 87117-5776, USA*
[4]*Sandia National Laboratories, Albuquerque, New Mexico 87185-1322, USA*
[5]*Directed Energy Directorate, Air Force Research Laboratory, Kirtland Air Force Base, New Mexico 87117-5776, USA*

(Received 22 June 2018; accepted 20 October 2018; published online 13 November 2018)

The performance of silicon carbide (SiC)-based metal-oxide-semiconductor field-effect transistors (MOSFETs) is greatly enhanced by a post-oxidation anneal in NO. These anneals greatly improve effective channel mobilities and substantially decrease interface trap densities. In this work, we investigate the effect of NO anneals on the interface density of states through density functional theory (DFT) calculations and electrically detected magnetic resonance (EDMR) measurements. EDMR measurements on 4H-silicon carbide (4H-SiC) MOSFETs indicate that NO annealing substantially reduces the density of near interface SiC silicon vacancy centers: it results in a 30-fold reduction in the EDMR amplitude. The anneal also alters post-NO anneal resonance line shapes significantly. EDMR measurements exclusively sensitive to interface traps with near midgap energy levels have line shapes relatively unaffected by NO anneals, whereas the measurements sensitive to defects with energy levels more broadly distributed in the 4H-SiC bandgap are significantly altered by the anneals. Using DFT, we show that the observed change in EDMR linewidth and the correlation with energy levels can be explained by nitrogen atoms introduced by the NO annealing substituting into nearby carbon sites of silicon vacancy defects. *Published by AIP Publishing.*
https://doi.org/10.1063/1.5045668

INTRODUCTION

Metal-oxide-semiconductor field-effect transistors (MOSFETs) based on silicon dioxide (SiO_2) on 4H-silicon carbide (4H-SiC) show great promise in high power and high temperature applications. However, the potential of this technology is limited by less than ideal electronic behavior at the SiC/SiO_2 interface region. Incorporation of post-oxidation NO annealing into the process flow results in significant densities of nitrogen in the interfacial region (about $10^{14}\,cm^{-2}$)[1,2] along with substantial improvement of the interface properties—typically an order of magnitude improvement in effective channel mobility[3] via a comparable decrease in interface trap density[4–6] and nitrogen counter doping.[7] Although the NO anneals are of great technological importance in SiC MOSFET technology, the materials physics involved in the annealing process is not well understood. Important physical insight can be gathered from electron paramagnetic resonance (EPR) measurements[8] obtained via electrically detected magnetic resonance (EDMR).[9,10]

Earlier EDMR studies[11] show that NO anneals result in substantial reduction of the magnetic resonance spectrum associated with silicon vacancy (V_{Si}) centers located near the SiC/SiO_2 interface, as indicated in Fig. 1. (The EDMR results also show a large reduction of a second spectrum consisting of two lines with a separation of approximately 11 G. This spectrum is attributed to a hydrogen complexed oxygen deficient silicon site called the 10.4 doublet center.[12] This aspect of the EDMR will not be further discussed in this work.) The EDMR response corresponds to the singly negatively charged V_{Si} site $-/0$ energy level. Recent EDMR measurements utilizing the bipolar amplification (BAE) technique[13] and spin dependent charge pumping (SDCP)[14] indicate that nitrogen nearby to these V_{Si} centers broaden their EDMR spectrum and that the broadening depends on the measurement used.[15] We utilize these EDMR measurements and density functional theory (DFT) to explore the effect of nitrogen on V_{Si}. We consider nitrogen atoms substituted in third-nearest neighbor carbon sites (N_C) to paramagnetic V_{Si} and compare our findings with results from the EDMR measurements. [The silicon vacancy is surrounded by four carbon nearest neighbors, 12 silicon second-nearest neighbors (in two distinct shells), and 25 carbon third-nearest neighbors (in six distinct shells)]. Candidate nitrogen sites are shown in Fig. 2.

To provide a coherent discussion of our analysis, we first give a brief discussion of EPR and EDMR in general, and

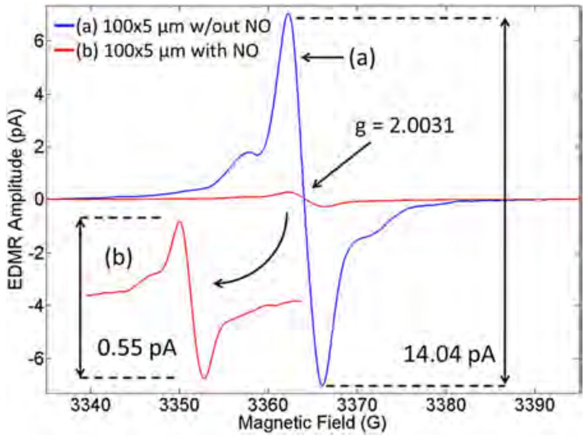

FIG. 1. The effects of an NO anneal on the SDCP detected EDMR. Two defect spectra are superimposed: a sharp center line, due to silicon vacancies in the near interface silicon carbide and a weaker spectrum, with two lines separated by about 11 G due to hydrogen complexed E′ centers. The NO anneal greatly reduces the amplitudes of both defect spectra.[11]

then we describe the BAE and SDCP EDMR detection techniques. EPR occurs when a paramagnetic center in a magnetic field absorbs electromagnetic radiation at a frequency ν. In the simplest case of an unpaired electron unperturbed by its environment, the electron transitions from its ½ to −½ spin state (or vice versa) with a resonance condition given by[8]

$$h\nu = g_e \mu_B B. \tag{1}$$

Here, h is Planck's constant, ν is the electromagnetic radiation frequency, g_e is the free electron g factor ($g_e = 2.0023193\ldots$), μ_B is the Bohr magneton, and B is an externally applied magnetic field.

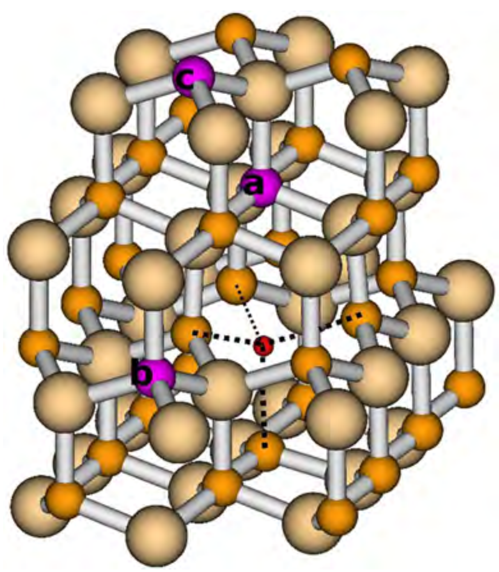

FIG. 2. Sites for nitrogen decoration (purple) in silicon carbide supercell. Brown (tan) are carbon (silicon) atoms. Center of vacancy is indicated by red atom. In all other figures and tables, N_C-V_{Si} complex with nitrogen at the a, b, or c site will be referred to as N-a, N-b, and N-c, respectively.

The analytical power of EPR (and EDMR) comes from deviations from this simple case caused by the paramagnetic site environment. For the observations in this study, two phenomena dominate these deviations: spin-orbit coupling and electron-nuclear hyperfine interactions. For the purpose of our discussion, the spin Hamiltonian of such a system can be expressed as[8]

$$\mathcal{H} = \mu_B \boldsymbol{B} \cdot \boldsymbol{g} \cdot S + \sum_i I_i \cdot \boldsymbol{A_i} \cdot S. \tag{2}$$

Here, μ_B is the Bohr magneton, $\boldsymbol{B}$ is the applied magnetic field vector, S is the electronic spin operator, and I_i is the nuclear spin operator for the ith nucleus. $\boldsymbol{g}$ and $\boldsymbol{A_i}$ are essentially tensors which describe a defect's local environment and are usually referred to as the g and A tensors. Spin-orbit coupling causes the g tensor components to deviate from the free electron g_e, and A provides a measure of electron-nuclear hyperfine interactions. It should be noted that a more complex spin Hamiltonian is required to fully describe the silicon vacancies discussed herein. However, the simple form of Eq. (2) is adequate to understand the results presented in this work.

EDMR measurements detect EPR through a change in device current. EDMR is inherently advantageous for solid state electronic device studies for two reasons: (1) it is exclusively sensitive to defects involved in electronic transport and (2) it is typically at least 10×10^6 times more sensitive than conventional EPR. In an EDMR measurement of an electronic device, the device is placed into a high quality factor microwave cavity or an RF coil which is placed in an electromagnet. As is the case for conventional EPR, the device is exposed to constant frequency electromagnetic radiation. Unlike conventional EPR, in EDMR, the device under study is biased in such a way as to produce a recombination or trap assisted tunneling dominated current. The magnetic field is slowly and linearly swept about the resonance field, and the EPR-induced current change is measured as a function of the magnetic field. The EDMR measurements discussed in this paper are, as mentioned previously, BAE and SDCP.

The BAE approach relies on spin dependent recombination (SDR)[10] to detect EDMR. SDR occurs when a charge carrier in either the valence or conduction band transitions to a deep level defect and then recombines through the subsequent capture of a charge carrier of the opposite sign. This process is spin dependent. A somewhat simplified explanation, suitable for the discussion herein, is as follows. The process is spin dependent because the capture event involving a paramagnetic charge carrier (electron or hole) at a paramagnetic defect site can only take place when the two entities have opposite spins. Envision the simple case of a conduction electron encountering a neutral paramagnetic "dangling bond" site. If the conduction electron and dangling bond electron have the same spin quantum number, the capture event would be forbidden by the Pauli exclusion principle. However, if the dangling bond spin were to be "flipped" by an EPR event, the trapping process and eventual recombination would be allowed. Inducing EPR of defect sites thus increases the recombination rate and recombination current.

In the BAE measurement, the MOSFET source-body diode is forward biased. The gate is biased so as to attract the charge carriers injected by the source; however, the bias is not sufficient to create an inversion layer. Current is measured at the drain (the drain is at virtual ground) and is strongly influenced by the interface/near interface recombination events. The BAE response is optimized by selecting a gate voltage that maximizes the change in interface/near interface recombination current. This change in recombination current as a function of magnetic field is the BAE signal. Because the BAE technique uses SDR, it is only sensitive to deep levels, as they must be efficient recombination centers.

SDCP measurements utilize EPR to observe a change in the current produced by charge pumping (CP).[16–18] SDCP, like BAE, exploits the spin dependent nature of charge capture at the MOSFET interface. Unlike BAE, however, SDCP can be sensitive to defect levels throughout a large majority of the 4H-SiC bandgap. SDCP utilizes CP, a powerful and widely utilized electrical MOSFET interface trap characterization technique. The CP process, in the most straightforward approach, involves the application of a continuous trapezoidal waveform to the MOSFET gate to alternately invert and accumulate the interface, filling and emptying traps at the interface region. The process produces a recombination current dominated by interface traps called the CP current which is measured at the body contact. Thus, the SDCP response (ΔI_{CP}) is the EPR-induced change in the CP current. For our discussion, the most relevant aspect of the technique is its ability to directly connect EDMR spectra with a range of energy levels within the 4H-SiC bandgap. The CP current is proportional to the waveform frequency, charge, effective channel area, density of states, and the measured bandgap energy window (ΔE_{CP}). ΔE_{CP} is nearly centered around midgap and can be approximated by[16–18]

$$\Delta E_{CP} = 2k_B T \ln\left(\frac{\Delta V_G}{\overline{v_{th}}\;\;\overline{\sigma}\, n_i\;\;(V_{TH}^{CP} - V_{FB}^{CP})\;\;\sqrt{t_r t_f}}\right), \quad (3)$$

where k_B is Boltzmann's constant, T is the temperature, ΔV_G is the gate waveform pulse amplitude, $\overline{v_{th}}$ is the geometric average of the electron and hole thermal velocity, $\overline{\sigma}$ is the geometric average of the electron and hole capture cross sections, n_i is the intrinsic carrier concentration, V_{TH}^{CP} and V_{FB}^{CP} are the CP threshold and flatband voltages, respectively, and t_r and t_f are the rise and fall times of the gate waveform, respectively. Equation (3) directly links measured defects to the range of energy levels at which they reside, thus providing a direct link between defect structure and an energy window.

EXPERIMENTAL

Electrically detected magnetic resonance

Our measurements were made on a homemade EDMR spectrometer operating at an ultra-low frequency ($\nu = 360$ MHz). It consists of a custom-made electromagnet made of 5 nested pairs of Helmholtz coils, a Kepco BOP 100-4M power supply, a Lake Shore Cryotronics 450 DSP temperature-compensated Gauss meter and Hall probe, a Stanford Research Instruments SG382 microwave generator, and a computer which provides lock-in detection, magnetic field control, and the data acquisition system. The RF magnetic field is provided by a Doty Scientific surface coil and resonance circuit. The RLC circuits maximize the RF fields at 360 MHz. Because the spectrometer utilizes lock-in detection, a small audio frequency alternating magnetic field is added to the large swept magnetic field to modulate resonance. As a consequence of this detection method, the measured spectrum is approximately the derivative of the EDMR response. For SDCP measurements, the gate waveform was applied with a Tabor Electronics WW2572A waveform generator. All measurements were made at room temperature.

Two types of MOSFETs were utilized in this study. Both types have a wet thermal gate oxide process but were fabricated by different manufacturers. One type received a post-oxidation anneal in NO for 2 h at 1175 °C while the other did not. The NO annealed and as-grown MOSFETs had a doping density, mobility, and defect density of $7 \times 10^{16}\,\mathrm{cm}^{-3}$, $19\,\mathrm{cm}^2/\mathrm{V\,s}$, $4.6 \times 10^{11}\,\mathrm{cm}^{-2}\,\mathrm{eV}^{-1}$ and $6 \times 10^{16}\,\mathrm{cm}^{-3}$, $1\,\mathrm{cm}^2/\mathrm{V\,s}$, $3.1 \times 10^{12}\,\mathrm{cm}^{-2}\,\mathrm{eV}^{-1}$, respectively. BAE measurements utilized longer channel MOSFETs which had gate areas (L × W) of $5 \times 100\,\mu\mathrm{m}^2$ (as-grown) and $100 \times 100\,\mu\mathrm{m}^2$ (NO anneal), and SDCP utilized shorter channel MOSFETs which had gate areas (L × W) of $1 \times 424\,\mu\mathrm{m}^2$ (as-grown) and $1 \times 1000\,\mu\mathrm{m}^2$ (NO anneal).

Theory

The defect calculations were executed with the highly efficient SeqQuest DFT code, using well converged, local orbital bases (double-zeta + polarization) and Hamann-type pseudopotentials,[19] with a spin-polarized Perdew-Becke-Ernzerhoff (PBE) implementation of the generalized gradient approximation.[20] To incorporate self-consistently the correct asymptotic boundary conditions for isolated charged defects, we use the local moment counter charge (LMCC) method[21,22] instead of a *jellium* background charge. This technique has predicted defect level energies with 0.1-0.2 eV accuracy across a full bandgap in silicon,[23,24] gallium arsenide,[25,26] and cesium iodide.[27] The long-range dielectric screening energy (outside the DFT defect simulation cell) is incorporated using a Jost expression[28] for a charge Q in the spherical cavity in isotropic dielectric medium with a low frequency dielectric constant, ε_o,

$$E_{pol} = -\frac{Q^2}{2R_{Jost}}\left[1 - \frac{1}{\varepsilon_o}\right], \quad (4)$$

where R_{Jost} is an effective "spherical radius" of the supercell (Rydberg atomic units). Good convergence to an asymptotic limit as a function of supercell size verifies that this is a good approximation.[25]

We use 2H-SiC as a proxy for 4H. It offers more convenient supercell dimensions, 2H- and 4H-SiC have bandgaps that are within 0.1 eV of each other, and, as noted in Ref. 29, and seen in Fig. 3, the defect levels are very similar. We use a 300-atom supercell (a 5 × 5 × 3 expansion of the

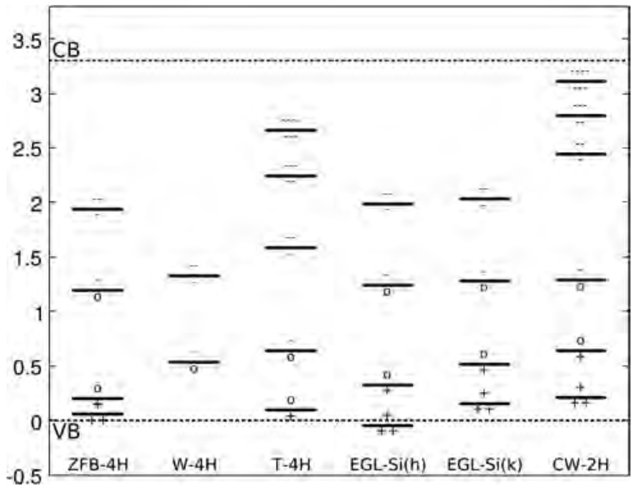

FIG. 3. Silicon vacancy defect levels from several calculations for 2H- and 4H-SiC. The band edges, estimated from the LMCC method, are shown in dotted lines. ZFB, W, T, EGL, and CW are from Refs. 29–32 and current work. For EGL, Si(h) and Si(k) indicate the two inequivalent sites.

conventional 4-atom hexagonal unit cell) with a $2\times2\times2$ k-sampling. Using our PBE lattice parameters, c = 5.09 Å and a = 3.10 Å, this $5\times5\times3$ supercell has a c/a ratio of 0.985, convenient for applying the spherical Jost screening estimate. The simulation volume was fixed to the theoretical lattice parameters, and atomic positions were relaxed to a minimum energy defect structure, with forces less than 0.02 eV/Å on each atom. Atoms at the C-axis cell boundary plane midway between Si vacancies in neighboring supercells were held fixed to prevent artificial strain interactions between defects. We considered nitrogen substituted on the nearby carbon sites "a," "b," and "c" depicted in Fig. 2: $N_C - V_{Si}$ pair defects are denoted as N-a, N-b, and N-c. We also considered two cases where nitrogen replaced second nearest neighbor silicon. These were found to be significantly higher in energy (~7 eV) and therefore not considered further in this work. We considered low- and high-spin configurations. In all cases, the high-spin state was lower in energy by roughly 0.2-0.3 eV.

DISCUSSION

Electrically detected magnetic resonance results

As mentioned previously, BAE and SDCP offer complementary information about the energy levels of the observed defects.[15] The BAE approach is specifically sensitive to defects with energy levels near midgap while the SDCP measurements (for our case) are sensitive to defect levels throughout ~85% of the bandgap.[15] The line shape of the (dramatically reduced) NO-annealed device EDMR spectrum depends on the EDMR detection technique. This difference is clear in both high and ultra-low resonant frequency EDMR measurements. However, the differences are most evident in the ultra-low frequency spectra, and we can assume that changes to spectra (in our case, spectral broadening) are almost entirely due to hyperfine interactions[8] which simplifies our discussion. Representative results are illustrated in

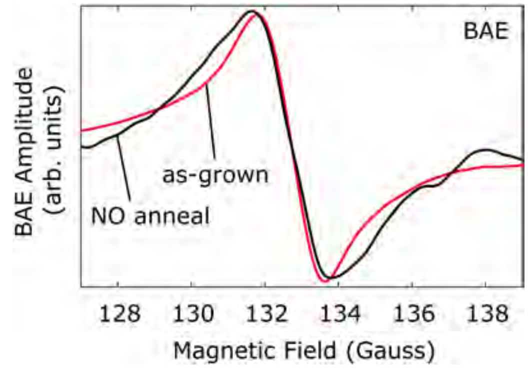

FIG. 4. 360 MHz BAE spectra comparing NO annealed (black) and as-grown (red) samples. Spectra are amplitude normalized for better comparison of linewidths.

Figs. 4 and 5 which compare measurements of NO annealed and as-grown MOSFETs via both EDMR techniques.

If the EDMR is detected via BAE, the as-grown device spectrum is virtually identical to the NO-annealed device spectrum (Fig. 4), but if the EDMR is detected via SDCP, the NO-annealed device spectrum is broader than the as-grown device spectrum by about 1.5 G (Fig. 5). This broadening is almost certainly due to hyperfine interactions with nearby nitrogen introduced by the NO anneal, because the spectral linewidths are virtually identical between BAE and SDCP in the as-grown device. In contrast, the SDCP spectrum is much broader for the NO-annealed device. The spectral broadening and the change in energy levels are apparently linked. The BAE spectra (due to only those defects with −/0 energy levels near midgap) are essentially un-broadened by the NO anneals whereas the SDCP spectra (due to defects with −/0 levels more broadly distributed through the gap) are significantly broader. How can this be? Our results make sense if a majority of V_{Si} are coupled to nearby nitrogen, the nearby nitrogen shifts the −/0 V_{Si} energy levels away from midgap. DFT provides insight into this theory.

Theoretical results

As mentioned previously, we consider nitrogen atoms introduced as third-nearest neighbors (nitrogen substituted for

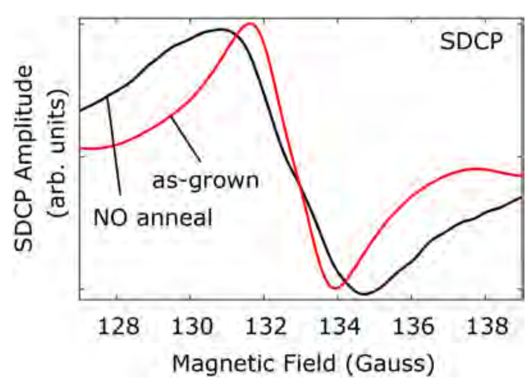

FIG. 5. 360 MHz SDCP spectra comparing NO annealed (black) and as-grown (red) samples.

TABLE I. Energies of formation and intra-defect distances for sites labeled in Fig. 4.

	$R_{N-V_{Si}}$ (Å)	ΔE_f (eV) (Si-rich)
V_{Si}	…	2.75
N-a	3.36	4.94
N-b	4.78	4.96
N-c	5.87	5.11

carbon) to paramagnetic V_{Si}. In Table I, we show the energies of formation (ΔE_f) in the neutral charge state (in a Si-rich limit), and the intradefect distance, the distance between the defect center and the average position of the nitrogen nuclei ($R_{N-V_{Si}}$), for the various $N_C - V_{Si}$ configurations. The stability of nitrogen at carbon sites changes remarkably little with distance from the vacancy. Assuming equilibrium conditions, there would be half as many N_C substitutions at 4.78 Å, and 0.003 as many at 5.87 Å, as there are at 3.36 Å.

In Fig. 6, we show computed defect levels for isolated V_{Si} and for the nitrogen substituting for carbon atoms near a V_{Si}. We label the levels for the N_C sites with the analogous charge state of the isolated V_{Si}. We expect that the N_C will donate one of its electrons to the V_{Si} so that the neutral $V_{Si} + N_C$ defect complex corresponds to -1 charge-state of the vacancy and a positive nitrogen ion. This simple picture is supported by the preservation of the general features of the V_{Si} level diagram, with shifts downward, consistent with the N_C acting as a modest perturbation on the V_{Si}. The further the nitrogen ion is from the V_{Si}, the smaller the shift. The $-/0$ level corresponds to the level observed in the EDMR. The largest shift of this level, for the nearest nitrogen, N-a, is ~0.5 eV. Note that Fig. 6 has no reference to the band edges. In Fig. 3, we compare our defect levels for the V_{Si} from several calculations in the literature.[29–32] Note that the results from Zywietz et al.,[30] from Ettisserry et al.,[32] and from the current work all put the $-/0$ level near midgap. Reference 29 did not account for finite cell effects. The results from Ref. 32 are for hybrid screened exchange and include both finite cell corrections and an approximate treatment of the proximity to the interface. Note that, for the $-/0$ level, there is an insignificant difference between Si(h) and Si(k), the two inequivalent silicon sites in 4H-SiC. While we do not include interface effects, for defects 3 Å from the interface, the interface electrostatic adjustment is only 0.05 eV for the -1 charge state.[32,33] Finally, we should note that the shifts in Fig. 6 are independent of interface effects. Finally, the band edges in Fig. 3 imply that for all nitrogen decorated vacancies considered, the +/++ level will be subsumed into the valence band.

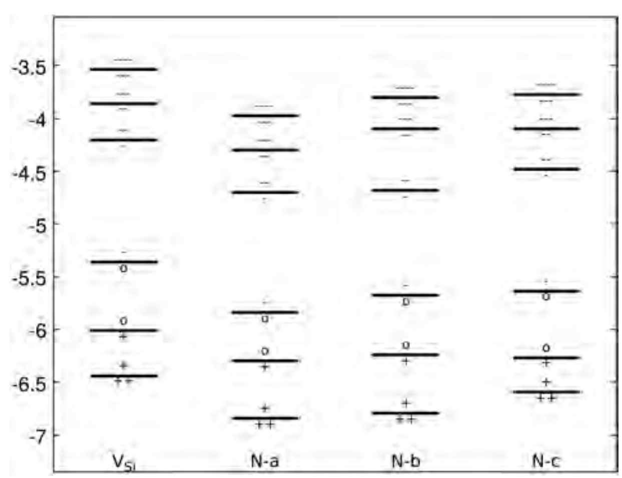

FIG. 6. Defect levels, as calculated using the LMCC, for the silicon vacancy and for the three configurations of N_C-V_{Si} defect pairs labeled N-a, N-b, and N-c in Fig. 2.

The downward shift in the near midgap $-/0$ level in the current calculation would explain the experimental EDMR observations. When nitrogen introduced by the NO anneal decorates V_{Si}, those V_{Si} would not be probed by the BAE measurements. (V_{Si} without nitrogen will still be probed.) The $N_C - V_{Si}$ complex would, however, be probed by the SDCP measurements, and they would be broadened by the nitrogen. This is exactly the case. The Wang result[31] and Torpo result[29] would lead to little change, the spin-active state is already completely within the range of the SDCP experiment and yielding no difference between the BAE and SDCP after the NO anneal.

Finally, we turn to the calculated spin densities on the nitrogen ions. We used Mulliken population analysis[34] generalized for solids. Following Mulliken, in Eq. (5), we define a set of gross spin populations

$$\rho_{n_A}^{\alpha,\beta} = \sum_k \sum_{i=1}^{n_{orb}^{\alpha,\beta}} n_{occ}^{i,\alpha,\beta} \sum_{m_B} C_{k,i,n_A}^{\alpha,\beta *} S_{n_A,m_B}^k C_{k,i,m_B}^{\alpha,\beta}, \tag{5a}$$

$$\rho_A^{\alpha,\beta} = \sum_{n_A} \rho_{n_A}^{\alpha,\beta}, \tag{5b}$$

$$\rho_{n_A}^S = \rho_{n_A}^\alpha - \rho_{n_A}^\beta, \tag{5c}$$

$$\rho_A^S = \rho_A^\alpha - \rho_A^\beta, \tag{5d}$$

where k is summed over the k-vector sample, i is summed over spin-up (α) or spin-down (β) eigenstates, n_A and m_B label the Bloch function associated with the local orbital basis element n_A and m_B, centered on atoms A and B, respectively, C is the complex linear combination coefficients for the Bloch functions in the eigenvectors, $n_{occ}^{i,\alpha,\beta}$ is the occupation number of the ith α or β eigenfunction, determined by Fermi-Dirac statistics, and S is the k-dependent overlap matrix between Bloch functions.

In Table II, we show the total spin densities on N-a, N-b, and N-c. These are sums of terms shown in Eq. (5c)—essentially the angular momentum projections of the atomic Mulliken spin populations. Qualitatively, they measure the overlap of the defect wave function in the -1 charge state with the nitrogen atom that decorates the vacancy. Because the wave function is localized on the core of the vacancy, it is unsurprising that the nitrogen-spin density decreases monotonically with distance. We should note that these are pseudo-spin densities obtained from the pseudo-wave functions. They do not include core-polarization, and they do not

TABLE II. Spin densities, in electron spins, on the three sites shown in Fig. 4.

	s-density	p-density	d-density
N-a	1.73×10^{-3}	2.46×10^{-2}	3.2×10^{-4}
N-b	7.0×10^{-4}	1.13×10^{-2}	6.4×10^{-4}
N-c	7.0×10^{-4}	1.12×10^{-2}	6.1×10^{-4}

have the correct orthogonality oscillations that would permit direct calculation of hyperfine parameters. However, these sums over direction and a split-valence basis set are good first order approximations (to better than a factor of two) for estimates of broadening due to the hyperfine interactions with the nearby nitrogen atoms. Hyperfine constants for electrons 100% localized on the near 100% abundant ^{14}N sites[35,36] allow for approximate calculation of the broadening. The isotropic hyperfine coupling constant for an electron 100% localized on a nitrogen s-orbital would be 646.2 G. The anisotropic hyperfine coupling constant for an electron 100% localized on a nitrogen p-orbital would be 19.8 G. Since the nitrogen nucleus has a spin of one and the s-contribution is somewhat larger than the p-contribution, we estimate that the broadening would be dominated by the s-character contribution and would correspond to about 2.2 G for nitrogen atoms at the N-a sites and 0.9 G for nitrogen atoms at the N-b and N-c sites. The net effect would be a weighted average of these values. Thus, the experimentally observed broadening between as-grown and NO-annealed SDCP spectra of about 1.5 G is in good agreement with the, admittedly, semi-quantitative theoretical values. This broadening would, of course, only be observable if these nitrogen atoms were to be present at a very high fraction of the defect sites. Our results then are entirely consistent with the earlier work of others indicating a very high density of nitrogen induced in the near interface region by the NO annealing. However, since our resonance results are only sensitive to the immediate surroundings of the defects, they do not directly address the overall nitrogen concentration in the near interface region, but only the nitrogen concentration in the immediate vicinity of these defects.

SUMMARY

Our results provide a coherent explanation for the differences in the BAE and SDCP EDMR results for devices which have and have not been subjected to the technologically important NO anneals. Nitrogen atoms in close proximity to the silicon vacancy centers will both lower the −/0 energy levels and broaden the EDMR spectra. Our work is also consistent with the earlier work of others indicating the presence of extremely high densities of nitrogen atoms at the SiC-oxide interface as a result of NO anneals.[1,2] We note that the defects measured by BAE and SDCP are close to the interface; however, due to the complicated nature of the experiments, we can only make an order-of-magnitude estimate for their location. The limiting dimension in the SDCP measurement is likely the width of the inversion layer because the traps must be filled by the inversion electrons supplied by the source and the drain. This width is well understood[37] and corresponds to several nanometers in these measurements. Thus, a reasonable order-of-magnitude estimate for the defect distance is within several nm of the interface. It should also be noted that our results also suggest that the NO anneals would be more effective in improving the performance of n-channel devices than p-channel devices as the introduction of the nitrogen atoms will drive remaining defect energy levels downward toward the interface SiC valence band edge.

ACKNOWLEDGMENTS

AFRL gratefully acknowledges the support of the Air Force Office of Scientific Research (AFOSR) through Contract No. FA9550-17RVCOR505. This work was supported in part by a grant of computer time from the DoD High Performance Computing Modernization Program at the Air Force Research Laboratory and from the U.S. Army Engineer Research and Development Center. Work at Penn State was supported in part by AFOSR under Grant No. FA 9550-17-1-0242 and in part by the U.S. Army Research Laboratory, Adelphi, MD. Sandia National Laboratories is a multi-mission laboratory managed and operated by National Technology and Engineering Solutions of Sandia, LLC, a wholly owned subsidiary of Honeywell International, Inc., for the U.S. Department of Energy's National Nuclear Security Administration under Contract No. DE-NA0003525. This paper describes objective technical results and analysis. Any subjective views or opinions that might be expressed in the paper do not necessarily represent the views of the U.S. Department of Energy, U.S. Department of Commerce, or the United States Government. A.H.E. thanks Dr. Andrew C. Pineda and Dr. Danhong Huang for helpful questions and discussions. M.A.A. and P.M.L. thank Dr. Aivars J. Lelis of the U.S. Army Research Laboratory, Adelphi, MD, for helpful discussions.

[1]R. Kosugi, T. Umeda, and Y. Sakuma, Appl. Phys. Lett. **99**, 182111 (2011).
[2]J. Rozen, S. Dhar, M. E. Zvanut, J. R. Williams, and L. C. Feldman, J. Appl. Phys. **105**, 124506 (2009).
[3]G. Y. Chung, C. C. Tin, J. R. Williams, K. McDonald, R. K. Chanana, R. A. Weller, S. T. Pantelides, L. C. Feldman, O. W. Holland, M. K. Das, and J. W. Palmour, IEEE Electron Device Lett. **22**, 176 (2001).
[4]G. Y. Chung, C. C. Tin, J. R. Williams, K. McDonald, M. Di Ventra, S. T. Pentelides, L. C. Feldman, and R. A. Weller, Appl. Phys. Lett. **76**, 1713 (2000).
[5]D. B. Habersat, A. J. Lelis, J. M. McGarrity, F. B. McLean, and S. Pothbare, Mater. Sci. Forum **600–603**, 743 (2009).
[6]T. Umeda, K. Esaki, R. Kosugi, K. Fukuda, T. Ohshima, N. Morishita, and J. Isoya, Appl. Phys. Lett. **99**, 142105 (2011).
[7]K. Ueno and T. Oikawa, IEEE Electron Device Lett. **20**, 624 (1999).
[8]C. P. Slichter, *Principles of Magnetic Resonance* (Springer-Verlag, Berlin, 1990).
[9]D. J. Lepine, Phys. Rev. B **6**, 436 (1972).
[10]D. Kaplan, I. Solomon, and N. F. Mott, J. Phys. Lett. (Paris) **39**, 51 (1978).
[11]C. J. Cochrane, P. M. Lenahan, and A. J. Lelis, Appl. Phys. Lett. **102**, 193507 (2013).
[12]J. F. Conley and P. M. Lenahan, IEEE Trans. Nucl. Sci. **40**, 1335 (1993).
[13]T. Aichinger and P. M. Lenahan, Appl. Phys. Lett. **101**, 083504 (2012).
[14]B. C. Bittel, P. M. Lenahan, J. T. Ryan, J. Fronheiser, and A. J. Lelis, Appl. Phys. Lett. **99**, 083504 (2011).

[15]M. A. Anders, P. M. Lenahan, and A. J. Lelis, J. Appl. Phys. **122**, 234503 (2017).
[16]J. S. Brugler and P. G. A. Jespers, IEEE Trans. Electron Devices **ED-16**, 297 (1969).
[17]G. Groeseneken, H. E. Maes, N. Beltran, and R. F. De Keersmaecker, IEEE Trans. Electron Devices **ED-31**, 42 (1984).
[18]P. Heremans, J. Witters, G. Groeseneken, and H. E. Maes, IEEE Trans. Electron Devices **36**, 1318 (1989).
[19]D. R. Hamann, Phys. Rev. B **40**, 2980 (1989).
[20]J. P. Perdew, K. Burke, and M. Ernzerhof, Phys. Rev. Lett. **77**, 3865 (1996).
[21]P. A. Schultz, Phys. Rev. B **60**, 1551 (1999).
[22]P. A. Schultz, Phys. Rev. Lett. **84**, 1942 (2000).
[23]P. A. Schultz, Phys. Rev. Lett. **96**, 246401 (2006).
[24]P. A. Schultz and A. H. Edwards, Nucl. Instrum. Methods B **327**, 2 (2014).
[25]P. A. Schultz and A. von Lilienfeld, Model. Simul. Mater. Sci. Eng. **17**, 084007 (2009).
[26]P. A. Schultz, J. Phys. Condens. Matter **27**, 075801 (2015).
[27]R. M. Van Ginhoven and P. A. Schultz, J. Phys. Condens. Matter **25**, 495504 (2013).
[28]W. Jost, J. Chem. Phys. **1**, 466 (1933).
[29]L. Torpo, M. Marlo, T. E. M. Staab, and R. M. Nieminen, J. Phys. Condens. Matter **13**, 6203 (2001).
[30]A. Zywietz, J. Furthmüller, and F. Bechstedt, Phys. Rev. B **59**, 15166 (1998).
[31]X. Wang, M. Zhao, H. Bu, H. Zhang, X. He, and A. Wang, J. Appl. Phys. **114**, 194305 (2013).
[32]D. P. Ettisserry, N. Goldsman, and A. Lelis, J. Appl. Phys. **115**, 103706 (2014).
[33]P. A. Schultz, R. Van Ginhoven, and A. H. Edwards (unpublished).
[34]R. S. Mulliken, J. Chem. Phys. **23**, 1833 (1955).
[35]J. A. Weil, J. R. Bolton, and J. E. Wertz, *Electron Paramagnetic Resonance, Elementary Theory and Practical Application* (Wiley-Interscience, New York, 1994).
[36]J. R. Morton and K. F. Preston, J. Magn. Reson. **30**, 577 (1978).
[37]F. Stern, Phys. Rev. B **5**, 4891 (1972).

Rapid Communications

Multiple-photon transitions in electrically detected magnetic resonance measurements of 4*H*-SiC transistors

James P. Ashton * and Patrick M. Lenahan

Department of Engineering Science and Mechanics, The Pennsylvania State University, University Park, Pennsylvania 16802, USA

(Received 10 May 2020; revised 29 June 2020; accepted 30 June 2020; published 17 July 2020)

We report an ultralow-field frequency-swept electrically detected magnetic resonance (fsEDMR) measurement scheme sensitive to so-called ultrastrong coupling in paramagnetic systems, which arises from comparatively strong driving fields and weak Zeeman interaction with small static fields. We observe multiple-photon transitions in the EDMR spectrum of a 4*H*-SiC transistor. The multiphoton transitions are a strong function of the linearly polarized driving field and of the static field. The observation of both field-swept EDMR at a constant frequency and fsEDMR demonstrate that the transitions we observe are caused by multiphoton transitions. In the small static field and large driving-field regime, Bloch-Siegert effects cause small changes to the resonant frequency. We observe these Bloch-Siegert shifts in the resonance frequency in the ultralow-field fsEDMR scheme and verify the observation by also measuring the driving field directly using Faraday's law of induction and a sensing coil. Multiphoton transitions are important for quantum engineering applications.

DOI: 10.1103/PhysRevB.102.020101

Multiple-photon transitions have been observed in nuclear magnetic resonance [1–3], electron paramagnetic resonance (EPR) [4,5], and in optically detected magnetic resonance [6]. The multiphoton transitions have widespread applicability from electrically driven magnetic resonance of spins in quantum dots [7], magnetic resonance imaging [8], and manipulation of coherent spin states in spin-based qubits used for quantum computation [9]. Furthermore, in the ultrastrong coupling regime, Bloch-Siegert shifts (BSS) emerge [10], which have applications in imaging [11] and quantum computing [12]. Both multiphoton transitions and BSS are observed in this work in the electrically detected magnetic resonance (EDMR) spectrum of interface defects in 4*H*-SiC/SiO_2 metal-oxide-semiconductor field-effect transistors (MOSFETs). The absorption of two or more photons requires conservation of angular momentum. Right and left circularly polarized photons have corresponding angular momentum $J = 1$ with $m_J = \pm 1$ denoted as $\sigma^{\pm}$ photons, respectively. For multiphoton transitions, discrete numbers of photons are absorbed for the transitions. In the work of Clerjaud and Gelineau, the $n = 2$ transition and $n = 3$ transition were observed in conventional EPR, where n is the number of photons [4]. They account for the angular momentum conservation for the two-photon transition by labeling one of the absorbed quanta as a π photon which would exist if some component of the linearly polarized driving field (B_1) was parallel with the static field B_0. The π-type photons are associated with $m_J = 0$; these photons can be absorbed or emitted by the spin system regardless of the spin angular momentum difference of the transition since the wave function of the π photon is $\pi = \frac{1}{\sqrt{2}}(\sigma^+ + \sigma^-)$ [5]. At ultralow magnetic fields ($\leqslant$0.5 mT) which would involve driving-field frequencies in the range of $\sim$5–15 MHz or less, the electron spin Zeeman interaction is small and comparable to B_1. Mkhitaryan *et al.* show that, in weak field measurements, interaction of the spin system with the environment can cause the two-photon transition [4]. The effect of the environment can be viewed as a time-dependent tilt of the DC field [13]. Mkhitaryan *et al.* modeled the environment for the two-photon absorption as a fluctuator coupled to the spin via the dipole interaction [13]. We utilize the model proposed by Mkhitaryan *et al.* to analyze the shapes of the two-photon resonances [13]. We find strong agreement between the theory of Mkhitaryan *et al.* [13] and our experimental results. Ultralow-field EDMR measurements of spin-dependent recombination currents in SiC devices provide a particularly convenient system to study the ultrastrong coupling regime ($B_1 \approx B_0$). At such low fields and frequencies, the environment enabling the two-photon transition can be conveniently studied; in the case of 4*H*-SiC, the environment would be influenced by (small) hyperfine fields [13]. We observe the electrical detection of the two-photon transition utilizing both continuous-wave EDMR (cwEDMR) and frequency-swept (fs) EDMR. The observation of these transitions in both fsEDMR and cwEDMR demonstrates that they are certainly due to multiphoton transitions; it rules out the possibility of harmonic detection from the apparatus. Ultralow-field fsEDMR is a convenient scheme for studying the EDMR response within the sub-mT range because fsEDMR eliminates a near-zero field magnetoresistance (NZFMR) response, which often dominates the sub-mT regime in a magnetic field-swept measurement [14,15].

Continuous-wave EDMR is achieved in a manner much the same as EPR aside from the detection scheme. In EDMR, a change in device current occurs at resonance. To understand the EDMR results of this paper, we provide a brief discussion of EPR. Consider a sample with paramagnetic defects that is placed within a microwave cavity situated between the pole faces of an electromagnet. Consider first the simplest possible case in which unpaired electrons residing in these defects are

*jamesashton1015@gmail.com

otherwise unperturbed by their local environment. The cavity along with a microwave bridge provides microwave radiation of energy $E = h\upsilon$, where h is Planck's constant and υ is the microwave frequency. The electromagnet provides a magnetic field B; its magnitude splits the unpaired electrons' energy via the Zeeman interaction. The energy of the electron spins in this B field is split into two levels characterized by the electrons' spin quantum number m_s which can either be $+1/2$ or $-1/2$. When the microwave radiation energy is equal to the difference in energy between the electrons' $+1/2$ and $-1/2$ levels [16,17], $h\upsilon = g_e\mu_B B$, resonance occurs and the electrons transition from $+1/2$ to $-1/2$ (or vice versa). Here, g_e is the Landè g factor ($g_e \approx 2.0023\ldots$), μ_B is the Bohr magneton, and B is the magnitude of the applied field. In EPR, the absorption of microwave power is detected. Information about the defect's local environment is extracted via deviations to this resonance condition, two of which are spin-orbit coupling and electron-nuclear hyperfine interactions [16]. Electron-nuclear hyperfine interactions are the interactions between the magnetic moments of the unpaired electrons and the magnetic nuclei. EDMR is based on the intermediate coupling of two electrons which results in a nearly field and frequency independent sensitivity [18]. Thus, ultralow field EDMR measurements are possible without a loss in signal amplitude [18]. For the low magnetic fields utilized, spin-spin interactions are also important to understand our results [19,20].

One way in which EDMR takes place is through spin dependent recombination (SDR). SDR can be understood by theory first developed in a seminal paper by Kaplan, Solomon, and Mott [18]. Consider the following (qualitative) explanation of SDR. When a conduction electron encounters a deep level paramagnetic defect, the unpaired electron will couple with the conduction electron to form an intermediate state. If both electron spins are parallel, the electron will be unable to transition into the paramagnetic defect as this transition would violate the Pauli Exclusion Principle; these triplet states (spin angular momentum $S = 1$) tend to dissociate. However, at resonance, spin flipping events at the deep level site will transform triplet states into singlet states (spin angular momentum $S = 0$), in which the unpaired electron and conduction electron spins are anti-parallel. Now the conduction electron may fall into the deep level and will subsequently recombine with a valance band hole. (This sequence could be reversed with the hole capture followed by electron capture.) The singlet state transition and subsequent recombination conserves spin angular momentum, as $S = 0$, while triplet state capture and recombination will not, as $S = 1$. Other spin dependent transitions detected via EDMR are also possible, such as spin-dependent trap-assisted tunneling [19,21–23].

EPR observations of multiples of the resonance field corresponding to multiphoton transitions have been reported previously [4]. Quite recently, Mkhitaryan *et al.* have addressed, in some detail, the theory of two-photon absorption in magnetic resonance [13]. They model the two-photon resonance line shape as a function of drive (B_1/B_0) and show that for strong drive, the two-photon line shape is a single peak whose spectrum narrows with increasing drive. For weak drive, the two-photon line shape is a two-peaked line with a broader line shape. The ratio (B_1/B_0) has also previously been explored in studies of the transition amplitudes corresponding to multiphoton transitions [5]. For larger transition amplitudes, which are proportional to this ratio, the more likely the multiphoton transitions are to occur. Thus, we expect and observe that ultralow-field (sub-mT) EDMR measurements yield a high sensitivity to multiphoton transitions.

We utilize an n-channel 4*H*-SiC MOSFET with a thermal ONO oxide with thickness 50 nm. These samples have recently been utilized in SDR measurements [24]; they have a very large density of interface defects which yield a large EDMR response. Charge-pumping measurements [25–27] indicate that the average interface defect density is 2×10^{12} cm^{-2} eV^{-1}. The gate area is $250 \times 20\,\mu$m^2. We utilize the bipolar amplification effect (BAE) measurement [28], which is an SDR measurement sensitive to 4*H*-SiC/SiO_2 interface traps with energy levels within the vicinity of the middle of the 4*H*-SiC band gap. In BAE, the MOSFET drain to body contact is forward biased well past the junction built-in voltage and the gate is biased close to but below inversion so that the electrons injected from the drain will travel at or very near to the 4*H*-SiC/SiO_2 interface as they proceed to the source. The body is grounded and the current is monitored through the source, which is held at virtual ground. Our experimental apparatus utilizes a custom-built electromagnet with built in modulation coils situated inside a three-layer cylindrical μ-metal zero-Gauss chamber with outer shield 2.8 m long and 0.6 m in diameter. We utilize a Kepco BOP 20-5D bipolar power supply for magnet power, a Lake Shore Cryotronics 475 DSP Gaussmeter and Hall probe, a Stanford Research Systems SR570 preamplifier, a LABVIEW-based virtual lock-in amplifier, a Marconi/IFR 2026Q rf source fed into a custom-built resonator with diameter 6.6 mm with nine turns, a LeCroy LC564A 1 GHz oscilloscope for power monitoring, and a LABVIEW-based graphical user interface for magnetic-field modulation, data acquisition, magnetic-field control, and power leveling. Magnetic-field modulation is supplied from the computer, amplified by an Insignia stereo amplifier, and subsequently fed into the built-in modulation coils. Figure 1 illustrates a diagram of the experimental setup. For 87.5-MHz measurements, a Doty Scientific 85-MHz, 12-mm-diameter resonator coil was utilized with a 10-W HD Communications Corp. HD29347 1 − 1025-MHz rf amplifier. All measurements were performed at room temperature.

Sweeping frequency can result in changes in the rf level caused by the impedance of the resonator. These changes in rf level could significantly impact the AC device current detected causing power fluctuations in the device that distort the EDMR spectrum. This problem is circumvented by utilizing a proportional-integral-derivative (PID) controller to monitor the power level utilizing a GHz oscilloscope as mentioned previously. The PID scheme for power leveling has recently been introduced by Manning *et al.* for electrically detected electron nuclear double-resonance measurements [29]. The voltage out of the rf source is measured by a GHz oscilloscope and is fed back to the PID controller so that power-level changes are corrected.

Figure 2 illustrates the low-field/frequency (87.5-MHz) cwEDMR and NZFMR [14,15] spectrum for the 4*H*-SiC MOSFET sample. Here, we utilize the Doty Scientific resonator coil. In this measurement, magnetic-field modulation

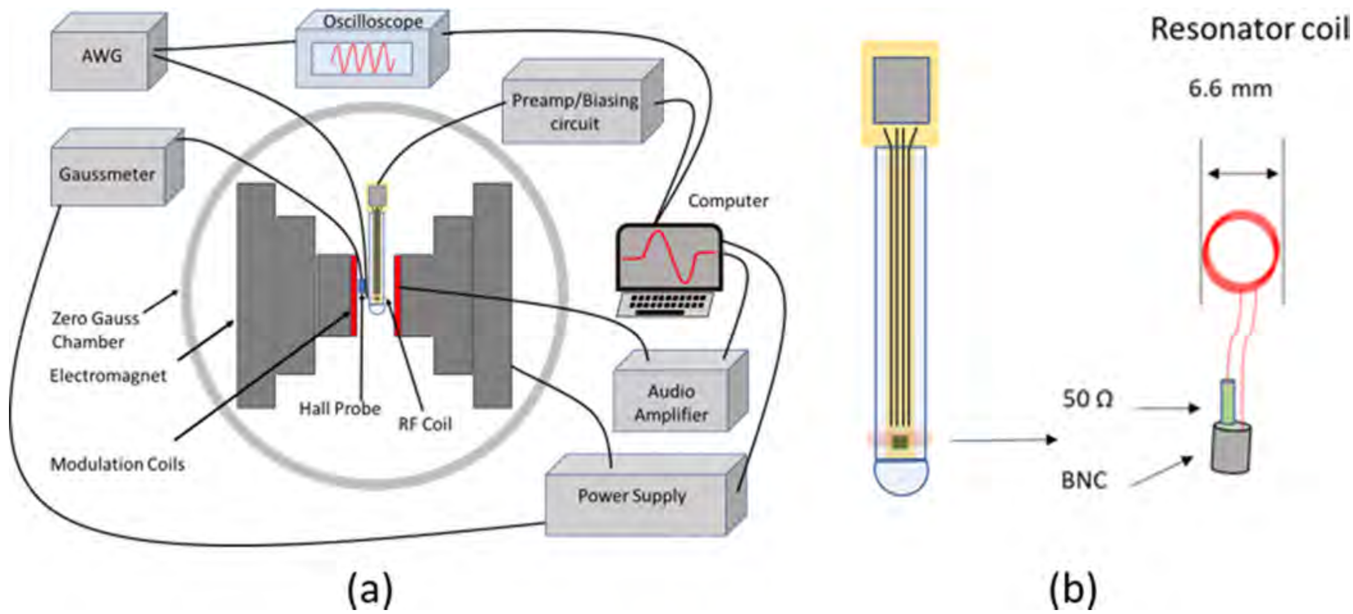

FIG. 1. (a) Schematic illustration of the experimental apparatus; (b) the custom-built resonator.

was utilized. From Fig. 2, the two-photon transition at $B \approx 6$ mT is present. Here, the rf field $B_1 \approx 0.11$ mT, which was measured utilizing a two-turn 12-mm-diameter (matched with the resonator) sensing coil. Thus, the ratio of $B_1/B_0 \approx 10^{-2}$. A half-field "forbidden" $\Delta m_s = 2$ transition is present in Fig. 2, which involves the dipolar interaction of the unpaired electron spin to the conduction-level electron (The half-field transitions can be utilized to count the number of spins, or paramagnetic defects, in the sample [17,19,20].) The spectrum in Fig. 2 has side structures in the EDMR response, which are separated by 1.1 mT. These side peaks are presumably the result of hydrogen complexed *E*' centers in the MOSFET gate oxide [30–33]. It should be noted that the defects studied here presumably have spin-spin relaxation times in the 10s of μs and spin-lattice relaxation times in the range of 100s of μs at room temperature based on recent literature [34–37].

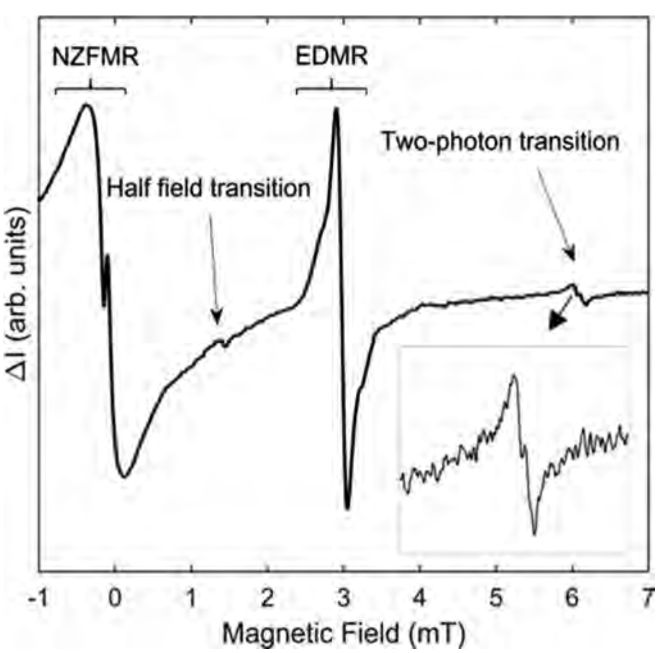

FIG. 2. NZFMR and low-field and -frequency (3 mT/87.5 MHz) cwEDMR spectrum for the 4*H*-SiC transistor. The inset shows the two-photon transition of the cwEDMR spectrum occurring at 6 mT.

As anticipated, the multiphoton transitions of the EDMR spectrum are much more pronounced at ultralow magnetic fields and rf frequencies. We have made measurements in the range of $0.2 - 0.5$ mT corresponding to rf frequencies of $5.6 - 14$ MHz. Since such low resonant fields are utilized, we have housed the low-field spectrometer inside of a zero-Gauss chamber. This eliminates stray magnetic fields caused by the various electronic components utilized and also eliminates the Earth's ambient magnetic field (≈0.05 mT). In the ultralow-field and frequency measurements, we utilize a second custom-built resonator with a 6.6-mm diameter as illustrated in Fig. 1. The values of B_1 were again determined utilizing a diameter-matched 3-turn 6.6-mm sensing coil. Figure 3 shows representative field-swept EDMR spectra with the rf frequency held at 8.4 MHz for $B_1 \approx 0.10$ mT, $B_1 \approx 0.06$ mT, and $B_1 \approx 0.03$ mT. Here, we utilize frequency modulation of the rf to eliminate the NZFMR response. It is clear from Fig. 3 that the $n = 2$ transition can be observed for $B_1 \approx 0.10$ mT and $B_1 \approx 0.06$ mT. Note that signal to noise of the $n = 2$ response for $B_1 \approx 0.06$ mT limits our measure of the center crossing of this line. The line is presumably caused by the two-photon transition evident from the position of the peak (twice the resonant field). The transition disappears at lower power levels. In Fig. 4, we present fsEDMR measurements observed at static magnetic fields of 0.2, 0.3, 0.4, and 0.5 mT. In these measurements, the values of the driving field $B_1 \approx 0.10$ mT, $B_1 \approx 0.06$ mT, $B_1 \approx 0.03$ mT, $B_1 \approx 0.015$ mT. It is clear that with a decrease in B_0 and an increase in B_1, peaks appear at $\upsilon_n = \upsilon_0/n$ where υ_0 is the frequency at which the $n = 1$ transition occurs (the classical

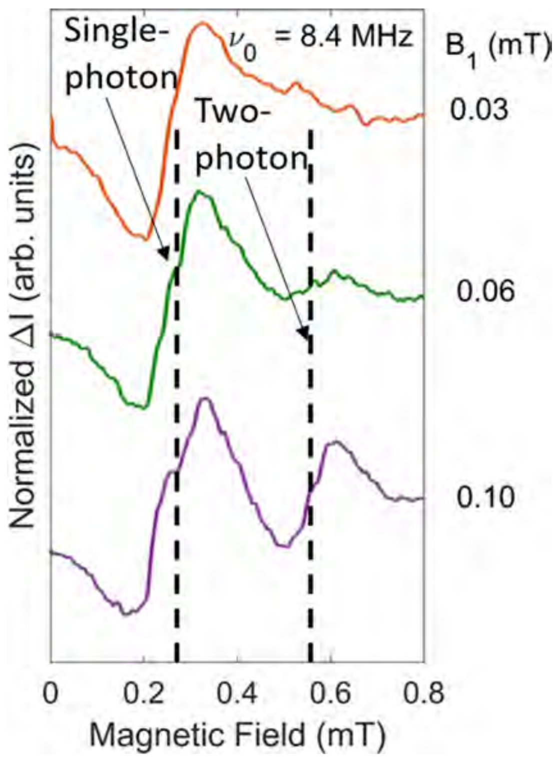

FIG. 3. Representative field-swept ultralow-field EDMR utilizing frequency modulation of the rf. The rf frequency was 8.4 MHz. Note that the two-photon transition is clearly present at twice the resonant field for $B_1 \approx 0.06$ mT and $B_1 \approx 0.10$ mT.

transition). It is quite obvious from this plot that the peaks occur at divisions of the rf frequency corresponding to integer $n > 1$. Table I provides a list of the peak positions and widths of each transition. This confirms that the observed double-field resonances in the cwEDMR measurements are the result of multiphoton transitions as this result could not be caused by harmonics. If these transitions were harmonic detection of the source frequency, one would expect to observe the fsEDMR transitions at integer *multiples* of the resonance frequency. However, it is clear from Fig. 4 that this does not occur and we observe transitions at integer *divisions* of the rf frequency, consistent with multiphoton transitions [7]. The two-photon transition is a forbidden transition. However, as recently proposed by Mkhitaryan *et al.* [13], the observation of the two-photon transition is a consequence of dipole coupling of the paramagnetic center with the environment which can be modeled as "noise." In EDMR measurements of organic light-emitting diodes (OLED), the noise amplitude is controlled by local hyperfine fields [13,38]. In EDMR measurements of 4*H*-SiC MOSFETs, hyperfine fields would also control the level of noise. (It may be worth pointing out that, in 4*H*-SiC, the hyperfine fields could be controlled via isotopic substitution of ^{12}C and ^{28}Si.) Thus, one could effectively *tune* the environment with isotopic substitution; the two-photon transitions could be utilized to study this effect.

Mkhitaryan *et al.* predicted that the shape of the two-photon transition for weak drive ($B_1 \ll B_0$) should have a two-peak structure [13]. One can see this result in the two-photon curve of Fig. 2 at $B \approx 6$ mT corresponding to weak drive since $B_1/B_0 \approx 10^{-2}$. In the fsEDMR spectra of Fig. 4, the two-photon transitions are single peaks whose linewidths narrow with increasing drive. This spectral narrowing of the two-photon line was also predicted by Mkhitaryan *et al.* [13] for strong drive; the single-peak profile of the two-photon transition is sensitive to changes in B_1 since the profile $I(\beta) \propto 1/(1+\beta^2\delta^2)$, where δ is a dimensionless quantity which incorporates the detuning from the two-photon resonance and $\beta \propto B_1^4/B_0^4$ is a dimensionless quantity which incorporates the effect of drive [13]. From Fig. 4 and Table I, the width of the two-photon curve decreases with increasing B_1/B_0 but is only weakly dependent, consistent with the conclusions of Mkhitaryan *et al.* [13].

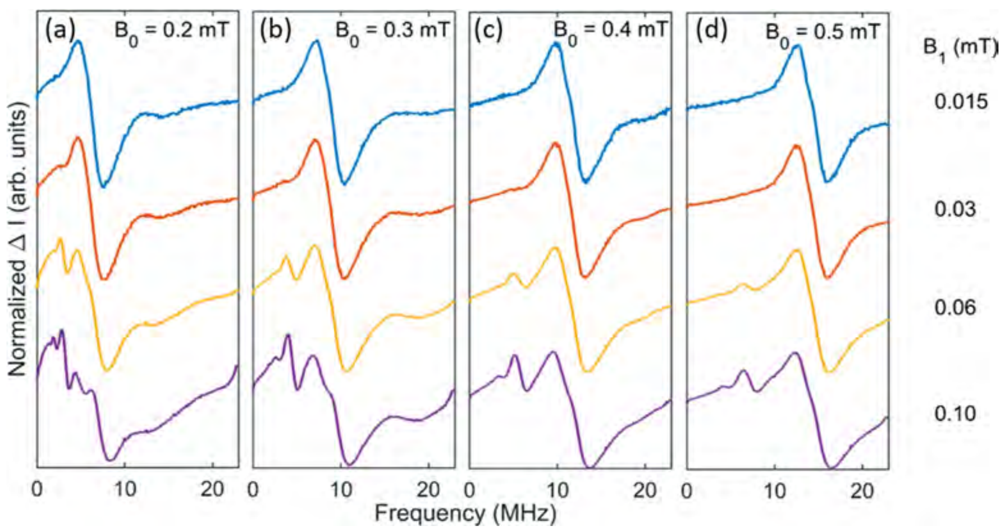

FIG. 4. Frequency-swept ultralow-field EDMR. The amplitudes have been normalized. (a) B_0 set to 0.2 mT, (b) B_0 set to 0.3 mT, (c) B_0 set to 0.4 mT, and (d) B_0 set to 0.5 mT. It is clear that the multiphoton transitions are dependent on both B_0 and B_1. The multiphoton transitions occur at integer divisions of the rf resonant frequency. The $n = 3$ transition is observed for B_1 at 0.10 mT and B_0 at 0.2 mT. The $n = 2$ transition is observed for $B_1 \geqslant 0.06$ mT.

TABLE I. Positions f and width w (in units of MHz) of the single- ($n = 1$), two-($n = 2$), and three- ($n = 3$) photon transition from Fig. 4 for $B_1 \geqslant 0.06$ mT.

B_1 \ B_0	0.2 mT	0.3 mT	0.4 mT	0.5 mT
≈0.10 mT	$n = 1:\ f = 6.3$ $w = 4.0$ $n = 2:\ f = 3.2$ $w = 0.8$ $n = 3: f = 2.1$ $w = 0.4$	$n = 1:\ f = 8.8$ $w = 4.3$ $n = 2:\ f = 4.4$ $w = 1.0$	$n = 1:\ f = 11.4$ $w = 4.2$ $n = 2, f = 5.8$ $w = 1.4$	$n = 1:\ f = 14.1$ $w = 4.3$ $n = 2:\ f = 7.1$ $w = 1.5$
≈0.06 mT	$n = 1: f = 6.1$ $w = 3.4$ $n = 2: f = 3.0$ $w = 0.9$	$n = 1: f = 8.6$ $w = 3.7$ $n = 2: f = 4.3$ $w = 1.2$	$n = 1, f = 11.4$ $w = 3.8$ $n = 2, f = 5.7$ $w = 1.5$	$n = 1, f = 14.1$ $w = 3.6$ $n = 2, f = 7.0$ $w = 1.6$

We expect to observe the BSS [10] of the rf frequency, which occurs for a strong linearly polarized B_1 when B_0 is weak. According to Clerjaud and Gelineau, for odd transitions, the shift in frequency caused by the Bloch-Siegert effect is [4]

$$\Delta\upsilon = \left[\frac{(\gamma B_1)^2}{4\upsilon}\right], \quad p = 0, \quad \text{and}$$

$$\Delta\upsilon = \left[\frac{(\gamma B_1)^2}{4\upsilon}\right](2p+1)/p(p+1), \quad p = 1,\ 2,\ 3, \ldots \quad (1)$$

Here, γ is the gyromagnetic ratio for the electron (28 MHz/mT), $n = 2p + 1$ is the number of photons for the given transition, and υ is the rf frequency. Equation (1) can provide a first-order estimate of the rf field B_1 [4,39]. For the $n = 1$, $p = 0$ transition, we calculate B_1 from the BSS corresponding to the sensing coil measurement of $B_1 \approx 0.10$ mT and $B_1 \approx 0.06$ mT (at lower B_1, the shift is on the order of a few hundredths of a MHz which is below our detection limit). The results are shown in Table II.

The error between the BSS B_1 and the B_1 estimated with the sensing coil is mainly caused by the error in the frequency measurement of the center crossing of the spectra (signal-to-noise limitation) and, to a lesser extent, error of the sensing coil measurement. The B_1 values between the two measurements fall within range of one another. We thus conclude that the BSS extracted B_1 is in agreement with B_1 measured via the sensing coil. We have confirmed the extraction of BSS $B_1 \approx 0.12$ mT via the BSS for the spectrum of Fig. 4 corresponding to $B_0 \approx 0.3$ mT and $B_1 \approx 0.10$ mT measured via the sensing coil [Fig. 5(b), bottom spectrum]. The utilization of BSS for determination of B_1 has been reported elsewhere [8,11,39]. This is an observation of BSS in an EDMR measurement.

In conclusion, we present ultralow-field fsEDMR and magnetic-field-swept cwEDMR results that directly measure multiphoton transitions of the EDMR spectrum of 4H-SiC/SiO_2 interface defects in 4H-SiC MOSFETs. For the ultralow-field range explored here (0.2−0.5 mT), a cwEDMR measurement utilizing conventional magnetic-field modulation would be impossible as a NZFMR response would overwhelm most, if not all, of the ultralow-field EDMR spectrum. We are able to circumvent this problem by utilizing frequency modulation of the rf field. We provide representative cwEDMR spectra as a function of the driving field B_1 and show that transitions corresponding to multiphoton absorption occur at multiples of the rf resonance field. We also utilize fsEDMR at ultralow magnetic fields to confirm the observed multiphoton transitions. In the fsEDMR measurements, we are able to observe transitions up to $n = 3$ photons (Fig. 4). In addition, we observe Bloch-Siegert shifting of the EDMR frequency in our fsEDMR measurements which we confirm via direct measurement of B_1 via Faraday's law with a sensing coil. This represents EDMR observation of the multiphoton transitions in an inorganic semiconductor device. The multiphoton transitions and Bloch-Siegert effect are both important for quantum engineering applications, such as spin-based quantum computation.

We would like to thank Brian R. Manning for his contributions to the spectrometer setup and automatic power leveling. We would also like to thank Stephen J. Moxim for acquiring data and fruitful discussions regarding the interpretation of the results. This work at Penn State was supported by the US Army Research Laboratory. Any opinions, findings, conclusions, or other recommendations expressed herein are those of the authors and do not necessarily reflect the views of the US Army Research Laboratory. This work was also supported by the Air Force Office of Scientific Research under Award No. FA9550-17-1-0242.

TABLE II. Bloch-Siegert shift in MHz, B_1 measured with a sensing coil, and B_1 extracted from (1) for the spectra of Fig. 4(a).

Approximate BSS $\Delta\upsilon$ (MHz)	B_1 estimated with the sensing coil (mT)	B_1 measured through the BSS (mT)
0.5	0.10 ± 0.01	0.12 ± 0.03
0.2	0.06 ± 0.01	0.08 ± 0.04

[1] S. Yatsiv, Phys. Rev. **113**, 1522 (1959).
[2] Y. Zur, M. H. Levitt, and S. Vega, J. Chem. Phys. **78**, 5293 (1983).
[3] P. Bucci, P. Cavaliere, and S. Santucci, J. Chem. Phys. **52**, 4041 (1970).
[4] B. Clerjaud and A. Gelineau, Phys. Rev. Lett. **48**, 40 (1982).
[5] J. Dolinšek, M. Vilfan, and S. Žumer, *Novel NMR and EPR Techniques* (Springer, Berlin, 2006).
[6] V. A. Morozov, A. V. Antzutkin, A. V. Koptyug, and A. B. Doktorov, Mol. Phys. **73**, 517 (1991).
[7] J. Romhányi, G. Burkard, and A. Pályi, Phys. Rev. B **92**, 054422 (2015).
[8] V. Han and C. Liu, Magn. Reson. Med. **84**, 1184 (2020).
[9] S. Bertaina, L. Chen, N. Groll, J. Van Tol, N. S. Dalal, and I. Chiorescu, Phys. Rev. Lett. **102**, 050501 (2009).
[10] F. Bloch and A. Siegert, Phys. Rev. **57**, 522 (1940).
[11] L. I. Sacolick, F. Wiesinger, I. Hancu, and M. W. Vogel, Magn. Reson. Med. **63**, 1315 (2010).
[12] P. Forn-Díaz, J. Lisenfeld, D. Marcos, J. J. García-Ripoll, E. Solano, C. J. P. M. Harmans, and J. E. Mooij, Phys. Rev. Lett. **105**, 237001 (2010).
[13] V. V. Mkhitaryan, C. Boehme, J. M. Lupton, and M. E. Raikh, Phys. Rev. B **100**, 214205 (2019).
[14] C. J. Cochrane and P. M. Lenahan, J. Appl. Phys. **112**, 123714 (2012).
[15] J. P. Ashton, S. J. Moxim, P. M. Lenahan, C. G. McKay, R. J. Waskiewicz, K. J. Myers, M. E. Flatte, N. J. Harmon, and C. D. Young, IEEE Trans. Nucl. Sci. **66**, 428 (2019).
[16] W. Gordy, *Theory and Applications of Electron Spin Resonance* (John Wiley & Sons, New York, 1980).
[17] C. P. Slichter, *Principles of Magnetic Resonance*, 3rd ed. (Springer-Verlag, Berlin, 1978).
[18] D. Kaplan, I. Solomon, and N. F. Mott, J. Phys. Lett. **39**, 51 (1978).
[19] C. J. Cochrane and P. M. Lenahan, Appl. Phys. Lett. **104**, 093503 (2014).
[20] S. S. Eaton, K. M. More, B. M. Sawant, and G. R. Eaton, J. Am. Chem. Soc. **105**, 6560 (1983).
[21] M. A. Anders, P. M. Lenahan, C. J. Cochrane, and J. Van Tol, J. Appl. Phys. **124**, 215105 (2018).
[22] M. J. Mutch, P. M. Lenahan, and S. W. King, Appl. Phys. Lett. **109**, 062403 (2016).
[23] R. J. Waskiewicz, M. J. Mutch, P. M. Lenahan, and S. W. King, in *2016 IEEE International Integrated Reliability Workshop (IIRW)* (IEEE, New York, 2016), pp. 99–102.
[24] J. P. Ashton, P. M. Lenahan, D. J. Lichtenwalner, A. J. Lelis, and M. A. Anders, J. Appl. Phys. **126**, 145702 (2019).
[25] A. B. M. Elliot, Solid State Electron. **19**, 241 (1976).
[26] S. J. Brugler and P. G. Jespers, IEEE Trans. Electron Devices **ED-16**, 297 (1969).
[27] G. Groeseneken, H. E. Maes, N. Beltran, and R. F. D. E. Keersmaecker, IEEE Trans. Electron Devices **ED-31**, 42 (1984).
[28] T. Aichinger and P. M. Lenahan, Appl. Phys. Lett. **101**, 083504 (2012).
[29] B. R. Manning, R. J. Waskiewicz, D. J. McCrory, and P. M. Lenahan, Rev. Sci. Instrum. **90**, 123111 (2019).
[30] C. J. Cochrane, P. M. Lenahan, and A. J. Lelis, J. Appl. Phys. **109**, 014506 (2011).
[31] P. M. Lenahan, C. Cochrane, and A. Lelis, ECS Trans. **64**, 111 (2014).
[32] M. A. Anders, P. M. Lenahan, C. J. Cochrane, and A. J. Lelis, IEEE Trans. Electron Devices **62**, 301 (2015).
[33] M. A. Anders, P. M. Lenahan, and A. J. Lelis, J. Appl. Phys. **122**, 234503 (2017).
[34] S. G. Carter, O. O. Soykal, P. Dev, S. E. Economou, and E. R. Glaser, Phys. Rev. B **92**, 161202(R) (2015).
[35] R. Nagy, M. Niethammer, M. Widmann, Y. C. Chen, P. Udvarhelyi, C. Bonato, J. U. Hassan, R. Karhu, I. G. Ivanov, N. T. Son, J. R. Maze, T. Ohshima, Ö. O. Soykal, Á. Gali, S. Y. Lee, F. Kaiser, and J. Wrachtrup, Nat. Commun. **10**, 1954 (2019).
[36] C. Kasper, D. Klenkert, Z. Shang, D. Simin, A. Gottscholl, A. Sperlich, H. Kraus, C. Schneider, S. Zhou, M. Trupke, W. Kada, T. Ohshima, V. Dyakonov, and G. V. Astakhov, Phys. Rev. Appl. **13**, 044054 (2020).
[37] A. J. Ramsay and A. Rossi, Phys. Rev. B **101**, 165307 (2020).
[38] D. P. Waters, G. Joshi, M. Kavand, M. E. Limes, H. Malissa, P. L. Burn, J. M. Lupton, and C. Boehme, Nat. Phys. **11**, 910 (2015).
[39] I. Hung, P. Gor'kov, and Z. Gan, J. Magn. Reson. **310**, 106636 (2020).

Journal of Applied Physics ARTICLE scitation.org/journal/jap

Ultra-low field frequency-swept electrically detected magnetic resonance

Cite as: J. Appl. Phys. **129**, 083903 (2021); doi: 10.1063/5.0042484
Submitted: 30 December 2020 · Accepted: 9 February 2021 ·
Published Online: 25 February 2021

View Online Export Citation CrossMark

J. P. Ashton,[a] B. R. Manning, W. R. Barker, and P. M. Lenahan[b]

AFFILIATIONS

Engineering Science and Mechanics Department, The Pennsylvania State University, University Park, Pennsylvania 16802, USA

[a]**Author to whom correspondence should be addressed:** jamesashton1015@gmail.com
[b]**URL:** https://sites.esm.psu.edu/wiki/research:pml8:dr._lenahan

ABSTRACT

We have developed a new ultra-low field frequency-swept (FS) electrically detected magnetic resonance (EDMR) spectrometer to perform sensitive EDMR measurements of 4H-silicon carbide (SiC) metal–oxide–semiconductor field-effect transistors at sub-millitesla (mT) magnetic fields. The new spectrometer design enables the detection of so-called ultra-strong coupling effects such as multiple-photon transitions and Bloch–Siegert shifts. In this paper, we present a new spectrometer design and discuss ultra-low field FS-EDMR sensitivity to both multiphoton transitions and Bloch–Siegert shifts of the FS-EDMR response. FS-EDMR effectively eliminates the interference of the sub-mT EDMR response from a near-zero field magnetoresistance (NZFMR) phenomenon that pervades the sub-mT regime in a magnetic field-swept EDMR scheme. We discuss an automatic power leveling scheme, which enables frequency sweeping. We also present results illustrating the Bloch–Siegert shift of the FS-EDMR response. Finally, we study the two-photon transition line shape in the 4H-SiC transistor as a function of the static field, in which we observe a collapse of the two-photon linewidth with decreasing static field and compare our results to the theory of two-photon absorption in EDMR.

I. INTRODUCTION

Recently, there has been increasing interest in performing electrically detected magnetic resonance (EDMR) measurements at ultra-low magnetic fields.[1–10] By utilizing multiple fields and frequencies in EDMR measurements, better separation of hyperfine contributions and spin–orbit coupling can be achieved.[1,7,11] Sub-millitesla (mT) EDMR measurements have recently been demonstrated both in organic[6,8] and inorganic systems.[12] However, studies of magnetic field-swept EDMR in the sub-mT regime have been limited presumably because of a near-zero field magnetoresistance (NZFMR) effect that often overwhelms the sub-mT regime.[13,14]

The purpose of this work is to provide a proof-of-concept demonstration of a new, sensitive sub-mT EDMR technique, which effectively eliminates interference from the NZFMR effect. This work extends recent work by our group in studies of ultra-strong coupling effects in 4H- silicon carbide (SiC) EDMR measurements.[12] The technique utilizes a frequency sweep of the rf that provides the oscillating driving field for resonance with the static field held constant. Utilizing this setup, NZFMR phenomena are no longer detected since the observed transitions depend only on the rf frequency and the applied static magnetic field. The new ultra-low field frequency-swept (FS) EDMR scheme is sensitive to multiple-photon transitions and Bloch–Siegert shifts (BSSs)[15] in measurements of 4H-SiC metal–oxide–semiconductor field-effect transistors (MOSFETs).[12]

4H-SiC is a useful material for high power[16] and high temperature[17] applications because of the wide bandgap (3.26 eV) and features a 10× higher breakdown field (2.2 MV/cm) and higher thermal conductivity (3.7 W/cm K) than silicon (Si).[17] SiC is also becoming progressively more important for quantum engineering applications.[18–23]

The BSS is an important strong coupling phenomenon that has applications in B_1 mapping[24] and quantum engineering.[25] Both multiphoton transitions and BSS have been observed very recently in EDMR measurements performed on organic light emitting diodes.[26] Recently, Kraus *et al.* utilized optically detected magnetic resonance measurements on SiC and achieved detection of multiple-photon resonances through silicon vacancy defects.[23]

Recent work has demonstrated elimination of interference caused by the NZFMR effect in ultra-low field EDMR studies of organics by utilization of amplitude modulation of the rf field.[6,8] In a frequency-swept measurement, the NZFMR response is effectively eliminated because the NZFMR response is independent of the rf and also requires a magnetic field sweep, which is responsible for splitting the electron spin energy levels. The mixing of the electron spin pair levels as the field is swept gives rise to the NZFMR effect.[27] The FS-EDMR scheme enables a single measurement method to probe sub-mT transitions.

In this work, the line shape of the observed two-photon transition in the 4H-SiC MOSFET is also studied utilizing recently developed theory.[28] In this work, the line shape of the two-photon transition is studied as a function of the applied static field.

It should be noted that in NZFMR and EDMR measurements, lock-in amplifier detection is utilized with magnetic field modulation. Thus, the NZFMR and EDMR responses will appear as approximate derivatives.

II. ELECTRON PARAMAGNETIC RESONANCE, ELECTRICALLY DETECTED MAGNETIC RESONANCE, AND SPIN-DEPENDENT TRANSPORT

A. Introduction

Electrically detected magnetic resonance is based on electron paramagnetic resonance (EPR). To understand the results presented, we provide a brief discussion of EPR. Consider a sample containing point defects with unpaired electron spins which is placed in a microwave cavity within an electromagnet. Consider the simplest of cases when the electron is unaffected by its surroundings. When a large magnetic field B_0 is applied, the energy of electrons within these defects will be split into two levels. These levels are determined by the electron's spin quantum number, m_s, which can have a value of +1/2 and −1/2. The sample is also subjected to a microwave field of magnitude B_1. In the simple case of an unpaired electron otherwise unaffected by its surroundings, when the microwave frequency ν times Planck's constant h is equal to the electron energy splitting (Zeeman splitting) $\Delta E = g_e \mu_B B_0$, the sample will absorb microwaves and the unpaired electron spins will "flip." Here, g_e is the Landé g factor ($g_e \approx 2.0023$) and μ_B is the Bohr magneton. At resonance, the electron transitions from its +1/2 to −1/2 spin state (or vice versa). For the simple case of an electron unperturbed by its local environment, the resonance condition is given by[29–31]

$$h\nu = g_e \mu_B B_0. \tag{1}$$

Perturbations to the resonance condition (1) provide structural information about the defects under study. Two of the most important perturbations are spin–orbit coupling and electron–nuclear hyperfine interactions. Spin–orbit coupling changes the Landé g factor g_e to an orientation dependent number often expressed as a second-rank tensor $\mathbf{g}$. Electron–nuclear hyperfine interactions are caused by the interaction between the magnetic moment of the electrons and nearby magnetic nuclei. These two interactions can be described via a spin Hamiltonian of the form,

$$\mathcal{H} = \mu_B \mathbf{B} \cdot \mathbf{g} \cdot \mathbf{S} + \sum_i \mathbf{I}_i \cdot \mathbf{A}_i \cdot \mathbf{S}. \tag{2}$$

Here, $\mathbf{B}$ is the applied magnetic field vector, $\mathbf{g}$ is a second-rank tensor whose parameters depend on the spin–orbit coupling interactions, $\mathbf{S}$ is the electron spin angular momentum operator, $\mathbf{I}_i$ is the nuclear spin angular momentum operator for the ith nucleus, and $\mathbf{A}_i$ is the hyperfine coupling tensor for the ith nucleus. Other perturbations exist and are relevant to this study such as dipolar and exchange interactions.

Conventional EPR has a sensitivity that scales with the field and frequency of the measurement. At X-band frequencies, the sensitivity is about 10^{10} total defects.[32] EPR is also sensitive to every paramagnetic defect within the sample under study. Since conventional EPR measurement sensitivity depends upon the polarization of the spin system, ultra-low field measurements with conventional EPR having extremely low sensitivity. EDMR overcomes these limitations. It has a near field and frequency independent sensitivity and is only sensitive to electrically active defects. It is also 10×10^6 times more sensitive than EPR.[33]

B. Spin-dependent recombination

One transport mechanism detected through EDMR is spin-dependent recombination (SDR). SDR can be understood through seminal work of Kaplan *et al.*[33] and subsequent work refining their ideas.[34–36] The following provides a simplified discussion of SDR. Consider a conduction electron which encounters an unpaired electron spin residing at a deep level defect. The conduction electron and trapped electron will couple to form an intermediate spin state. These spin states can either be singlet states ($S = 0$) with basis state $S_0 = (|\uparrow\downarrow\rangle - |\downarrow\uparrow\rangle)/\sqrt{2}$ with $m_S = 0$ or triplet states ($S = 1$) with basis states $T_+ = |\uparrow\uparrow\rangle$, $T_0 = (|\uparrow\downarrow\rangle + |\downarrow\uparrow\rangle)/\sqrt{2}$, and $T_- = |\downarrow\downarrow\rangle$ with $m_S = +1, 0,$ and -1, respectively. (It should be noted that in the case of higher spin defects, for instance, a spin 3/2 silicon vacancy center, quartet states exist, in which the three electron spins couple.[23,37]) When a magnetic field B_0 is applied, the conduction level electron transition to the deep level will be forbidden by Pauli's exclusion principle since both electrons will have the same spin quantum number. These triplet states will tend to dissociate and there will be no subsequent electron–hole recombination (recombination via triplet states does not conserve spin angular momentum since $S = 1$). However, under resonance, spin flipping events will transform triplet states into singlet states. Now, the conduction electron and the electron residing at the deep level defect have anti-parallel spins. This is now an allowed transition and the conduction electron will fall into the deep level defect and subsequently recombine with a valance band hole (recombination via singlet states does conserve spin angular momentum since $S = 0$). In SDR, the flipping of the trap center spins is generally observed. This process is illustrated in Fig. 1.

C. Two-photon absorption in electrically detected magnetic resonance

In the case where EDMR is achieved with a linearly polarized B_1 field, only odd numbers of photons may be absorbed.[38] Normally,

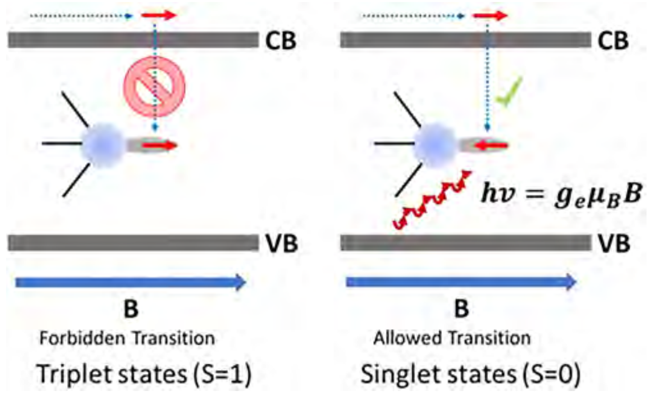

FIG. 1. Illustration of SDR: (left) triplet state dissociation and (right) singlet state recombination.

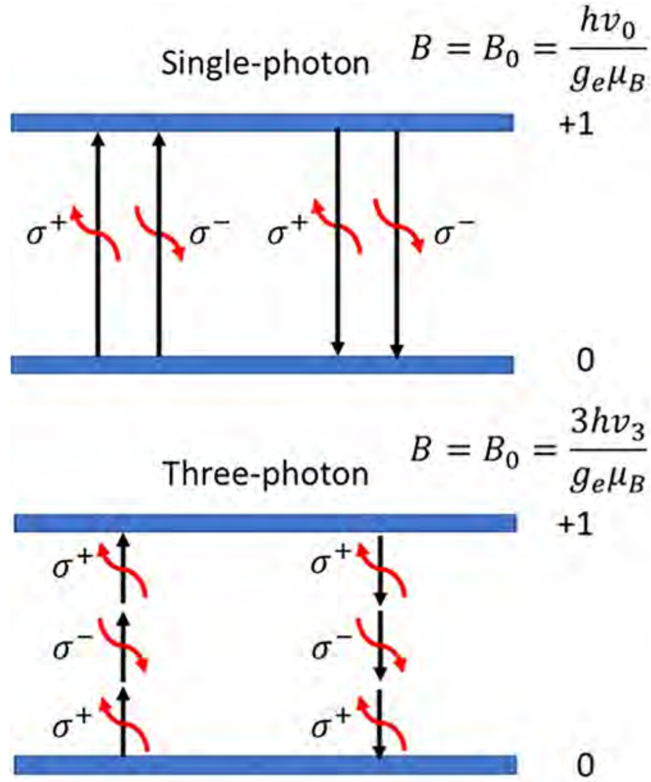

FIG. 2. Cartoon illustration of single-photon transition with $\nu = \nu_0$ (top) and three-photon transition with $\nu = \nu_3 = \nu_0/3$ (bottom) at constant B_0. This multi-photon process is a special case of general multiphoton processes in which a linearly polarized driving field induces resonances through σ^+ and σ^- of the same frequency. Note that both σ^+ and σ^- photons are absorbed in transitions corresponding to $\nu_n = \nu_0/n$. In this case, which is most relevant to this work, only odd transitions are allowed. It should also be noted that other multiphoton processes are possible and outlined elsewhere.[38]

only the $n = 1$ transitions is observed. However, there is a finite probability that $n = 3, 5, 7,$ numbers of photons are absorbed during the transition. This can be detected by scanning out to n times the resonant field. The fact that even-n transitions are generally forbidden can be understood by considering the helicity of the photons involved. If the B_1 field is perpendicular to the static field B_0, photons with angular momentum $J = 1$ will have $m_J = +/-1$. These photons are denoted as $\sigma^{+/-}$, respectively. Consider the simplified diagram of Fig. 2. During the $n = 1$ transition (the classical transition), a single σ^+ or σ^- photon will be absorbed when the microwave or rf frequency of the B_1 field matches the Zeeman splitting of the electron spin states. The $n = 3$ transition can also occur at B_0 if three photons are absorbed, each with frequency $\nu = \nu_3 = \nu_0/3$, where ν_3 is the third sub-harmonic frequency. This can occur because, in a linearly polarized B_1 field, both σ^+ and σ^- photons are present. Thus, as long as the angular momentum difference of the spin transition equals the angular momentum of the combination of photons absorbed, a multiple-photon transition is possible.

Thus, even n transitions are forbidden. However, even transitions have been observed in EPR measurements.[38,39] The even transitions become possible if some component of the B_1 and B_0 field are parallel because π photons become possible. π photons have angular momentum $J = 0$ and their wave function is $\pi = (\sigma^+ + \sigma^-)/\sqrt{2}$.[38] In a recent paper by Mkhitaryan *et al.*,[28] the two-photon transition in EDMR measurements at ultra-low field and frequencies was modeled. The model is based on noise caused by interactions of the environment with the spin system. They note that this can be thought of as a time-dependent tilt of the DC field.[28] The authors predicted the two-photon line shape for a strong drive and weak drive (which depends on the ratio B_1/B_0). In the present paper, we will only consider the strong drive case (weak drive produces a two-peak line shape which resembles electromagnetically induced transparency).[28] The strong drive case produces a single-peak symmetric line whose linewidth narrows with the increase of B_1/B_0. The line shape of the two-photon transition for strong drive [large $\beta \propto (B_1/B_0)^4$] can be modeled using[28]

$$I(\delta) = 2\tau_S\beta \frac{1+\delta^2}{(1+\delta^2)^2 + \beta^2\delta^2} \exp\left(\beta \frac{1-\delta^2}{(1+\delta^2)^2}\right). \qquad (3)$$

Here, δ is a dimensionless parameter describing the detuning from resonance, τ_S is the slow relaxation time, and β is a dimensionless term describing drive. As noted by Mkhitaryan *et al.*, (3) is an approximation for strong drive.[28] Although (3) is an approximation for strong drive, it is sufficiently accurate to describe the experimental results in this paper. We utilize (3) to model the two-photon transition. It should be noted that the "noise," which is utilized to estimate the line shapes is dependent on local hyperfine fields.[28]

D. Near-zero field magnetoresistance

Small local hyperfine fields control spin-dependent transport at near-zero applied fields. A NZFMR effect can appear with sweeping the quasi-static B_0 field through the zero magnetic field. The NZFMR response involves the mixing of singlet and triplet state energy levels and the degeneracy that results in the mixing depends on local hyperfine fields. NZFMR is often broader than the EDMR response and the shoulders of the response can extend well beyond the sub-mT region. A representative NZFMR trace of the 4H-SiC MOSFET is shown in Fig. 3. The NZFMR response can be modeled utilizing solutions to the stochastic quantum Liouville equation and the density matrix.[27]

The NZFMR effect has the potential to be a very useful defect identification tool[27,40] and has been utilized for vector magnetometry for space applications.[18] NZFMR does not depend on the driving field B_1, making it appealing for a simplified and robust magnetometer.[18]

In the case of this work, NZFMR hinders our ability to measure EDMR at sub-mT magnetic fields. The NZFMR response overwhelms the sub-mT EDMR measurements in a magnetic field-swept and magnetic field-modulated scheme because it extends well through the sub-mT regime, as illustrated in Fig. 3. Thus, a key benefit to frequency sweeping the B_1 field is the elimination of the NZFMR effect. This is achieved because the static field is held constant. NZFMR relies on a quasi-static and slowly varying magnetic field.

E. Bloch–Siegert shift

The Bloch–Siegert shift (BSS)[15] in our measurements is caused by the utilization of a linearly polarized driving field B_1. The linear polarization of the drive field induces a shift of the resonance toward higher frequencies.[41] In a magnetic field-swept measurement, the shift would be toward the zero magnetic field.[15,42] While these changes are subtle, the high signal-to-noise EDMR of the 4H-SiC MOSFET interface defects enables a crude extraction of the BSS. As the driving field B_1 approaches B_0, the BSS increases as the square of B_1 via the first order expression:

$$\Delta\nu = \frac{(B_1\gamma)^2}{4\nu_0}. \tag{4}$$

Here, $\Delta\nu$ is the BSS in MHz, γ is the gyromagnetic ratio of the electron (28 MHz/mT), and ν_0 is the resonance frequency in MHz.

III. EXPERIMENTAL

We utilize n-channel 4H-SiC MOSFETs with thermal ONO oxide with a thickness of 50 nm and a gate area of $250 \times 20\,\mu m^2$. These samples have a very large EDMR response corresponding to a large density of interface/near-interface defects.[11,12] We utilize the bipolar amplification effect (BAE) measurement.[43] In BAE, the MOSFET drain-to-body contact is forward biased well past the junction built-in voltage such that only near-interface/interface

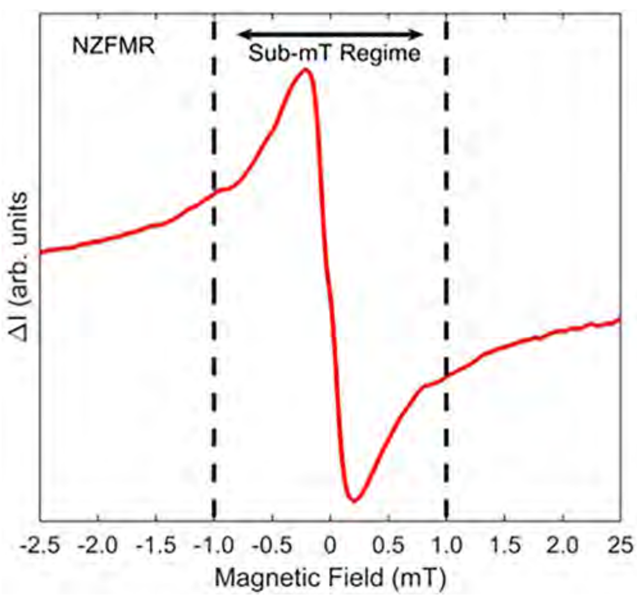

FIG. 3. Representative NZFMR trace illustrating the sub-mT regime.

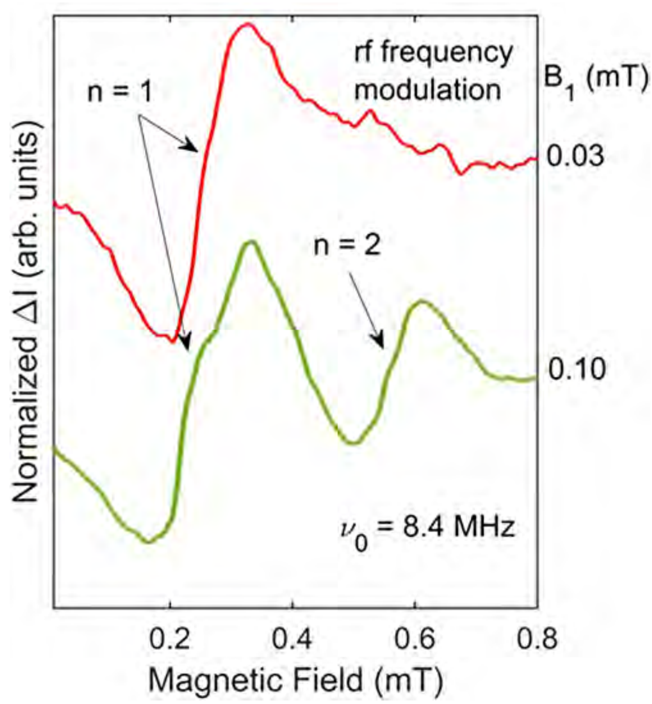

FIG. 4. EDMR response of the 4H-SiC MOSFET utilizing rf frequency modulation. Note that the two-photon transition ($n = 2$) emerges for $B_1 = 0.10$ mT and disappears for $B_1 = 0.03$ mT. Adapted with permission from J. P. Ashton and P. M. Lenahan, Phys. Rev. B **102**, 020101(R) (2020). Copyright 2020 American Physical Society.[12]

defects are detected and the gate is biased close to but below the inversion. The body is grounded and the current is monitored through the source, which is held at virtual ground. This measurement is sensitive to defects with energy levels near the middle of the 4H-SiC bandgap. The values of B_1 were determined utilizing Faraday's law of induction and a sense coil in which the resonator diameter and the sense coil diameter are matched (6.6 mm). All measurements were performed at room temperature.

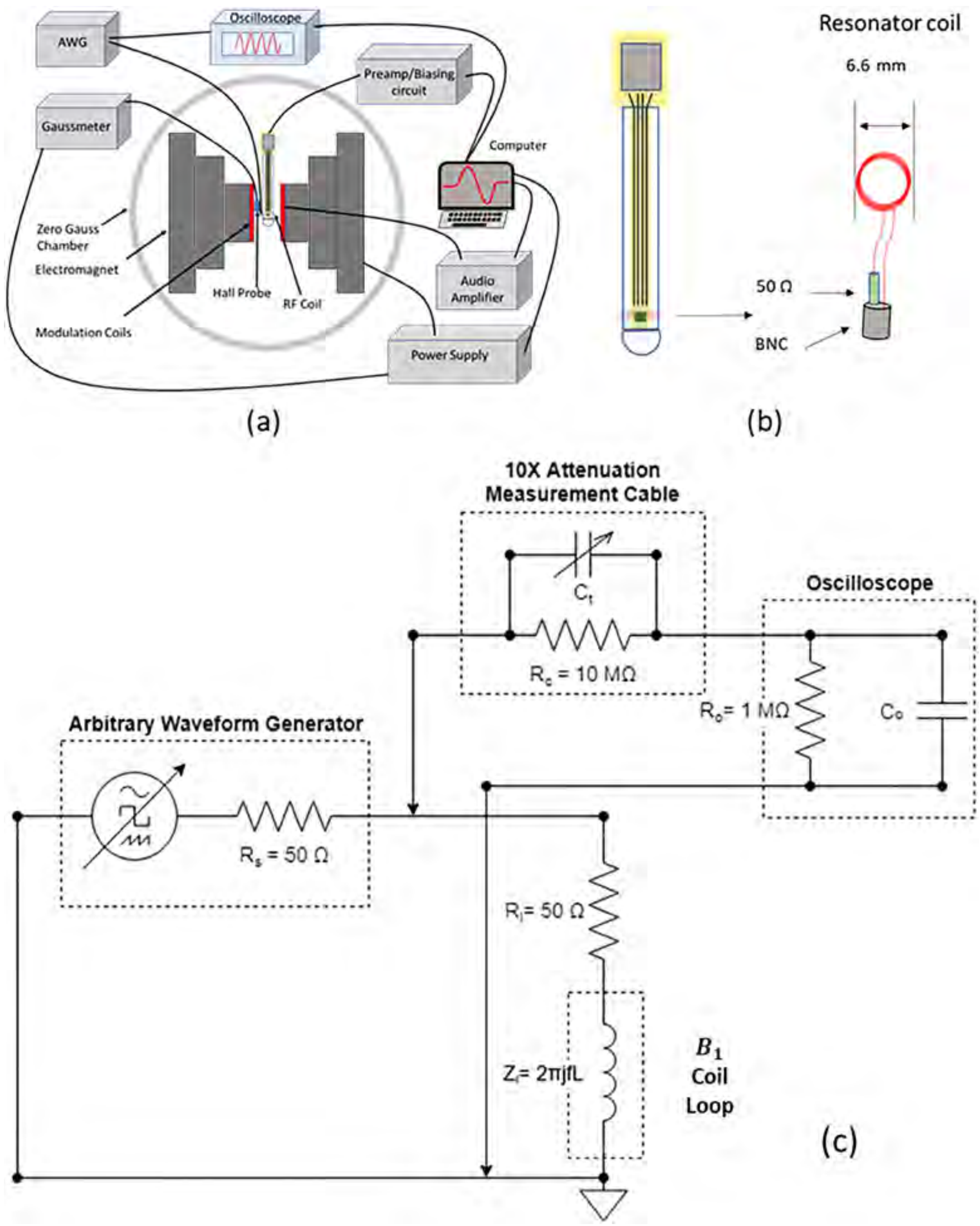

FIG. 5. (a) and (b) Schematic illustration of the ultra-low field FS-EDMR apparatus. Reprinted with permission from J. P. Ashton and P. M. Lenahan, Phys. Rev. B **102**, 020101(R) (2020). Copyright 2020 American Physical Society.[12] (c) FS-EDMR circuit diagram. R_s represents the impedance of the AWG, R_l represents the resistance of the load, Z_l represents the complex impedance of the B_1 coil loop, R_c represents the resistance of the 10× attenuation cable, C_t represents the capacitance of the compensation capacitor, R_o and C_o represent the internal resistance and capacitance of the oscilloscope, respectively. Adapted with the permission from Rev. Sci. Instrum. **90**, 123111 (2019). Copyright 2019 AIP Publishing LLC.[45]

IV. ULTRA-LOW FIELD FREQUENCY-SWEPT ELECTRICALLY DETECTED MAGNETIC RESONANCE

A. Elimination of the NZFMR

In a magnetic field-swept EDMR measurement, the B_1 field is held constant and the B_0 field is swept through resonance. This approach works very well for magnetic fields that are larger than ≈1 mT. However, for sub-mT measurements, a magnetic field-swept scheme utilizing magnetic field modulation would be ineffective since the EDMR response would likely overlap with the NZFMR response. Subtraction of the NZFMR[1,44] can also be utilized but requires an additional time-averaged scan with the rf field turned off. Varying the type of modulation is also an option. Instead of utilizing conventional magnetic field modulation, AM and FM of the rf field can also be utilized.[6,8] In Fig. 4, we utilize FM of the rf field. In this figure, the two-photon line is apparent for $B_1 \approx 0.10$ mT. FS-EDMR also eliminates interference from the NZFMR response because in FS-EDMR, B_0 is held constant. Any observed transitions are caused by the sweeping rf field, which the NZFMR effect is independent of.

B. Spectrometer design

Figure 5(a) illustrates a diagram of the FS-EDMR apparatus. Figure 5(b) illustrates a diagram of the resonator. The ultra-low field FS-EDMR spectrometer utilizes a custom-built 4 in. electromagnet with three sets of coils for greater field uniformity and built-in modulation coils. The electromagnet is situated inside a three-layer cylindrical μ-metal zero-Gauss chamber with outer shield 2.8 m long and 0.6 m in diameter. We utilize a Kepco BOP 20-5D bipolar power supply for magnet power, a Lake Shore Cryotronics 475 DSP Gaussmeter and Hall probe, a Stanford Research Systems SR570 preamplifier, a LabVIEW-based virtual lock-in amplifier, a Marconi/IFR 2026Q rf source fed into a custom-built resonator with diameter 6.6 mm with nine turns, a LeCroy LC564A 1 GHz oscilloscope for power monitoring, and a LabVIEW-based graphical user interface for magnetic field modulation, data acquisition, magnetic field control, and power leveling. Magnetic field modulation is supplied from the computer, amplified by an Insignia stereo amplifier, and subsequently fed into the built-in modulation coils.

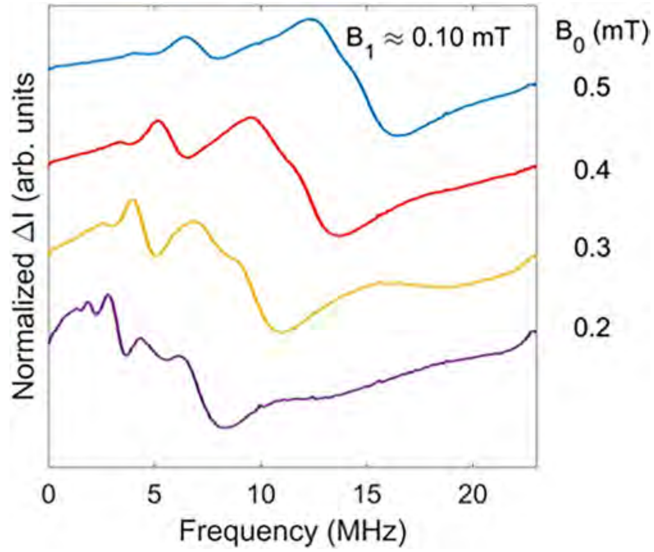

FIG. 7. FS-EDMR response of the 4H-SiC MOSFET for $B_0 = 0.5$, 0.4, 0.3, and 0.2 mT with $B_1 \approx 0.10$ mT. Adapted with permission from J. P. Ashton and P. M. Lenahan, Phys. Rev. B **102**, 020101(R) (2020). Copyright 2020 American Physical Society.[12]

C. Automatic power leveling

Sweeping rf gives rise to power fluctuations in the EDMR response of the device caused by changes in the impedance of the resonator. These power fluctuations can often cause current changes, which are much larger than the EDMR response and obscure the resulting data. In order to circumvent this problem, a software-based proportional-integral-derivative (PID) controller was implemented to provide feedback to reduce fluctuations in power. A similar scheme has recently been implemented by Manning *et al.* for electrically detected electron–nuclear double resonance measurements.[45] A basic block diagram depicting the operation of the PID controller is shown in Fig. 6.

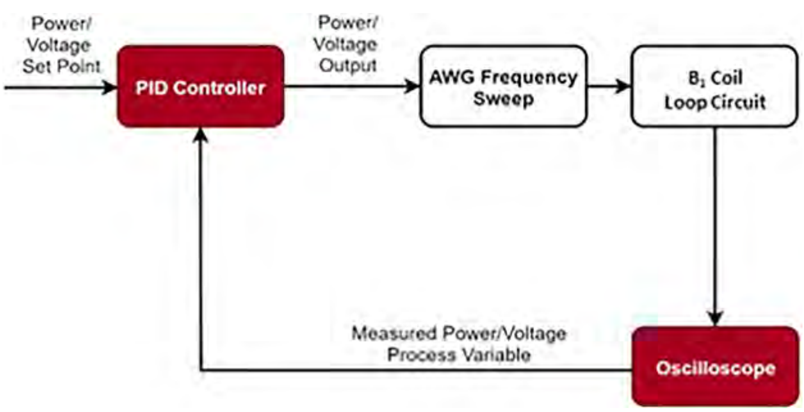

FIG. 6. PID controller implementation for the FS-EDMR spectrometer. Adapted with the permission from Rev. Sci. Instrum. **90**, 123111 (2019). Copyright 2019 AIP Publishing LLC.[45]

The PID controls the response of the arbitrary waveform generator (AWG) by monitoring the difference between the measured output and a set point, which constitutes an error signal.[46] The PID's output adjusts to drive the error toward zero. Additional hardware was also included in order for the PID controller to function. A 50 Ω resistor was added in series with the B_1 coil to behave as the load. This is done to match the internal impedance of the AWG to that of the load. The B_1 coil has an inductance; however, its impedance can be neglected at lower frequencies. However, as the frequency increases, the impedance of the B_1 coil increases. In order to provide the PID controller with the measured output, a LeCroy LC564A 1 GHz oscilloscope is placed in parallel to the 50 Ω resistor and B_1 coil via a high impedance 10× attenuation cable. The circuit diagram of the PID controlled FS-EDMR spectrometer is shown in Fig. 5(c).

The AWG requires a constant 50 Ω load to maintain accurate voltage measurement across the load. Due to the internal 50 Ω source impedance of the AWG, half the voltage will drop over its internal impedance and the other half will drop over the load. The ratio of the load voltage drop to the output of the AWG, $\frac{V_L}{V_{AWG}} = 1/2$, when the source impedance is perfectly matched to that of the load. Any impedance mismatch reflects a portion of the power to the source.[45,47] The PID controller compares the load voltage to the user-defined set voltage. Differences between the measured output and the set point during the frequency sweep causes a growth in the magnitude of the error signal. The impedance of the B_1 coil depends on frequency. The voltage output of the AWG depends on the difference between the desired value and the measured value. As frequency is swept, the power absorbed changes due to the varying impedance of the resonator and other parasitic effects. The PID updates the AWG output to eliminate the effect of any measured changes and drives the error signal down to zero. This causes the AWG output to converge around the set point.[45]

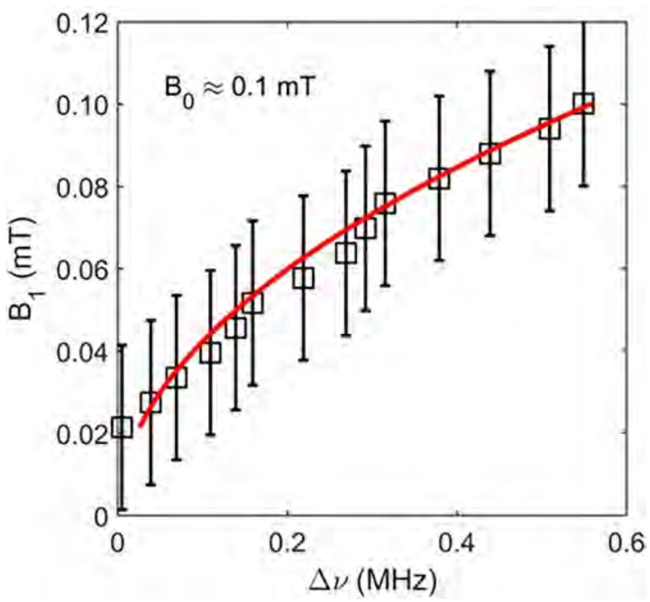

FIG. 8. BSS of the FS-EDMR response for $B_0 \approx 0.1$ mT with B_1 ranging from ≈0.02 to 0.10 mT. B_1 was measured in the data points with a sense coil and Faraday's law of induction. The solid red curve is a plot of the BSS from the first order calculation of (4).

D. FS-EDMR results

We performed FS-EDMR at sub-mT fields of 0.2, 0.3, 0.4, and 0.5 mT. The results are shown in Fig. 7. Here, $B_1 \approx 0.10$ mT was measured utilizing Faraday's law of induction and a sense coil. From Fig. 7, it is clear that the two-photon transition occurs at $\nu_0/2$, where $\nu_0 = g_e\mu_B B_0$ is the frequency corresponding to single-photon resonance (the classical transition).

In a recent paper by our group,[12] the two-photon transition was studied for various values of B_1 and B_0, and it was determined that the observed multiphoton transitions were a strong function of B_1/B_0 as expected by the theory.[28] In this work, the BSS was also observed.[15] In Fig. 8, the BSS is reported from FS-EDMR measurements in which $B_0 = 0.1$ mT and B_1 ranging from ≈0.02 to 0.10 mT. The values of B_1 here were measured utilizing the sensing coil and are plotted with the observed BSS. The red curve is plotted

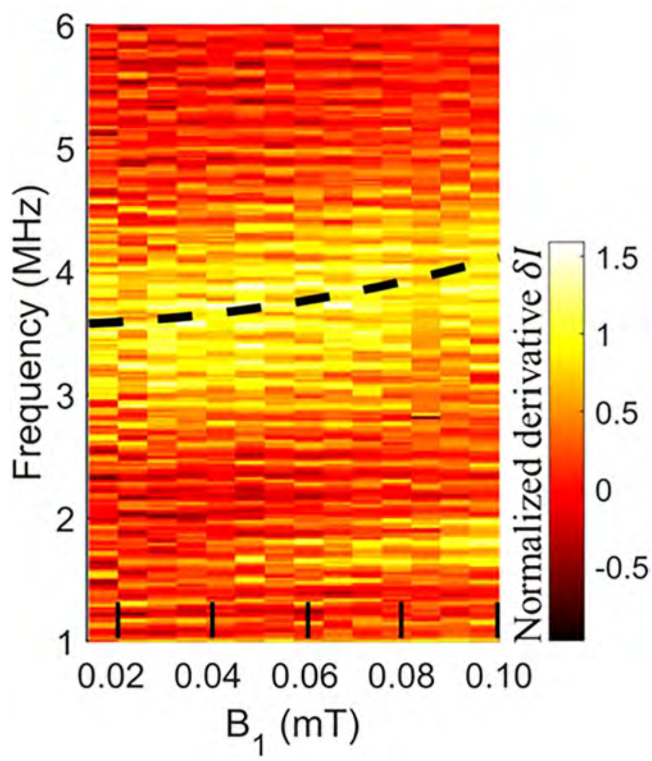

FIG. 9. Color map illustrating the FS-EDMR data with $B_0 \approx 0.1$ mT with B_1 ranging from ≈ 0.015 to 0.10 mT. The color bar indicates the normalized amplitude of the derivative FS-EDMR data. Again, B_1 was measured in the data points with a sense coil and Faraday's law of induction. The dashed curve is a plot of the BSS from the first order calculation of (4).

from (4) utilizing the measured values of B_1. It is clear that the B_1 predicted from the BSS and that measured through the sensing coil scheme are in close agreement. Figure 9 illustrates a color map of FS-EDMR data taken with B_1 ranging from ≈0.015 to 0.10 mT. The dotted line is the first order calculation of (4). The results from Figs. 8 and 9 demonstrate very strong evidence of our observations of the BSS.

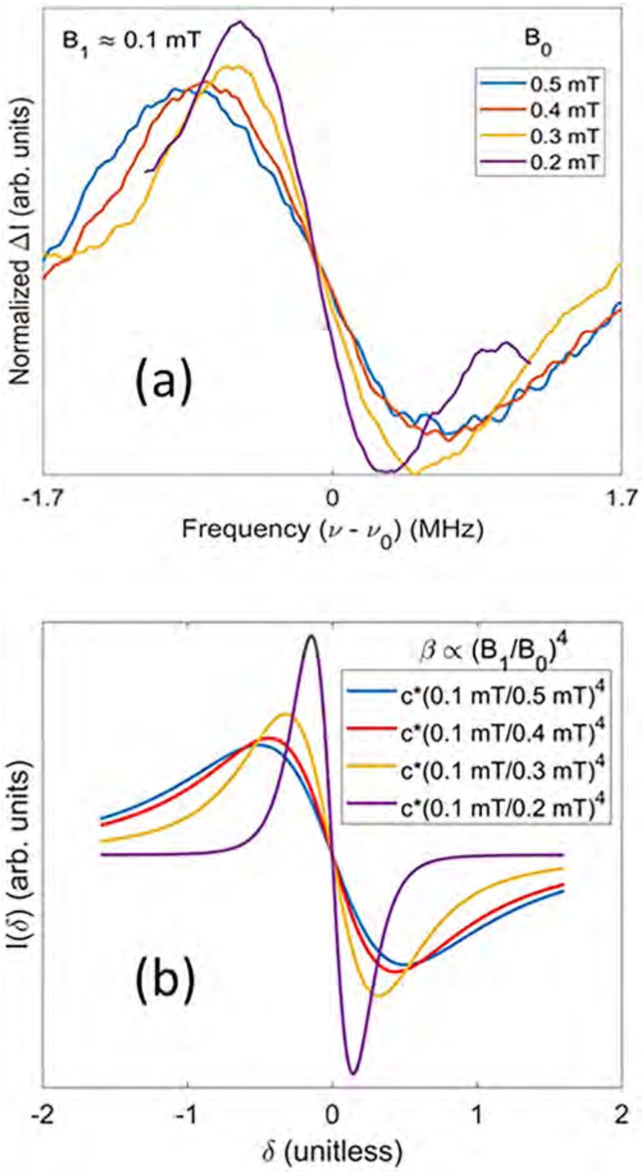

FIG. 10. (a) Two-photon line of the FS-EDMR response of the 4H-SiC MOSFET for $B_0 = 0.5$, 0.4, 0.3, and 0.2 mT with $B_1 \approx 0.10$ mT and (b) theoretical two-photon line shape (3) as a function of $\beta \propto (\frac{B_1}{B_0})^4$. Here, τ_S in (3) is set to 100 μs.

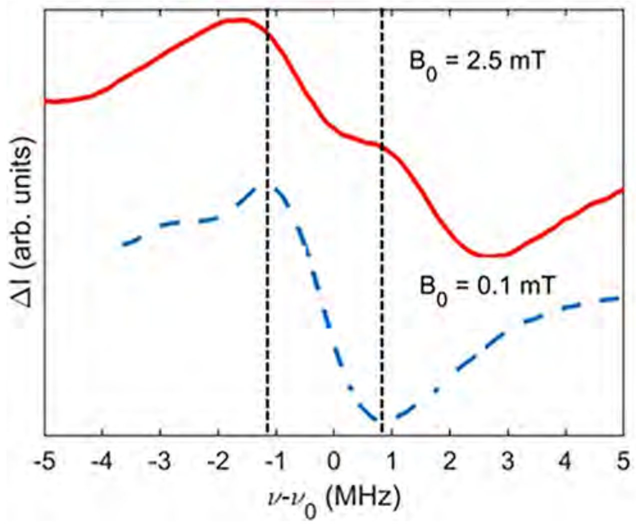

FIG. 11. FS-EDMR response of the 4H-SiC MOSFET for $B_0 = 0.1$ mT (bottom dashed blue data) and $B_0 = 2.5$ mT (top solid red data) with $B_1 \approx 0.015$ mT. The dashed vertical lines indicate the peak-to-peak linewidth of the $B_0 = 0.1$ mT data (≈2 MHz). The $B_0 = 2.5$ mT data are much broader (≈4.5 MHz).

In Fig. 10, the two-photon line is plotted as a function of $\beta \propto (\frac{B_1}{B_0})^4$ from (3). Utilizing (3), we calculate the two-photon resonance line and compare the line shape to the experimental two-photon line shape. Note that with increasing drive (which is $\propto B_1/B_0$), there is a narrowing of the two-photon resonance in both the experimental FS-EDMR data and data predicted from (3). Here, τ_S was set to 100 μs as the defects involved in this work have spin lattice relaxation lifetimes of order 100 μs.[20–22,48]

Finally, we report on limited results illustrating a broadening with the field and frequency of the FS-EDMR measurement. The results are shown in Fig. 11. The broadening observed is likely caused by effects of hyperfine-induced relaxation, which alters the spin-lattice relaxation time T_1 and the spin-spin relaxation times T_2. This effect has been described theoretically by Fedin *et al.*[49] In their analysis, a Redfield[50] relaxation framework was utilized. They show that, in the frequency domain, one would observe a narrowing of the EPR response at magnetic fields B_0 approaching the hyperfine coupling A. These results suggest such an effect is occurring. However, more data must be collected to confirm.

V. CONCLUSIONS

This work demonstrates a new apparatus for sensitive frequency-swept electrically detected magnetic resonance measurements in sub-mT magnetic fields. At sub-mT magnetic fields, ultra-strong coupling effects such as Bloch–Siegert shifts and multiple-photon transitions become detectable. The work illustrates several advantages offered by the new apparatus. FS-EDMR effectively eliminates the NZFMR effect, which overwhelms the sub-mT regime in magnetic field-swept EDMR measurements at low fields.

We compare the new FS-EDMR scheme to the magnetic field-swept EDMR in which FM modulation is implemented. In a frequency-swept measurement, the static field is held constant and multiphoton transitions occur at sub-harmonics. In a magnetic field-swept measurement, the B_1 frequency is held constant and multiphoton transitions occur at integer multiples of the resonance field.

We also compare our two-photon line shape to theory[28] and observe a narrowing of the two-photon line with the decreasing static field, consistent with the theory of two-photon absorption in EDMR measurements.[28] We illustrate the Bloch–Siegert shift with the static field B_0 held at ≈0.1 mT. The observation of both multiphoton transitions and the Bloch–Siegert shift in EDMR measurements of a 4H-SiC device at room temperature have utility in spintronics and quantum engineering applications as long coherence times of spin pairs may be inferred. Finally, limited results showing a field- and frequency-dependent broadening presumably involving hyperfine are reported. FS-EDMR measurements at sub-mT fields may also be applied to studies of other ultra-strong coupling effects in EDMR measurements such as the spin-Dicke effect.[10]

ACKNOWLEDGMENTS

This work at Penn State was supported by the U.S. Army Research Laboratory under Award No. W911NF-16-2-0061. Any opinions, findings, conclusions, or other recommendations expressed herein are those of the authors and do not necessarily reflect the views of the U.S. Army Research Laboratory. This work was also supported by the Air Force Office of Scientific Research under Award No. FA9550-17-1-0242.

DATA AVAILABILITY

The data that support the findings of this study are available from the corresponding author upon reasonable request.

REFERENCES

[1] M. A. Anders, P. M. Lenahan, and A. J. Lelis, "Multi-resonance frequency spin dependent charge pumping and spin dependent recombination—Applied to the 4H-SiC/SiO_2 interface," J. Appl. Phys. **122**, 234503 (2017).
[2] M. A. Anders, P. M. Lenahan, C. J. Cochrane, and J. Van Tol, "Physical nature of electrically detected magnetic resonance through spin dependent trap assisted tunneling in insulators," J. Appl. Phys. **124**, 215105 (2018).
[3] M. A. Anders, P. M. Lenahan, A. H. Edwards, P. A. Schultz, and R. M. Van Ginhoven, "Effects of nitrogen on the interface density of states distribution in 4H-SiC metal oxide semiconductor field effect transistors: Super-hyperfine interactions and near interface silicon vacancy energy levels," J. Appl. Phys. **124**, 184501 (2018).
[4] H. Morishita, L. S. Vlasenko, H. Tanaka, K. Semba, K. Sawano, Y. Shiraki, M. Eto, and K. M. Itoh, "Electrical detection and magnetic-field control of spin states in phosphorus-doped silicon," Phys. Rev. B **80**, 205206 (2009).
[5] M. Brandt, M. Bayerl, M. Stutzmann, and C. Graeff, "Electrically detected magnetic resonance of a-Si:H at low magnetic fields: The influence of hydrogen on the dangling bond resonance," J. Non-Cryst. Solids **227–230**, 343–347 (1998).
[6] T. Grünbaum, S. Milster, H. Kraus, W. Ratzke, S. Kurrmann, V. Zeller, S. Bange, C. Boehme, and J. M. Lupton, "OLEDs as models for bird magnetoception: Detecting electron spin resonance in geomagnetic fields," Faraday Discuss. **221**, 92–109 (2020).
[7] G. Joshi, R. Miller, L. Ogden, M. Kavand, S. Jamali, K. Ambal, S. Venkatesh, D. Schurig, H. Malissa, J. M. Lupton, and C. Boehme, "Separating hyperfine from spin-orbit interactions in organic semiconductors by multi-octave magnetic resonance using coplanar waveguide microresonators," Appl. Phys. Lett. **109**, 103303 (2016).
[8] S. Milster, T. Grünbaum, S. Bange, S. Kurrmann, H. Kraus, D. M. Stoltzfus, A. E. Leung, T. A. Darwish, P. L. Burn, C. Boehme, and J. M. Lupton, "Perdeuterated conjugated polymers for ultralow-frequency magnetic resonance of OLEDs," Angew. Chem. **59**, 9388–9392 (2020).
[9] D. M. Stoltzfus, G. Joshi, H. Popli, S. Jamali, M. Kavand, S. Milster, T. Grünbaum, S. Bange, A. Nahlawi, M. Y. Teferi, S. I. Atwood, A. E. Leung, T. A. Darwish, H. Malissa, P. L. Burn, J. M. Lupton, and C. Boehme, "Perdeuteration of poly [2-methoxy-5-(2-ethylhexyloxy)-1, 4-phenylenevinylene] (d-MEH-PPV): Control of microscopic charge-carrier spin-spin coupling and of magnetic-field effects in optoelectronic devices," J. Mater. Chem. C **8**, 2764–2771 (2020).
[10] D. P. Waters, G. Joshi, M. Kavand, M. E. Limes, H. Malissa, P. L. Burn, J. M. Lupton, and C. Boehme, "The spin-Dicke effect in OLED magnetoresistance," Nat. Phys. **11**, 910–914 (2015).
[11] J. P. Ashton, P. M. Lenahan, D. J. Lichtenwalner, A. J. Lelis, and M. A. Anders, "Electrically detected magnetic resonance study of barium and nitric oxide treatments of 4H-SiC metal-oxide-semiconductor field-effect transistors," J. Appl. Phys. **126**, 145702 (2019).
[12] J. P. Ashton and P. M. Lenahan, "Multiple-photon transitions in electrically detected magnetic resonance measurements of 4H-SiC transistors," Phys. Rev. B **102**, 020101(R) (2020).
[13] C. J. Cochrane and P. M. Lenahan, "Zero-field detection of spin dependent recombination with direct observation of electron nuclear hyperfine interactions in the absence of an oscillating electromagnetic field," J. Appl. Phys. **112**, 123714 (2012).
[14] J. P. Ashton, S. J. Moxim, P. M. Lenahan, C. G. McKay, R. J. Waskiewicz, K. J. Myers, M. E. Flatte, N. J. Harmon, and C. D. Young, "A new analytical tool for the study of radiation effects in 3-D integrated circuits: Near-zero field magnetoresistance spectroscopy," IEEE Trans. Nucl. Sci. **66**, 428–436 (2019).
[15] F. Bloch and A. Siegert, "Magnetic resonance for nonrotating fields," Phys. Rev. **57**, 522–527 (1940).
[16] J. Biela, M. Schweizer, S. Waffler, and J. W. Kolar, "SiC versus Si—Evaluation of potentials for performance improvement of inverter and DCDC converter systems by SiC power semiconductors," IEEE Trans. Ind. Electron. **58**, 2872–2882 (2011).
[17] J. B. Casady and R. W. Johnson, "Status of silicon carbide (SiC) as a wide-bandgap semiconductor for high-temperature applications: A review," Solid State Electron. **39**, 1409–1422 (1996).
[18] C. J. Cochrane, J. Blacksberg, M. A. Anders, and P. M. Lenahan, "Vectorized magnetometer for space applications using electrical readout of atomic scale defects in silicon carbide," Sci. Rep. **6**, 37077 (2016).
[19] H. Kraus, D. Simin, C. Kasper, Y. Suda, S. Kawabata, W. Kada, T. Honda, Y. Hijikata, T. Ohshima, V. Dyakonov, and G. V. Astakhov, "Three-dimensional proton beam writing of optically active coherent vacancy spins in silicon carbide," Nano Lett. **17**, 2865–2870 (2017).
[20] R. Nagy, M. Niethammer, M. Widmann, Y. C. Chen, P. Udvarhelyi, C. Bonato, J. U. Hassan, R. Karhu, I. G. Ivanov, N. T. Son, J. R. Maze, T. Ohshima, Ö. O. Soykal, Á. Gali, S. Y. Lee, F. Kaiser, and J. Wrachtrup, "High-fidelity spin and optical control of single silicon-vacancy centres in silicon carbide," Nat. Commun. **10**, 1954 (2019).
[21] S. G. Carter, O. O. Soykal, P. Dev, S. E. Economou, and E. R. Glaser, "Spin coherence and echo modulation of the silicon vacancy in 4H-SiC at room temperature," Phys. Rev. B **92**, 161202(R) (2015).
[22] C. Kasper, D. Klenkert, Z. Shang, D. Simin, A. Gottscholl, A. Sperlich, H. Kraus, C. Schneider, S. Zhou, M. Trupke, W. Kada, T. Ohshima, V. Dyakonov, and G. V. Astakhov, "Influence of irradiation on defect spin coherence in silicon carbide," Phys. Rev. Appl. **13**, 044054 (2020).
[23] H. Kraus, V. A. Soltamov, D. Riedel, S. Väth, F. Fuchs, A. Sperlich, P. G. Baranov, V. Dyakonov, and G. V. Astakhov, "Room-temperature quantum

microwave emitters based on spin defects in silicon carbide," Nat. Phys. **10**, 157–162 (2014).
[24]L. I. Sacolick, F. Wiesinger, I. Hancu, and M. W. Vogel, "B_1 mapping by Bloch-Siegert shift," Magn. Reson. Med. **63**, 1315–1322 (2010).
[25]P. Forn-Díaz, J. Lisenfeld, D. Marcos, J. J. García-Ripoll, E. Solano, C. J. Harmans, and J. E. Mooij, "Observation of the Bloch-Siegert shift in a qubit-oscillator system in the ultrastrong coupling regime," Phys. Rev. Lett. **105**, 237001 (2010).
[26]S. Jamali, V. V. Mkhitaryan, H. Malissa, A. Nahlawi, H. Popli, T. Grünbaum, S. Bange, S. Milster, D. Stoltzfus, A. E. Leung, T. A. Darwish, P. L. Burn, J. M. Lupton, and C. Boehme, "Floquet spin states in OLEDs," Nat. Commun. **12**, 465 (2021).
[27]N. J. Harmon, S. R. McMillan, J. P. Ashton, P. M. Lenahan, and M. E. Flatte, "Modeling of near zero-field magnetoresistance and electrically detected magnetic resonance in irradiated Si/SiO_2 MOSFETs," IEEE Trans. Nucl. Sci. **67**, 1669–1673 (2020).
[28]V. V. Mkhitaryan, C. Boehme, J. M. Lupton, and M. E. Raikh, "Two-photon absorption in a two-level system enabled by noise," Phys. Rev. B **100**, 214205 (2019).
[29]J. A. Weil, J. R. Bolton, and J. E. Wertz, *Electron Paramagnetic Resonance—Elementary Theory and Practical Applications*, 2nd ed. (John Wiley & Sons, Hoboken, NJ, 2007).
[30]W. Gordy, *Theory and Applications of Electron Spin Resonance* (John Wiley & Sons, New York, 1980).
[31]C. Slichter, *Principles of Magnetic Resonance*, 3rd ed. (Springer-Verlag, Berlin, 1978).
[32]G. R. Eaton, S. S. Eaton, D. P. Barr, and R. T. Weber, *Quantitative EPR* (Springer, New York, 2010).
[33]D. Kaplan, I. Solomon, and N. Mott, "Explanation of the large spin-dependent recombination effect in semiconductors," J. Phys. Lett. **39**, 51–54 (1978).
[34]F. C. Rong, W. R. Buchwald, E. H. Poindexter, W. L. Warren, and D. J. Keeble, "Spin-dependent Shockley-Read recombination of electrons and holes in indirect-band-gap semiconductor p-n junction diodes," Solid State Electron. **34**, 835–841 (1991).
[35]C. Boehme and K. Lips, "Theory of time-domain measurement of spin-dependent recombination with pulsed electrically detected magnetic resonance," Phys. Rev. B **68**, 245105 (2003).
[36]R. Haberkorn and W. Dietz, "Theory of spin-dependent recombination in semiconductors," Solid State Commun. **35**, 505–508 (1980).
[37]M. Widmann, S. Y. Lee, T. Rendler, N. T. Son, H. Fedder, S. Paik, L. P. Yang, N. Zhao, S. Yang, I. Booker, A. Denisenko, M. Jamali, S. Ali Momenzadeh, I. Gerhardt, T. Ohshima, A. Gali, E. Janzén, and J. Wrachtrup, "Coherent control of single spins in silicon carbide at room temperature," Nat. Mater. **14**, 164–168 (2015).
[38]J. Dolinšek, M. Vilfan, and S. Žumer, *Novel NMR and EPR Techniques* (Springer, Berlin, 2006), pp. 143–183.
[39]B. Clerjaud and A. Gelineau, "Observation of electron paramagnetic resonance at multiples of the "classical" resonance magnetic field," Phys. Rev. Lett. **48**, 40–43 (1982).
[40]N. J. Harmon, J. P. Ashton, P. M. Lenahan, and M. E. Flatté, "Near-zero-field spin-dependent recombination current and electrically detected magnetic resonance from the Si/SiO_2 interface," arXiv:2008.08121 [cond-mat.mtrl-sci] (2020).
[41]J. Romhányi, G. Burkard, and A. Pályi, "Subharmonic transitions and Bloch-Siegert shift in electrically driven spin resonance," Phys. Rev. B **92**, 054422 (2015).
[42]V. A. Morozov, O. N. Antzutkin, A. Koptyug, and A. B. Doktorov, "Multiquantum resonances in low-field optically detected ESR of radical-ion pairs," Mol. Phys. **73**, 517–540 (1991).
[43]T. Aichinger and P. M. Lenahan, "Giant amplification of spin dependent recombination at heterojunctions through a gate controlled bipolar effect," Appl. Phys. Lett. **101**, 083504 (2012).
[44]C. J. Cochrane and P. M. Lenahan, "Spin counting in electrically detected magnetic resonance via low-field defect state mixing," Appl. Phys. Lett. **104**, 093503 (2014).
[45]B. R. Manning, R. J. Waskiewicz, D. J. McCrory, and P. M. Lenahan, "Apparatus for electrically detected electron nuclear double resonance in solid state electronic devices," Rev. Sci. Instrum. **90**, 123111 (2019).
[46]M. Rata, G. Rata, and V. Chatziathanasiou, "A solution for the study and understanding of PID controllers," in *2014 International Conference and Exposition on Electrical and Power Engineering (EPE)* (IEEE, 2014), pp. 182–185.
[47]B. Mindan and L. Hong, "The analysis of impedance matching problem in RF circuit design," in *2010 International Forum on Information Technology and Applications* (IEEE, 2010), Vol. 1, pp. 350–353.
[48]A. J. Ramsay and A. Rossi, "Relaxation dynamics of spin-3/2 silicon vacancies in 4H-SiC," Phys. Rev. B **101**, 165307 (2020).
[49]M. Fedin, P. Purtov, and E. Bagryanskaya, "Anisotropic hyperfine interaction-induced spin relaxation in a low magnetic field," Chem. Phys. Lett. **339**, 395–404 (2001).
[50]A. G. Redfield, "On the theory of relaxation processes," IBM J. Res. Dev. **1**, 19–31 (1957).